Dissipative phase transitions in open quantum lattice systems

Florent Storme

Université Paris Diderot-Paris 7
Sorbonne Paris Cité

Ecole doctorale: Physique Ile-de-France

Laboratoire Matériaux et Phénomènes Quantiques

DOCTORAT

Physique

Florent Storme

Dissipative phase transitions in open quantum lattice systems

Transitions de phases dissipatives dans les systèmes quantiques ouverts sur réseaux

Thèse dirigée par Cristiano Ciuti

Soutenue le 24 Novembre 2017

JURY

Dr.	Juan José GARCIA-RIPOLL	CSIC Madrid	Rapporteur
Dr.	Sebastian SCHMIDT	ETH Zürich	Rapporteur
Prof.	Angela VASANELLI	Université Paris Diderot	Présidente
Prof.	Michiel WOUTERS	Universiteit Antwerpen	Examinateur
Prof.	Cristiano CIUTI	Université Paris Diderot	Directeur

Remerciement

Une thèse est un ouvrage collectif. C'est donc avec une réelle reconnaissance que je remercie l'ensemble des personnes qui m'ont soutenues dans ce travail.

La première d'entre elles est bien sûr Cristiano Ciuti, qui a dirigé ma thèse. C'est son imagination et ses talents scientifiques qui ont rendu possible les différents résultats présentés ici. De plus, il a toujours su suscité l'intérêt pour de nouveaux projets et ainsi me transmettre le goût du défi. Je me dois aussi de le remercier pour la patience dont il a fait preuve pendant la préparation de ce manuscrit.

Je remercie aussi tout particulièrement les membres de mon jury Angela Vasanelli, Michiel Wouters et les deux rapporteurs de ma thèse Juan-José Garcia Ripoll et Sebastian Schmidt. C'est avec un grand plaisir que j'ai répondu à vos questions qui m'ont permis d'approfondir ma compréhension et qui ont provoqué ma curiosité.

Il me faut aussi faire une mention spéciale à Alexandre Le Boité. Il m'a beaucoup aidé, que ce soit dans l'étude de la mécanique quantique des systèmes ouverts avant son départ en Allemagne, mais surtout à son retour pour l'amélioration de mon manuscrit. Son aide et ses corrections ont été cruciales pour la réussite tant de la rédaction que de la présentation.

Je tiens aussi à remercier les scientifiques avec qui j'ai eu la chance de collaborer tels que José Lebreuilly, Said Rodriguez, Jacqueline Bloch, Davide Rossini, Jacopo Carusotto, Rosario Fazio et Simon Pigeon. Ces collaborations internationales m'ont permis de progresser tant scientifiquement qu'humainement.

Le caractère exceptionnel de l'équipe théorie repose sur l'ensemble des chercheurs permanents ou non. Je remercie tout particulièrement Riccardo, Alberto et Wim avec qui j'ai pris beaucoup de plaisir à travailler et qui ont été essentiels à la réalisation des travaux présentés dans ce manuscrit. Je remercie aussi les anciens du groupe qui ont été une grande source d'inspiration pour moi. Parmi eux, j'ai une pensée pour Matthieu qui a fait le déplacement pour ma soutenance et avec qui il est toujours enrichissant de travailler. Je tiens aussi à remercier Stefano qui a participé aux bases de ce travail avant le début de ma thèse, ainsi que Juan pour sa bonne humeur et ses encouragements.

Je pense aussi aux doctorants avec qui j'ai eu le plus d' « overlap ». D'abord, Jared : on a commencé et terminé ensemble, je me souviendrai de nos batailles de Nerf à 23h pendant la rédaction. Ensuite, je remercie Fabrizio avec qui j'ai passé d'excellentes vacances en Grèce. Je remercie aussi Filippo Vicentini, autant pour nos échanges scientifiques que pour les fêtes qu'il a organisé. Au delà des doctorants, je remercie Nicola

pour ses efforts pour parler en français dans un groupe très italien et Guiliano Orso pour les discussions stimulantes et sa bonne humeur. Je souhaite bonne chance aux nouveaux de l'équipe, Cassia et Filippo Stellin à qui je souhaite de réussir dans leur parcours de recherche.

Au-delà de l'équipe théorie, je remercie les autres doctorants pour les bons moments partagés avec eux. Je me souviendrai en particulier du week-end thésard dans le Verdon, des diffusions de matchs de foot dans la cafétéria pour la coupe du monde et la coupe d'Europe. Je me souviendrai bien sûr du séminaire thésard. Cela a été l'occasion pour moi de collaborer avec Maria et de tester mes capacités d'organisation. C'est maintenant à Zahra de continuer l'organisation de cette « institution » du laboratoire et je lui souhaite bonne chance !

Dans un cadre plus formel, les journées MPQ ont aussi été des événements importants dans mes années au laboratoire. Ces activités ont ponctué mes années de thèses et ont apporté de bons moments avec les autres doctorants du laboratoire : Roméo, Romain, Hélène, Adrian, Adrien, Tom, Cynthia, Nabeel ainsi que tous les doctorants du thésarium. J'ai aussi eu la chance de fréquenter les doctorants d'autres laboratoires, en particulier Marijana et Titta du C2N avec qui je passe toujours de bons moments.

Dans le laboratoire, il est important de souligner le soutien de la direction et de l'équipe administrative. Je remercie Carlo Sirtori qui a été le directeur du Laboratoire pendant la durée de ma thèse pour m'avoir accueilli, tout comme Anne Servouze, Jocelyne Moreau et Sandrine Di Concetto qui sont certainement les meilleures administratrices de l'Université.

Le sport fait partie de mon équilibre et à contribuer à la réussite de mon parcours c'est pourquoi je tiens en particulier à remercier les membres du club d'athlétisme du Paris Avenir Athletic: Philippe, Jérôme, Arnaud, Jordan, Kahina, Noémie, Laetitia, Kelly, Julien, Karim, Gunther, Anaïs, Nicolas, Tim, Sami et tous les autres... Merci aussi à Moh et Justin qui ont pu se déplacer le jour J, pour leur amitié.

Je veux aussi remercier mes autres amis de Paris, Gabrielle et Tot pour les apéros dans leur jardin.

J'ai aussi une pensée pour Camille, Alexandre, Delphine, Jimmy, Tavi et les autres personnes que j'ai eu la chance de connaître pendant mes études tant à Lyon qu'à Télécom Bretagne à Brest.

Je remercie mes amis d'école et de lycée : Florence, Maxime et Jean-David.

Enfin, je remercie ma famille. Tout d'abord ma sœur Blandine qui a fait le chemin de Lyon pour ma thèse, ainsi que ma mère et mon beau-père. Je n'oublie pas, ma grand-mère Dany et mon grand-père Paul : leur soutien et leurs encouragements m'ont beaucoup aidés durant toutes ces années.

J'ai aussi une pensée particulière pour mon père, mon grand-père Roger et ma grand-mère Nicole.

Je voudrai terminer ces remerciements avec une citation qui peut servir de réponse à la question "comment se passe ta thèse ?":

"Vous savez, moi je ne crois pas qu'il y ait de bonne ou de mauvaise situation. Moi, si je devais résumer ma vie aujourd'hui avec vous, je dirais que c'est d'abord des rencontres. Des gens qui m'ont tendu la main, peut-être à un moment où je ne pouvais pas, où j'étais seul chez moi. Et c'est assez curieux de se dire que les hasards, les rencontres forgent une destinée... Parce que quand on a le goût de la chose, quand on a le goût de la chose bien faite, le beau geste, parfois on ne trouve pas l'interlocuteur en face je dirais, le miroir qui vous aide à avancer. Alors ça n'est pas mon cas, comme je disais là, puisque moi au contraire, j'ai pu : et je dis merci à la vie, je lui dis merci, je chante la vie, je danse la vie... je ne suis qu'amour ! Et finalement, quand beaucoup de gens aujourd'hui me disent « Mais comment fais-tu pour avoir cette humanité ? », et bien je leur réponds très simplement, je leur dis que c'est ce goût de l'amour ce goût donc qui m'a poussé aujourd'hui à entreprendre une construction mécanique, mais demain qui sait ? Peut-être simplement à me mettre au service de la communauté, à faire le don, le don de soi..."

Autis, *Atsérix et Obélix: Mission Cléopatre*, Alain Chabat, 2002

Abstract

This thesis is about the theory of open quantum many-body physics with a particular focus on driven-dissipative photonic and spin lattices. After a review of the main physical platforms and theoretical concepts, we describe our original results.

In Chapter 2, we present a theory of the single-mode Kerr model with a time-dependent pump. This model describes a single-mode optical cavity with a third-order optical nonlinearity. In the regime of parameters where the semiclassical analysis shows bistability, we find that a dynamic hysteresis loop appears in the exact solution. The hysteresis area as a function of the sweep time shows a double power-law decay where the second exponent is independent of the system parameters. We show how these effects are related to the emergence of a dissipative phase transition. We also describe concisely the experimental results which have recently confirmed such theoretical predictions.

In Chapter 3, we present the corner-space renormalization method. In order to obtain the steady-state density matrix of the lattice, we solve the Lindblad master equation in a subspace of the Hilbert space (the "corner"). The states spanning the corner space are selected iteratively using eigenvectors of the density matrix of smaller lattice systems, merging in real space two lattices at each iteration and selecting M pairs of states by maximizing their joint probability. The accuracy of the results is then improved by increasing the dimension M of the corner space until convergence is reached. The method has been benchmarked on a two-dimensional Bose-Hubbard model with coherent driving. The strength and limitations of the method are critically discussed.

In Chapter 4, we investigate a dissipative phase transition in the two-dimensional anisotropic Heisenberg XYZ model. Using the corner-space renormalization method we present a finite-size analysis of steady-state observables. In particular, we show the critical behaviour of the magnetic susceptibility, the entropy growth and the entanglement witnesses, providing a first evaluation of the critical exponents characterizing the transition. A study of the dynamics of finite-size systems is also consistent with a critical slowing down. For comparison, we present the corresponding analysis for one-dimensional arrays, showing the absence of criticality due to the reduced dimension.

In Chapter 5, we explore the non-equilibrium photonic phases of a dissipative Bose-Hubbard model with incoherent pumping of coupled two-level systems. Within a Gutzwiller mean-field approach, we determine the steady-state phase diagram of the system. We predict a second-order phase transition between an incompressible Mott-like phase and a coherent delocalized phase.

Résumé

Les travaux théoriques présentés dans cette thèse portent sur la physique à N-corps dans les systèmes quantiques ouverts. Nous nous intéressons en particulier aux réseaux dissipatifs de spins ou de cavités optiques non-linéaires avec pompage extérieur.

Après une revue des principales plateformes physiques et concepts théoriques au Chapitre 1, nous présentons dans le Chapitre 2 une théorie quantique du modèle de Kerr à un mode avec une pompe modulée dans le temps. Ce modèle décrit une cavité optique présentant une non-linéarité d'ordre trois. Dans le régime où la théorie semi-classique prédit un comportement bistable, nous trouvons qu'une boucle d'hystérésis apparaît dans la solution quantique exacte. L'aire de la boucle d'hystérésis en fonction de la période de la modulation décroît en suivant une double loi de puissance. Nous montrons que ces effets sont liés à l'émergence d'une transition de phase dissipative. Nous décrivons brièvement des résultats expérimentaux qui confirment nos prédictions.

Dans le Chapitre 3, nous introduisons la méthode "corner-space renormalization". Pour obtenir la matrice densité du réseau, nous résolvons l'équation maîtresse dans un sous-espace de l'espace de Hilbert. Les états qui engendrent ce sous-espace sont sélectionnés de façon itérative à partir des états propres des matrices densité de plus petits réseaux. Lors de la fusion de deux réseaux, nous sélectionnons les paires d'états en maximisant leur probabilité combinée. L'exactitude de la méthode est testée sur un réseau de Bose-Hubbard bidimensionnel pompé de façon cohérente.

Dans le Chapitre 4, nous examinons une transition de phase dissipative dans un réseau de spin bidimensionnel implémentant le modèle XYZ anisotrope de Heisenberg. En s'appuyant sur la méthode introduite dans le Chapitre 3, nous menons une analyse de taille finie des observables dans l'état stationnaire. En particulier, nous montrons le comportement critique de la susceptibilité magnétique, de la croissance de l'entropie et de marqueurs d'intrication, fournissant ainsi la première estimation des exposants critiques caractérisant cette transition. Notre étude de la dynamique de ces systèmes est également en accord avec l'hypothèse d'un ralentissement critique. Comme point de comparaison, nous exposons des résultats analogues pour des réseaux unidimensionnels, montrant ainsi l'absence de criticité en une dimension.

Dans le Chapitre 5, nous examinons les phases photoniques hors-équilibre d'un réseau de Bose-Hubbard dissipatif couplé à un ensemble de systèmes à deux niveaux. Dans le cadre d'une approximation de champ moyen à la Gutzwiller, nous déterminons le diagramme des phases stationnaires du système. Nous prédisons une transition de phase

du second ordre entre une phase incompressible semblable à un isolant de Mott et une phase cohérente délocalisée.

Contents

General Introduction

The first numerical approach to a complex mathematical problem can be traced back to 1777 when Buffon proposed a way to estimate π using probabilities. In his proposal, he considered a floor with equidistant lines and needles. The needles are dropped randomly and independently and when a large number of needles is used, it is possible to evaluate the probability for a needle to cross a line. Furthermore, that probability is linked to the number π which can therefore be evaluated from that procedure [1].

Even though a computer is not necessary to solve that early example, it can easily be implemented and contains the main idea of what would be a major step in numerical physics: mapping a complicated or technical calculation into an ensemble of easier operations using random numbers. Such types of algorithms go under the generic name of Monte-Carlo methods. The first modern example of such methods was implemented in the framework of the Manhattan Project in Los Alamos. Using the ENIAC, the first fully electronic computer at the University of Pennsylvania, Stanislaw Ulam and John von Neumann were able to simulate the behaviour of neutron diffusion across materials. The algorithm was based on a statistical sampling on both the initial position and speed of the particles as well as on the possible interactions with the material [2].

The next fundamental step for the establishment of numerical methods in physics was accomplished by Enrico Fermi, John Pasta, Stanislaw Ulam and Mary Tsingou [3, 4]. This very first "numerical experiment" aimed at investigating an ensemble of 62 oscillators with small non-linear couplings. The goal of this simulation was to test the ergodicity hypothesis for non-integrable systems: the results revealed that the hypothesis failed in this case as the system became quasi-periodic. Hence, this experiment was a breakthrough showing that numerical simulations were a powerful tool to explore new physical phenomena.

Since then, the use of computers to solve new physical problems has become a widespread method in physics. If we focus now on quantum mechanics, the scarcity of analytical solutions calls for the development of numerous numerical apporaches. Apart from the different Monte-Carlo techniques that were developed over the years to address a growing number of problems, a significant improvement was given by the renormalization group introduced by Wilson [5]. Wilson's approach was developed to solve the Kondo problem. In that case, solving means giving a good approximation of the many-body eigenstates with the lowest energies. To do so, Wilson first considered all the energy states that are coupled with the impurity. This continuum of states is dis-

cretized and mapped into a one-dimensional chain: the first site of the chain represents the impurity and it is coupled to the second site representing the most relevant state, which is coupled to a site representing the second most important one and so on and so forth. Formally, that means that the Hamiltonian of the system is obtained as the limit of a sequence of Hamiltonians $\hat{H}_N$ considering the N first states. By construction, the $(N+1)$-th term is obtained from the N-th term. When the sites are added to the chain, the number of degrees of freedom increases exponentially making a brute-force computation impossible. In order to evaluate the eigenstates, the exponential growth of the Hilbert space has to be bypassed. To do so, when one constructs the Hamiltonian for the $(N+1)$-th step, the elements from $\hat{H}_N$ are limited to the lowest lying eigenstates. As a result, the number of states considered is kept fixed under a given limit. This crude method proved most successful for the Kondo model and other impurity systems [6]. The key point here is that the coupling to the impurity is decreasing quickly when the chain is extended. Hence, the new sites induce only a perturbation to the many-body state, producing marginal truncation errors.

In fact, if one tries to apply real-space renormalization methods similar to Wilson's to many-body Hamiltonians on a lattice, it can lead to a dramatic failure due to problems related to boundary conditions [7]. This discovery lead to the development of the density matrix renormalization group (DMRG) [8]. This method is based on the selection of the most probable states of the reduced density matrix of a block, obtained by computing the ground state of the Hamiltonian of a larger block. Furthermore, it was shown in Refs. [9, 10] that the states constructed by the density matrix renormalization group were of a particular form: Matrix Product States [11] (MPS) allowing for variational computations. This formulation allowed to apply the DMRG formalism to a much wider range of problems. In particular, it was used to compute the excitation spectrum of one dimensional spin chains [12], as well as time integration [13, 14, 15, 16] and simulation of infinite systems [17]. This improvement made the DMRG-based methods very important for the study of quantum many-body systems at equilibrium. However, these algorithms remain mostly limited to one-dimensional arrays. Indeed, the generalization of this type of methods to two-dimensional lattices is quite challenging and requires the use of the projected entangled pairs formalism [18, 19], the transposition of the second spatial dimension into a one-dimensional system with long-range interactions [20, 21] or a generalized version of matrix product states [22].

The theory of many-body physics at equilibrium has been quite successful in the exploration of condensed matter physics (atomic systems and solid-state materials). Among the numerous achievements, one of particular importance is the description of quantum phase transitions [23, 24, 25]. A paradigmatic system undergoing a quantum phase transition is given by the Bose-Hubbard model [26] describing bosons living on a lattice with on-site interactions and nearest-neighbours hopping. The characteristic feature of a phase transition is the singular behaviour of ground state observables at the so-called critical point. In the case of the Bose-Hubbard model at equilibrium two

distinct phases exist: for strong interactions, there is a strongly localized phase with negligible number fluctuations (Mott Insulator); for large enough hopping, a delocalized superfluid phase emerges.

The investigation of quantum phases of matter has also been extended to cases where the system is driven far from equilibrium [27]. An example of such behaviour is the dynamics after a quench in closed quantum systems. As the system is instantaneously driven to a state far from the ground state of the modified Hamiltonian, the subsequent dynamics might be highly nontrivial. The investigation of the time-dependence of quantum correlations [28] or other correlation functions [29] has been the goal of a considerably large literature.

Lately, new physical platforms have emerged, being relevant for the study of out of equilibrium quantum many-body systems. In particular, over the past two decades, quantum fluids of light have been investigated both theoretically and experimentally in photonic platforms [30]. The many-body physics of light has become accessible thanks to sizeable and controllable photon-photon interactions mediated by electronic excitations in suitable semiconducting or superconducting systems. This has been particularly successful in systems in the so-called strong light-matter coupling regime. In this regime, matter excitations and photons give rise to hybrid quasiparticles called polaritons [31]. The intrinsically dissipative nature of photons causes the polaritons to have a finite lifetime. Hence, these systems cannot be described as closed systems, but have to be treated as open systems. A driving pump is needed to inject new excitations in the system resulting into a rich time evolution, which can lead to a steady-state. This time-evolution can be described via a master equation that accounts for the Hamiltonian dynamics as well as the dissipation and decoherence processes.

The strong coupling between matter degrees of freedom and photonic ones provides strong enough interactions to make possible the emergence of collective behaviours. As an early example of such collective phenomena, we can cite the realization of polariton condensates [32] and superfluidity [33] in planar semiconductor microcavities. In such microstructures, the light is confined using Bragg mirrors. The matter excitations are excitons: electron-hole pairs bounded by Coulomb forces. They are confined in quantum wells that are placed in between the two mirrors. These systems exhibit yet only a moderate nonlinearity. Theoretically, lattice models with giant photon-photon interactions have been pioneered in Refs. [34, 35, 36] even though these first theoretical studies neglected completely photon losses. The realization of strong interaction can lead to the so-called photon blockade [37]: the presence of one photon in the cavity can block the absorption of a second photon. Photon blockade has been demonstrated in atomic [38] and superconducting [39] systems. Superconducting lattices appear to be a particularly promising platform for strong photon-photon interactions.

In order to take into account the competition between dissipation, driving, hopping and interactions, novel theoretical methods have been introduced. Early on, the MPS framework has been extended to density matrices leading to methods based on Matrix

Product Operators (MPO) [14, 15, 40]. These methods are based on the time evolution of the density matrix using an MPO representation. Using such methods, it was possible to characterize novel steady-state phases such as geometrically fustrated polaritons [41] or fermionized photons [42]. This approach of solving the master equation has recently been complemented by variational approaches [43, 44]. In these methods, the determination of the steady-state of the system is mapped into a minimization problem. Note that methods based on projected entangled pairs have also been developed for two dimensional dissipative arrays [45].

A simpler theoretical approach is given by Gutzwiller mean-field theory, where the density matrix is approximated as the product of single-site density matrices. In this approximation, the lattice problem is reduced to the self-consistent description of a single site. This method leads to substentially easier calculations making it a viable tool for a first exploration of the phase diagram. However, there is no control over this approximation: hence it is necessary to confirm the results with those obtained with other methods. This framework allowed to a first exploration of photonic and dissipative spins lattices [46, 47, 48, 49, 50]. In order to include short range correlations that can have a dramatic impact on the steady-state phases, an improvement is offered by a cluster mean-field ansatz. Namely, instead of reducing the description to a single site, a small cluster of sites is considered with self-consistent boundary conditions [51, 52]. In the same spirit, several expansions of the density matrix taking into account the correlations in a perturbative manner have been introduced [53, 54]. Recently, also a linked-cluster expansion has been explored [55].

Other approximations such as the so-called truncated-Wigner Montecarlo method [30, 56, 57] have been considered. In the limit of moderate interactions, the truncated Wigner approximation has been rather successful [33, 57]. Indeed, mapping the complex driven-dissipative quantum dynamics into a set of scalar stochastic differential equations leads to a dramatic speed up of the integration time. This method was extensively used in the early days of the investigation of quantum fluid of light [30], and is now used to study driven-dissipative Bose-Hubbard lattices with relatively weak interactions [58, 59]. In order to include the on-site quantum aspects, a particular decoupling was recently proposed. In this spirit, a Gutzwiller decoupling [60] has been considered in the framework of the Montecarlo wavefunction method [61, 62, 63] leading to the evaluation of a steady-state density matrix neglecting spatial quantum correlations.

It is also worth noting that methods from field theory such as the Keldysh functional formalism have been applied to driven-dissipative systems (for a review see Ref. [64]). In particular, it is a powerful tool to investigate the thermodynamic limit of driven open quantum systems as it enables the use of renormalization methods [65]. Within this formalism, it is possible to estimate critical exponents that characterize phase transitions [66], as well as effective temperatures for the steady-state in the thermodynamic limit [67]. However, so far quantum correlations cannot be properly evaluated using these methods nor their finite-size dependence.

This thesis presents original theoretical contributions to the physics of driven-dissipative strongly correlated lattice systems. The manuscript is organised as follows.

In Chapter 1, we present an introduction to open many-body quantum systems. After describing the main physical systems, we introduce the master equation formalism and the main state-of-the-art numerical methods. An introduction to the main concepts of dissipative phase transitions is also presented.

In Chapter 2, we present our original results on dynamical optical hysteresis of a driven-dissipative nonlinear quantum resonator.

Chapter 3 presents the original method for the investigation of driven-dissipative many-body systems, which has been developed in our group: the corner-space renormalization method.

Chapters 4 and 5 present studies of many-body systems using the corner-space renormalization method and other techniques. In Chapter 4, we investigate the phase transition from a paramagnetic to a ferromagnetic phase in the dissipative anisotropic Heisenberg XYZ model. In Chapter 5, we predict a dissipative phase transition for the Bose-Hubbard model in the presence of incoherent driving.

Final conclusions and perspectives are drawn in the final chapter.

Chapter 1

Introduction to open many-body quantum physics

In the general introduction we have pointed out that the presence of driving and losses makes the study of open quantum systems rather different from the study of systems at equilibrium. This chapter aims at introducing the main physical systems, theoretical concepts and methods.

In the first section, we will present two relevant experimental platforms for the study of open many-body quantum systems, namely semiconductor microcavities and superconducting circuits. In section 1.2 we introduce the master equation formally describing the dynamics of such systems in the case of a weak coupling between the system and the environment. In section 1.3, we describe two important methods for the simulation of the master equation. Firstly, the Montecarlo wavefunction algorithm [61, 62, 63] that maps the master equation into the stochastic evolution of quantum states. Secondly, the Matrix Product Operator [14, 15] method, which is a powerful technique to solve one-dimensional systems. Finally in section 1.4, an introduction to dissipative phase transitions is given.

1.1 Examples of physical systems

In this section, we detail two of the most important experimental platforms for the study of open quantum many-body systems, namely, semiconductor microstructures and superconducting circuits. These two platforms can be tailored to create lattices of photonic cavities with effective photon-photon interaction. These systems are intrinsically open because of the unavoidable photon losses. The presence of a pump is necessary to compensate the dissipation by injecting photons. The photon-photon interactions are mediated by electronic excitations [30]. In the case of semiconductor microcavities, the nonlinear optical medium is given by quantum wells. As for superconductor quantum circuits, the nonlinearity is provided by Josephson junctions.

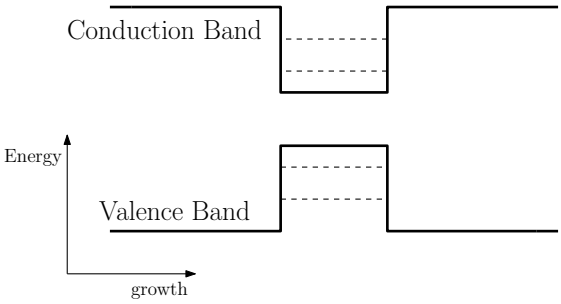

Figure 1.1: Band structure of a quantum well along the growth direction. The dashed lines represent the energy levels of quantum confined subbands.

1.1.1 Semiconductor microcavities

In undoped semiconductors, the lowest energy excitations are excitons. When light is shined on a semiconductor, an electron from the valence band is promoted to the excitation band and a hole appears in the valence band. It is energetically favourable for the electron and the hole to bind via Coulomb interaction and form an exciton. In order to further confine the electron-hole pair and increase the binding energy, a quantum well is used. This is a heterostructure that is obtained by growing a thin layer of a semiconductor with an energy gap E_g (between the valence and conduction bands) between two layers of a semiconductor with a band gap $E'_g > E_g$, as represented in Fig. 1.1.

In order to maximize the light-matter coupling in these systems, the photons are confined using Bragg mirrors. In such microcavity systems, it is possible to reach the strong light-matter coupling regime: the elementary excitations are the so-called polaritons, hybrid light-matter particles. These microcavity systems have been a prominent platform for the exploration of the many-body physics of exciton-polaritons. Indeed, phenomena such as the Bose-Einstein condensation of polariton gases [32] and polariton superfluidity [33] have been demonstrated in semiconductor microcavities.

Lattice systems of coupled micropillars with arbitrary geometry can be created by lithographic etching of planar cavities (see Ref. [68] for a review). In such micropillars, the lateral confinement of the polaritons is ensured by the difference of index between the semiconductor and the air surrounding it (see the inset of Fig. 1.2).

For resonant excitation, the micropillar can be considered as a single-mode cavity where the polariton-polariton interaction takes the form of a $\chi^{(3)}$ nonlinearity [69] leading to the Hamiltonian ($\hbar = 1$):

$$\hat{H} = \omega_c \hat{a}^\dagger \hat{a} + \frac{U}{2} \hat{a}^\dagger \hat{a}^\dagger \hat{a} \hat{a}, \tag{1.1}$$

with ω_c being the frequency of the polariton mode and U the strength of the non-linearity. The operator $\hat{a}$ is here the polariton annihilation operator.

The micropillars can be coupled by a nearest-neighbour hopping, which is theoreti-

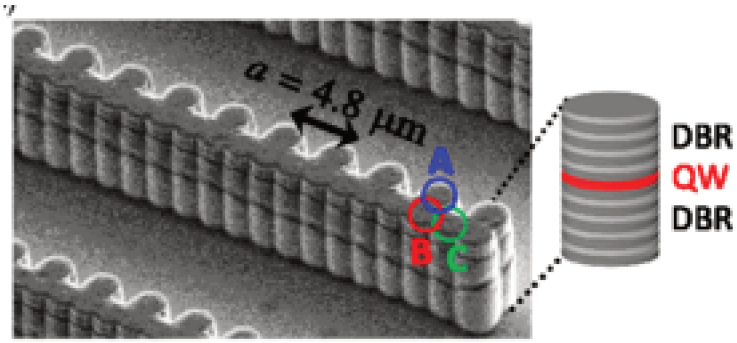

Figure 1.2: Scanning electron microscopy image of a one-dimensional Lieb lattice of semiconductor micropillars. The circles indicate the unit cell with three sites. The inset represents a single pillar with the two Bragg mirrors (DBR) and the quantum well (QW) in the middle that induces the non-linearity. From Ref. [71].

cally accounted for by the Hamiltonian:

$$\hat{H}_{hop} = -J \sum_{<i,j>} \hat{a}_i^\dagger \hat{a}_j, \tag{1.2}$$

where the operators $\hat{a}_j$, $\hat{a}_i$ represent the annihilation operators on the ith and jth sites and J is the hopping rate. This Hamiltonian is implemented thanks to the finite overlap between the optical modes in neighbouring micropillars. Using this scheme, it is possible to build artificial molecules [70] as well as one-dimensional [71, 72] and two-dimensional [73] lattices. An example of such lattice is shown in Fig. 1.2. In the case of semiconductor microcavity lattices, the demonstrated nonlinearities are yet moderate ($U \lesssim 10^{-2}\gamma$ where γ is the cavity loss rate), but the disorder is extremely small (comparable or smaller than γ).

1.1.2 Superconducting circuits

Another promising type of platform for the realization of open many-body quantum systems is offered by superconducting circuits. The basic building block of these circuits are LC resonators composed of a capacitor C and an inductance L. Such linear circuits can be described by the quadratic Hamiltonian [74]:

$$\hat{H} = \frac{1}{2C}\hat{Q}^2 + \frac{L}{2}\hat{\phi}^2, \tag{1.3}$$

where the operator $\hat{Q}$ is the charge of the capacity and $\hat{\phi}$ is the magnetic flux through the inductor. These operators obey the commutation rules $[\hat{Q}, \hat{\phi}] = -\mathrm{i}$.

In these systems, the nonlinearity is achieved thanks to Josephson junctions, hybrid structures composed of two superconductors separated by a thin insulating barrier. The Cooper pairs of the superconducting material can tunnel through the insulating barrier.

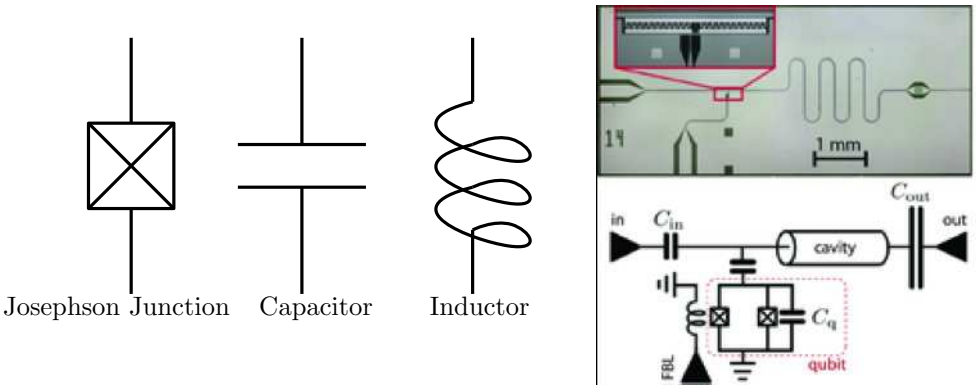

Figure 1.3: Left panel: schematic representation of a Josephson junction, a capacitor and an inductor. Right Panel: realization of the Jaynes-Cummings model using a transmission line resonator and a Josephson artificial atom. From Ref. [78].

There exist many different ways to integrate these elements in a circuit leading to different types of artificial two-level systems (qubits) [75]. An example of such nonlinear element is given on the right panel of Fig. 1.3: a transmon qubit [76, 77] composed of two Josephson junctions connected to the cavity through two capacitors. This system was used to implement the Jaynes-Cummings Hamiltonian [79]:

$$\hat{H} = \omega_c \hat{a}^\dagger \hat{a} + \omega_{at} \hat{\sigma}_z + g(\hat{a}^\dagger \hat{\sigma}^- + \hat{\sigma}^+ \hat{a}), \tag{1.4}$$

where the operators $\hat{\sigma}^-$, $\hat{\sigma}^+$ and $\hat{\sigma}_z$ are the Pauli matrices acting on the two-level system Hilbert space and the operator $\hat{a}$ is the annihilation operator for the microwave photonic mode. The frequencies ω_c and ω_{at} are those for the bare cavity and the atomic resonance of the Josephson junction, while g is the vacuum Rabi coupling between the atom and the cavity.

Interaction in these systems can be giant: indeed, the photon blockade effect has been demonstrated in a spectacular way [37, 39]. When $g/\gamma \gg 1$ (γ is the dissipation rate), it is possible to inject an excitation resonantly. However, as shown in Fig. 1.4, due to the anharmonic spectrum and narrow linewidths, the injection of a second excitation is blocked, because off-resonant. The ability to produce giant nonlinearities in superconducting circuits makes this platform a promising tool for the realization of strongly correlated many-body states of light.

As in semiconductor microstructures, in superconducting platforms it is possible to couple the different resonators implementing a hopping coupling described by Eq. (1.2) in the Hamiltonian. Figure 1.5 shows a superconducting lattice of 72 LC resonators coupled to transmon qubits. The sites are forming a one-dimensional chain that is pumped at one end. Presently, the main limitation of circuit QED lattices is represented by disorder. The parameters of a single-site cavity are not perfectly controlled because they are very sensitive on nanometric details of the Josephson junction.

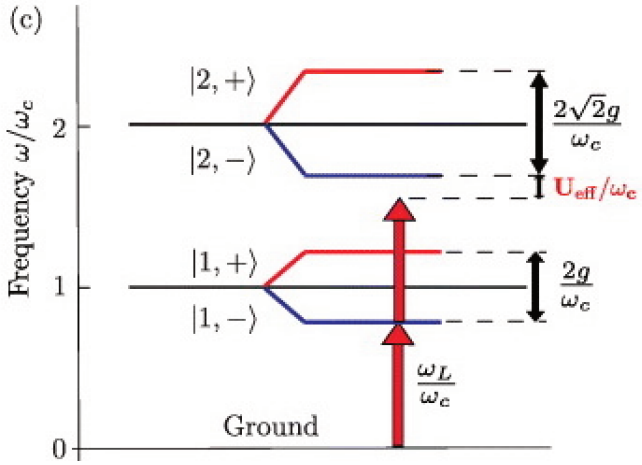

Figure 1.4: Energy levels of the Jaynes-Cummings Hamiltonian (1.4) for $\omega_{at} = \omega_c$. The red arrows represent the driving field on resonance with the single excitation transition, but detuned from the two excitation mode. This is the mechanism of photon blockade. From Ref. [80].

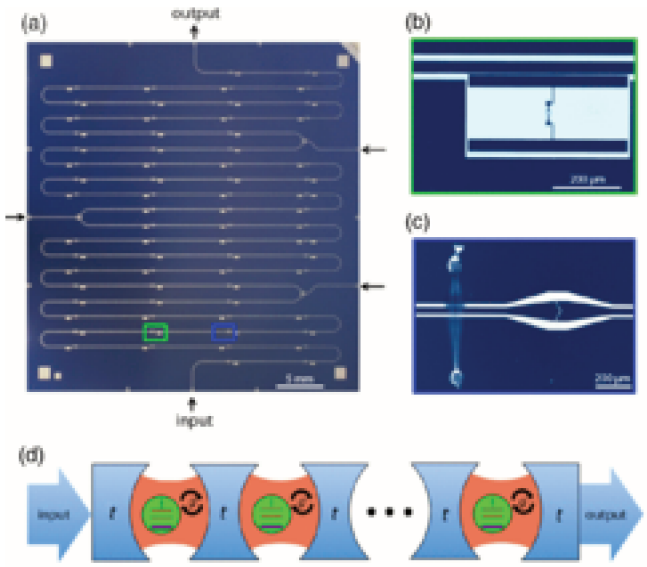

Figure 1.5: a) A view of the 72 resonators lattice on a 35×35 mm chip. b,c) The transmons qubits are coupled to the center of each resonator. d) Schematic view of the lattice. Form Ref. [81].

1.2 Dynamics of open quantum systems

The realization of many-body photonic phases on lattices were first proposed by three papers [34, 35, 36]. In these pioneering papers, the theory was at equilibrium and neglected the photonic losses. However, in order to gain a proper understanding of open many-body systems, it is necessary to take the dissipation processes into account. The dissipation is a result of the coupling between the system under study and the environment, typically represented by a bath consisting of an infinite number of modes. For example, in the case of photons, the bath is the ensemble of all electromagnetic modes in free space.

When energy is dissipated from the system to the bath, it is very unlikely that the reciprocal process takes place. As a result, the system undergoes a non-unitary evolution while the bath remains approximately in the same state. Thus, even in the limit of weak coupling, the dynamics of the system will be different from the unitary evolution of its equilibrium counterpart: the Hamiltonian of the system under study is not enough to give an accurate description of the dynamics.

In order to account for the dissipation processes, we will use a Lindblad master equation approach, that is derived in the following. The derivation detailed here is a standard procedure [82, 83, 84], based on several approximations that we will be discussed in the following. Firstly, we will perform the *Born approximation*, in the limit of weak coupling between the system and a large bath. Secondly, we will consider the *Markov approximation* assuming that the dynamics of the bath is much faster than the one of the system. Furthermore, we perform the *secular approximation* where the terms oscillating faster than the coupling strength are neglected. Following Ref. [82], we will apply the general result to the case of a single-mode resonator.

1.2.1 Liouville-von Neumann equation

First of all, we consider the Liouville-von Neumann equation for the total system. We consider a quantum system S described by the Hamiltonian $\hat{H}_S$ coupled to a bath B described by a Hamiltonian $\hat{H}_B$ with the interaction Hamiltonian $\hat{H}_{int}$. The total Hamiltonian $\hat{H}_T$ reads:

$$\hat{H}_T = \hat{H}_S + \hat{H}_{int} + \hat{H}_B. \tag{1.5}$$

The Liouville-von Neumann equation for the ensemble $S + B$ reads:

$$\partial_t \hat{\chi} = -\mathrm{i}[\hat{H}_T, \hat{\chi}], \tag{1.6}$$

where $\hat{\chi}$ is the total density matrix including the system and the bath. The reduced density matrix of the system $\hat{\rho}$ can be obtained from $\hat{\chi}$ by tracing out the bath degrees of freedom

$$\hat{\rho} = \mathrm{Tr}_B(\hat{\chi}). \tag{1.7}$$

The aim of the derivation is to obtain an equation of motion for the reduced density matrix of the system. A first step is to move into the interaction picture to focus on the interaction of the system S with the bath B

$$\hat{\chi}_I(t) = e^{\mathrm{i}(\hat{H}_S+\hat{H}_B)t}\hat{\chi}e^{-\mathrm{i}(\hat{H}_S+\hat{H}_B)t}. \tag{1.8}$$

The density matrix in the interaction picture follows the evolution equation:

$$\partial_t\hat{\chi}_I = -\mathrm{i}\left[\tilde{H}_{int}(t), \hat{\chi}_I(t)\right], \tag{1.9}$$

with the time-dependent Hamiltonian

$$\tilde{H}_{int}(t) = e^{(\mathrm{i}(\hat{H}_S+\hat{H}_B)t)}\hat{H}_{int}e^{(-\mathrm{i}(\hat{H}_S+\hat{H}_B)t)}. \tag{1.10}$$

We can then write a formal integral solution for $\hat{\chi}_I(t)$, namely

$$\hat{\chi}_I(t) = \hat{\chi}_I(t=0) - \mathrm{i}\int_0^t \mathrm{d}\tau\left[\tilde{H}_{int}(\tau), \hat{\chi}_I(\tau)\right]. \tag{1.11}$$

In order to obtain the Liouville-von Neumann equation in an integro-differential form, we inject the solution (1.11) into the master equation in the interaction picture (1.9):

$$\partial_t\hat{\chi}_I = -\mathrm{i}\left[\tilde{H}_{int}(t), \hat{\chi}(0)\right] - \int_0^t \mathrm{d}(\tau)\left[\tilde{H}_{int}(t), \left[\tilde{H}_{int}(\tau), \hat{\chi}_I(\tau)\right]\right]. \tag{1.12}$$

This equation is very hard to solve as it is, because of its integro-differential form and because it still contains all the degrees of freedom of the bath. In the following, we rely on the approximations mentioned above in order to get a workable differential equation for $\hat{\rho}_I(t) = \mathrm{Tr}_B(\hat{\chi}_I(t))$.

1.2.2 Equation for the system density matrix

Let us assume that there is no interaction between the bath and the system for $t \leq 0$. At time $t = 0$ the system and the bath will be uncorrelated. This means that the density operator will be of the form:

$$\hat{\chi}_I(0) = \hat{\chi}(0) = \hat{\rho}(0) \otimes \hat{R}, \tag{1.13}$$

where $\hat{R}$ is the density matrix of the bath. This also implies that at $t = 0$, we have:

$$\mathrm{Tr}_B(\hat{\chi}\hat{H}_{int}) = 0. \tag{1.14}$$

We assumed that the coupling between the system and the bath is weak. This means that the correlations between the system and the bath can be neglected, which leads to the approximated density operator at time t:

$$\hat{\chi}_I(t) \approx \hat{\rho}_I(t) \otimes \hat{R}_I(t), \tag{1.15}$$

where $\hat{R}_I(t)$ is the density matrix of the bath at time t in the interaction picture. This approximation is commonly called the *Born approximation* [82]. Note that this approximation can lead to a state significantly different from the real one for the ensemble $S+B$ if a finite number of modes is considered for the bath. However, other approaches based on projective methods lead to a similar form [84].

Moreover, we assume that the bath is at thermal equilibrium, that is

$$\hat{R} = \frac{e^{-\hat{H}_B/(k_B T)}}{\mathrm{Tr}(e^{-\hat{H}_B/(k_B T)})}, \tag{1.16}$$

with k_B being the Boltzmann constant and T the temperature of the bath. Since $\hat{R}$ commutes with $\hat{H}_B$, we can simplify Eq. (1.15) and write $\hat{\chi}_I(t) \approx \hat{\rho}_I(t) \otimes \hat{R}$.

Injecting $\hat{\chi}_I(t) \approx \hat{\rho}_I(t) \otimes \hat{R}$ in Eq. (1.12) allows us to find an equation for the dynamics of the reduced density matrix:

$$\partial_t \hat{\rho}_I = -\int_0^t \mathrm{d}\tau \mathrm{Tr}_B \left(\left[\tilde{H}_{int}(t), \left[\tilde{H}_{int}(\tau), \hat{\rho}_I(\tau) \otimes \hat{R} \right] \right] \right). \tag{1.17}$$

Furthermore, in the limit of weak coupling between the system and the bath, the reduced density matrix in the interaction picture evolves very slowly. As a result, we perform the *Markov approximation* mentioned above, i. e., the evolution of $\hat{\rho}_I(t)$ does not depend on its previous values [84]:

$$\partial_t \hat{\rho}_I = -\int_0^t \mathrm{d}\tau \mathrm{Tr}_B \left(\left[\tilde{H}_{int}(t), \left[\tilde{H}_{int}(\tau), \hat{\rho}_I(t) \otimes \hat{R} \right] \right] \right). \tag{1.18}$$

This equation is often called the *master equation in the Born-Markov form* [82].

1.2.3 Lindblad master equation

Let us consider the general coupling Hamiltonian [84]:

$$\hat{H}_{int} = \sum_u \hat{s}_u \otimes \hat{B}_u, \tag{1.19}$$

where the operators $\hat{s}_u$ and $\hat{B}_u$ act respectively on the system and the bath. Furthermore, we also assume that the operators $\hat{s}_u$ can be decomposed as follow:

$$\hat{s}_u = \sum_\nu \hat{s}_u(\nu), \tag{1.20}$$

where $[\hat{H}_S, \hat{s}_u(\nu)] = -\nu \hat{s}_u(\nu)$ and $[\hat{H}_S, \hat{s}_u^\dagger(\nu)] = \nu \hat{s}_u^\dagger(\nu)$. As a result, in the interaction picture, we can write:

$$\tilde{H}_{int}(t) = \sum_{u,\nu} e^{-\mathrm{i}\nu t} \hat{s}_u(\nu) \otimes \hat{B}_u(t) = \sum_{u,\nu} e^{\mathrm{i}\nu t} \hat{s}_u^\dagger(\nu) \otimes \hat{B}_u^\dagger(t). \tag{1.21}$$

If we decompose the double commutator in Eq. (1.18), we obtain:

$$\partial_t \hat{\rho}_I = -\int_0^t \mathrm{d}\tau \mathrm{Tr}_B \left(\tilde{H}_{int}(t)\hat{H}_{int}(\tau)\hat{\rho}_I(t) \otimes \hat{R} - \hat{H}_{int}(t)\hat{\rho}_I(t) \otimes \hat{R}\hat{H}_{int}(\tau) + H.C. \right), \tag{1.22}$$

where $H.C.$ is the Hermitian conjugate. We now substitute $\hat{H}_{int}(t) = \sum_{u,\nu} \exp(\mathrm{i}\nu t)\hat{s}_u^\dagger(\nu)\hat{B}_u^\dagger(t)$ and $\hat{H}_{int}(\tau) = \sum_{l,\nu'} \exp(-\mathrm{i}\nu'\tau)\hat{s}_l(\nu')\hat{B}_l(\tau)$:

$$\partial_t \hat{\rho}_I = \sum_{u,l}\sum_{\nu,\nu'} \int_0^t \mathrm{d}\tau e^{\mathrm{i}(\nu t - \nu'\tau)} \mathrm{Tr}_B \left(\hat{R}\hat{B}_u^\dagger(t)\hat{B}_l(\tau) \right) \left[\hat{s}_l(\nu')\hat{\rho}_I(t), \hat{s}_u^\dagger(\nu) \right] + H.C. \,. \tag{1.23}$$

It is convenient to introduce the correlation function of the bath [83]:

$$\begin{aligned} G_{u,l}(t,t') &= \mathrm{Tr}_B \left(\hat{R}\hat{B}_u^\dagger(t)\hat{B}_l(t') \right), \\ &= \mathrm{Tr}_B \left(\hat{R}\hat{B}_u^\dagger(t-t')\hat{B}_l \right), \\ &= G_{u,l}(t-t'). \end{aligned}$$

Performing the change of variable $\tau' = t - \tau$ in Eq. (1.23), the equation for the reduced density matrix reads:

$$\partial_t \hat{\rho}_I = \sum_{u,l}\sum_{\nu,\nu'} e^{\mathrm{i}(\nu-\nu')t} \int_0^t \mathrm{d}\tau' e^{\mathrm{i}\nu'\tau'} G_{u,l}(\tau') \left[\hat{s}_l(\nu')\hat{\rho}_I(t), \hat{s}_u^\dagger(\nu) \right] + H.C. \,. \tag{1.24}$$

In the limit of weak coupling to the bath, terms oscillating at a frequency much larger than the coupling will be averaged to 0. This was introduced as the *secular approximation* in the beginning of the derivation. As a result, only the terms with $\nu = \nu'$ in Eq. (1.24) will have a significant contribution, giving:

$$\partial \hat{\rho}_I = \sum_{\nu}\sum_{u,l} \Gamma_{u,l}(\nu) \left[\hat{s}_l(\nu)\hat{\rho}_I(t), \hat{s}_u^\dagger(\nu) \right] + \Gamma_{l,u}^*(\nu) \left[\hat{s}_l(\nu), \hat{\rho}_I(t)\hat{s}_u^\dagger(\nu) \right], \tag{1.25}$$

where we introduced the quantity:

$$\Gamma_{u,l}(\nu) = \int_0^t \mathrm{d}\tau e^{\mathrm{i}\nu\tau} \mathrm{Tr}_B \left(\hat{R}\hat{B}_u^\dagger(\tau)\hat{B}_l \right). \tag{1.26}$$

Furthermore, another consequence of the weak coupling hypothesis is that the characteristic time for the decay of bath correlations will be much smaller than the characteristic timescale of the reduced density matrix evolution. Thus, we can take $t \to \infty$ in the upper bound of the previous integral.

Finally, if we introduce the following quantities [84]:

$$S_{u,l}(\nu) = \frac{1}{2\mathrm{i}}(\Gamma_{u,l}(\nu) - \Gamma_{l,u}(\nu)^*), \tag{1.27}$$

$$\gamma_{u,l}(\nu) = \Gamma_{u,l}(\nu) + \Gamma_{l,u}(\nu)^* = \int_{-\infty}^{\infty} \mathrm{d}\tau e^{\mathrm{i}\nu\tau} G_{u,l}(\tau), \tag{1.28}$$

we obtain the Lindblad master equation in the interaction picture

$$\partial_t \hat{\rho}_I = -\mathrm{i}\left[\hat{H}_{LS}, \hat{\rho}_I\right] + L[\hat{\rho}_I], \tag{1.29}$$

where the Lamb Shift Hamiltonian $\hat{H}_{LS}$ reads

$$\hat{H}_{LS} = \sum_{\nu} \sum_{u,l} S_{u,l}(\nu) \hat{s}_u^\dagger(\nu) \hat{s}_l(\nu), \tag{1.30}$$

and the Lindblad term reads

$$L[\hat{\rho}_I] = \sum_{\nu} \sum_{u,l} \gamma_{u,l}(\nu) \left[\hat{s}_l(\nu) \hat{\rho}_I \hat{s}_u^\dagger(\nu) - \frac{1}{2}\left(\hat{s}_u^\dagger(\nu)\hat{s}_l(\nu)\hat{\rho}_I + \hat{\rho}_I \hat{s}_u^\dagger(\nu)\hat{s}_l(\nu)\right)\right]. \tag{1.31}$$

This leads to the Lindblad master equation:

$$\partial_t \hat{\rho} = -\mathrm{i}\left[\hat{H}_S + \hat{H}_{LS}, \hat{\rho}\right] + L[\hat{\rho}]. \tag{1.32}$$

To give a concrete example, let us consider an optical cavity with a single decay channel and a single mode with frequency $\nu = \omega_0$ [82]. We have

$$\tilde{s}(t) \approx \hat{a} e^{-\mathrm{i}\omega_0 t}, \tag{1.33}$$

where $\hat{a}$ is the annihilation operator for the resonator. The coupling Hamiltonian then reads:

$$\hat{H}_{int}(t) = \hat{a} e^{-\mathrm{i}\omega_0 t} \hat{C}^\dagger(t) + \hat{a}^\dagger e^{\mathrm{i}\omega_0 t} \hat{C}(t), \tag{1.34}$$

where we introduced the operator $\hat{C} = \hat{B}^\dagger$. In our case, the quantities $\gamma_{u,l}(\omega_0)$ read [82]:

$$\gamma_1 = \int_{-\infty}^{\infty} \mathrm{d}\tau e^{\mathrm{i}\omega_0 \tau} \mathrm{Tr}_B(\hat{R}\hat{C}^\dagger(\tau)\hat{C}) = \gamma n_{th}, \tag{1.35}$$

$$\gamma_2 = \int_{-\infty}^{\infty} \mathrm{d}\tau e^{\mathrm{i}\omega_0 \tau} \mathrm{Tr}_B(\hat{R}\hat{C}(\tau)\hat{C}^\dagger) = \gamma(n_{th}+1), \tag{1.36}$$

where γ is the linewidth of the cavity and n_{th} is the thermal occupation of the bath at frequency ω_0. Note that since the correlators $\mathrm{Tr}_B(\hat{R}\hat{C}^\dagger(\tau)\hat{C}^\dagger) = 0$ and $\mathrm{Tr}_B(\hat{R}\hat{C}(\tau)\hat{C}) = 0$, the terms with $u \neq l$ in Eq. (1.31) are not contributing. Moreover, the shift Hamiltonian $\hat{H}_{LS} \propto \delta \hat{a}^\dagger \hat{a}$ introduces a shift δ in the frequencies of the system. It will be omitted in the following.

In conclusion, the master equation reads:

$$\begin{aligned}\partial_t \hat{\rho} = &-\mathrm{i}\left[\hat{H}_S, \hat{\rho}\right] \\ &+ \frac{\gamma(n_{th}+1)}{2}\left(\hat{a}\hat{\rho}\hat{a}^\dagger - \hat{a}^\dagger\hat{a}\hat{\rho} - \hat{\rho}\hat{a}^\dagger\hat{a}\right) \\ &+ \frac{\gamma n_{th}}{2}\left(\hat{a}^\dagger\hat{\rho}\hat{a} - \hat{a}\hat{a}^\dagger\hat{\rho} - \hat{\rho}\hat{a}\hat{a}^\dagger\right).\end{aligned} \tag{1.37}$$

For nonlinear systems, taking the annihilation operator of the resonator mode remains a good approximation as long as the strength of the interaction remains smaller

than the transition energy of the matter or cavity degrees of freedom [85]. In the ultra-strong coupling regime, the master equation needs to be modified [86]. In the following of this thesis, we are not considering such cases. As a result, the general form of the master equation will be:

$$\partial_t \hat{\rho} = -\mathrm{i}[\hat{H}_S, \hat{\rho}] + \frac{1}{2}\sum_k \gamma_k \left(2\hat{a}_k \hat{\rho} \hat{a}_k^\dagger - \hat{a}_k^\dagger \hat{a}_k \hat{\rho} - \hat{\rho}\hat{a}_k^\dagger \hat{a}_k\right), \tag{1.38}$$

where the operator $\hat{a}_k$ is the jump operator for the kth dissipation channel and γ_k is the associated loss rate.

1.2.4 Properties of the Lindblad master equation

The previous master equation (1.38) can be written in a more synthetic way:

$$\partial_t \hat{\rho} = \mathcal{L}\hat{\rho}, \tag{1.39}$$

where we introduced the Liouvillian super-operator:

$$\mathcal{L}\hat{\rho} = -\mathrm{i}[\hat{H}_S, \hat{\rho}] + \frac{1}{2}\sum_k \left(2\hat{a}_k \hat{\rho} \hat{a}_k^\dagger - \hat{a}_k^\dagger \hat{a}_k \hat{\rho} - \hat{\rho}\hat{a}_k^\dagger \hat{a}_k\right). \tag{1.40}$$

The Liouvillian superoperator is a linear map acting on operators. It implies also that the Liouvillian superoperator can be recast as a matrix acting on the density operator seen as a vector. As a result, we can write the eigenvalue equation:

$$\mathcal{L}\hat{\rho}_\lambda = \lambda \hat{\rho}_\lambda, \tag{1.41}$$

where the different eigenvalues λ are complex numbers. The eigenvalues λ have to fulfil the condition $\mathrm{Re}(\lambda) \leq 0$, with the steady-state density matrix $\hat{\rho}_{SS}$ corresponding to $\lambda = 0$.

Contrary to unitary evolutions, which map a pure state into another pure state, the master equation maps the initial state into a potentially mixed state. The density matrix can be diagonalized to find its eigenstates and their respective probabilities:

$$\hat{\rho} = \sum_n p_n |\psi_n\rangle\langle\psi_n|. \tag{1.42}$$

The normalisation condition is expressed as:

$$\mathrm{Tr}(\hat{\rho}) = \sum_n p_n = 1. \tag{1.43}$$

The trace of the density matrix is of course conserved by the unitary term of Eq. (1.38). Moreover, since $\mathrm{Tr}(L[\hat{\rho}]) = 0$, the trace is also conserved by the Lindblad master equation.

1.3 State-of-the-art numerical methods

Analytical solutions of the master equation (1.38) are limited to particular cases, so it is important to have numerical methods to solve it. In order to be able to numerically deal with Hilbert spaces of infinite dimension, it is necessary to truncate the Hilbert space conserving only the relevant states. For example, if we consider a single-mode optical cavity, the dimension of the Hilbert space is infinite. However, the losses will limit the number of photons. In the Fock number basis, this is translated in a cutoff $N_{\max}$ so that the basis for the truncated Hilbert space is:

$$\{|0\rangle, |1\rangle, \ldots, |N_{\max}\rangle\}\,. \tag{1.44}$$

Of course, it is mandatory to test the convergence by checking that the results are not changed if a larger value of the cutoff $N_{\max}$ is considered.

When studying extended systems, the dimension of the Hilbert space grows exponentially. If a site is accurately described in a Hilbert space $\mathcal{H}_1$ of dimension $\dim(\mathcal{H}_1) = N_{\max}+1$, then the dimension of the Hilbert space for a lattice of m sites will be:

$$\dim(\mathcal{H}) = \dim\left(\bigotimes_{i=1}^{m}\mathcal{H}_1^{(i)}\right) = (N_{\max}+1)^m. \tag{1.45}$$

This exponentially increases the dimension of the Hilbert space representing an important limitation on the number of sites that can be handled by brute-force calculations.

1.3.1 Montecarlo wavefunction method

When the dimension of the Hilbert space becomes large, it is not possible to store the density matrix into the computer memory. A method which allows to improve a bit this problem is the Montecarlo Wavefunction algorithm proposed by J. Dalibard *et al.* [61, 62] and H. J. Carmichael [63]. First, note that the master equation given by Eq. (1.38) can be written as

$$\partial_t\hat{\rho} = -\mathrm{i}\left(\hat{H}_{nh}\hat{\rho} - \hat{\rho}\hat{H}_{nh}^{\dagger}\right) + \sum_k \gamma_k \hat{a}_k\hat{\rho}\hat{a}_k^{\dagger}, \tag{1.46}$$

where the operator $\hat{H}_{nh}$ reads

$$\hat{H}_{nh} = \hat{H}_S - \mathrm{i}\sum_k \frac{\gamma_k}{2}\hat{a}_k^{\dagger}\hat{a}_k. \tag{1.47}$$

The key point of the Montecarlo Wavefunction method is to consider the stochastic evolution of states $|\Psi_i\rangle$ instead of the evolution of the density matrix, which is recovered by averaging over N_{traj} individual quantum trajectories:

$$\hat{\rho} = \lim_{N_{traj}\to\infty}\frac{1}{N_{traj}}\sum_{i=1}^{N_{traj}}|\Psi_i\rangle\langle\Psi_i|. \tag{1.48}$$

The time evolution of the states $|\Psi_i\rangle$ is the sum of two contributions. The first one is a Schrödinger-like evolution associated with the non-Hermitian Hamiltonian $\hat{H}_{nh}$. The second contribution to the dynamics is due to quantum jumps accounting for the second term of Eq. (1.46). In the next section, we will detail the algorithm for the evolution of a state $|\Psi\rangle$.

Algorithm for the evolution of a single quantum trajectory

Let us consider a trajectory $|\Psi(t)\rangle$ for the state of the system. In order to compute the evolution from time t to $t+\delta t$, we start by generating a random number ϵ with an uniform distribution between 0 and 1. We then compute the probability for a jump to occur between t and $t+\delta t$ as follows:

$$\delta p = \delta t \langle\Psi| \sum_k \gamma_k \hat{a}_k^\dagger \hat{a}_k |\Psi\rangle. \tag{1.49}$$

If $\delta p > \epsilon$, we consider the non-unitary evolution:

$$|\bar{\Psi}(t+\delta t)\rangle = \frac{1}{1-\delta p}(1 - \mathrm{i}\delta t \hat{H}_{nh})|\Psi(t)\rangle. \tag{1.50}$$

Note that since the norm is not conserved by the $\hat{H}_{nh}$ term, we have normalized $|\bar{\Psi}(t+\delta t)\rangle$ by $1-\delta p$.

If $\delta p < \epsilon$, instead, a quantum jump is enforced. To do so, one first computes the probabilities associated with each channel:

$$\delta p_k = \frac{\gamma_k}{\delta p}\langle\Psi(t)|\hat{a}_k^\dagger \hat{a}_k|\Psi(t)\rangle. \tag{1.51}$$

Then, one has to generate another random number ϵ' and compute the cumulative probabilities:

$$p_i = \sum_{j\leq i} \delta p_j. \tag{1.52}$$

The next step is to compare ϵ' with the different p_i and select the jump operator $\hat{a}_i$ that verify $p_i \leq \epsilon' < p_{i+1}$. This is equivalent to generating a random integer i following the probability distribution given by the probabilities δp_i. The new state is calculated as

$$|\Psi(t+\delta t)\rangle = \frac{\hat{a}_i|\Psi(t)\rangle}{\sqrt{\langle\Psi(t)|\hat{a}_i^\dagger \hat{a}_i|\Psi(t)\rangle}}. \tag{1.53}$$

Computation of the density matrix

We now show that the density matrix can be recovered from the trajectories computed using the algorithm given in the previous section. Let us first consider the evolution of the operator $\sigma(t) = |\Psi(t)\rangle\langle\Psi(t)|$:

$$\sigma(t+\delta t) = (1-\delta p)\frac{|\bar{\Psi}(t)\rangle}{\sqrt{1-\delta p}}\frac{\langle\bar{\Psi}(t)|}{\sqrt{1-\delta p}} + \delta p \sum_i \delta p_i \frac{\hat{a}_i|\Psi(t)\rangle}{\sqrt{\langle\Psi(t)|\hat{a}_i^\dagger\hat{a}_i|\Psi(t)\rangle}}\frac{\langle\Psi(t)|\hat{a}_i^\dagger}{\sqrt{\langle\Psi(t)|\hat{a}_i^\dagger\hat{a}_i|\Psi(t)\rangle}}. \tag{1.54}$$

The first term of this expression represents the non-Hermitian evolution occurring with a probability $1 - \delta p$, whereas the second term takes the quantum jumps into account. By including the expression of equation (1.50) in (1.54), and averaging over all the trajectories, we get:

$$\hat{\rho}(t+\delta t) = \hat{\rho}(t) - \mathrm{i}\delta t[\hat{H}, \hat{\rho}(t)] + \frac{\delta t}{2} \sum_i \gamma_i \left(2\hat{a}_i \hat{\rho}(t) \hat{a}_i^\dagger - \hat{a}_i^\dagger \hat{a}_i \hat{\rho}(t) - \hat{\rho}(t) \hat{a}_i^\dagger \hat{a}_i \right). \quad (1.55)$$

This shows that $\hat{\rho}$ do solve the Lindblad master equation.

It is worth noting that within the quantum measurement formalism, the trajectories $|\Psi_i(t)\rangle$ have actually a physical meaning [87, 88]. Indeed, these trajectories can be seen as the result of a photon counting process where photons escaping the cavity induce the quantum jumps.

1.3.2 Matrix Product Operator (MPO) methods

In lattice systems, the exponential growth of the Hilbert space dimension is the main limitation in the accessible simulations. Even when a Montecarlo wavefunction algorithm is used, the manageable lattice sizes remain limited. For example, if we consider an ensemble of 16 two-level systems, the Hilbert space dimension is already $2^{16} = 65536$, which is close to the computational limits of a desktop computer. As a result, it is necessary to find methods to efficiently truncate the Hilbert space.

For one-dimensional systems, a very powerful method is the density matrix renormalization group [8]. New sites are added to the lattice in an iterative way. The array is divided into two equivalent blocks and their Hilbert space is truncated. This truncation is based on the selection of the most probable states of the reduced density matrix, obtained by tracing one of the blocks out of the ground state of the Hamiltonian for the ensemble of the two blocks.

More formally, the DMRG algorithm is based on the following steps:

1. Construct the blocks B_l and its mirror symmetric B_l^R.
2. Add a site to B_l and construct the Hamiltonian $\hat{H}_l$ for $B_l \bullet \bullet B_l^R$.
3. Diagonalize $\hat{H}_l$ to get its ground state.
4. Trace out the right hand side of the system to obtain the reduced density matrix $\hat{\rho}_{l+1}^L$ for $B_{l+1} = B_l \bullet$.
5. Diagonalize $\hat{\rho}_{l+1}^L$. The m eigenstates with the largest probabilities are used to construct a base for B_{l+1}.
6. Write all the operators for B_{l+1} in the truncated basis.
7. Repeat from step 2 until the desired number of sites is reached.

Furthermore, it was shown that the states simulated using DMRG are Matrix Product States [9, 10, 11] of the form:

$$|\Psi\rangle = \sum_{i_1=0}^{n-1} \cdots \sum_{i_N}^{n-1} c_{i_1,i_2,\ldots,i_N} |i_1\rangle |i_2\rangle \cdots |i_N\rangle. \tag{1.56}$$

The particularity of these states is that the coefficients $c_{i_1,i_2,\ldots,i_N}$ can be written as product of tensors:

$$c_{i_1,\ldots,i_N} = A^{[i_1]} A^{[i_2]} \cdots A^{[i_{N-1}]} A^{[i_N]}, \tag{1.57}$$

where the $A^{[u]}$ are non square matrices obtained using singular value decompositions (SVD), whose dimension increases exponentially when approaching the center of the lattice. The main interest of such formulation is that it allows a variational determination of the coefficient $c_{i_1,i_2,\ldots,i_N}$. In particular, this speeds up the time integration of dynamical systems [16]. In order to have efficient computations, the result of the SVD is truncated, keeping only the χ most significant singular values, where χ is called the bond link dimension. More details can be found for example in Ref. [89].

It is possible to extend the Matrix Product State formalism to operators, giving the so-called Matrix Product Operator (MPO) methods [14, 15]. They simulate open one-dimensional systems as well as thermalization problems. The density operator is recast as a vector (a so-called "super-ket") and the super-operator $\mathcal{L}$ is seen as a linear map acting on the super-kets. As for MPS, the super-ket representing the density operator is decomposed as

$$|\rho\rangle\rangle = \sum_{i_1=0}^{n^2-1} \cdots \sum_{i_N=0}^{n^2-1} c_{i_1,i_2,\ldots,i_N} |i_1\rangle\rangle \otimes |i_2\rangle\rangle \otimes \cdots \otimes |i_N\rangle\rangle, \tag{1.58}$$

where $|\rho\rangle\rangle$ and the different $|i_u\rangle\rangle$ are operators recast as kets forming a local base of dimension n^2. The coefficients c are decomposed on tensors using a succession of singular value decompositions (SVD):

$$c_{i_1,\ldots,i_N} = A^{[i_1]} A^{[i_2]} \cdots A^{[i_{N-1}]} A^{[i_N]}, \tag{1.59}$$

The vectorized density operator is then evolved using the so-called time-evolution block-decimation method until it reaches its steady state [15].

Lately this method has been improved thanks to two independent works [44, 43] where the steady state is found by minimizing $\|\mathcal{L}|\rho\rangle\rangle\|$ rather than by time evolution. Note that whereas $\mathcal{L}$ was directly minimized in Ref. [44], $\mathcal{L}^\dagger\mathcal{L}$ was used in Ref. [43]. The minimization is then performed locally on each site successively in one direction and then in the other direction. Convergence is reached after several of such optimization sweeps.

The different MPO based methods presented above are known to be efficient for one-dimensional systems with local interactions. There has been a recent proposal to simulate two dimensional open lattices based on projected entanglement pairs [45]. This formalism is an extension of the MPO description and implies to challenging implementations.

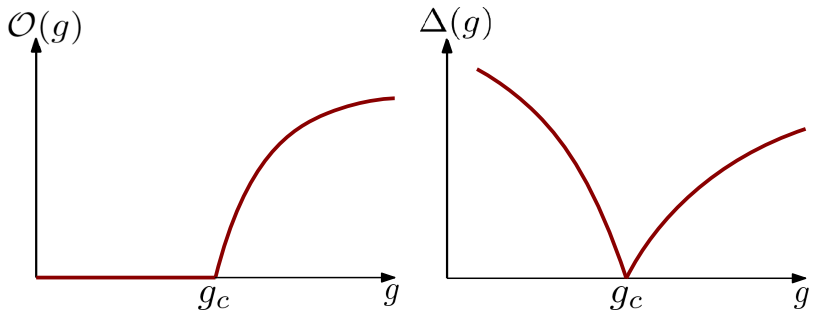

Figure 1.6: Typical behaviour of the order parameter $\mathcal{O}(g)$(left panel) and of the energy gap $\Delta(g)$ as a function of the parameter g for a second-order (continuous) phase transition.

1.4 Definition of dissipative quantum phase transitions

Among the different type of phenomena that can be observed in correlated driven-dissipative systems, we would like to concentrate on dissipative quantum phase transitions. Due to the dissipative nature of the system, these transitions cannot be treated like quantum phase transitions at equilibrium [23, 24]. In Chapters 2, 4 and 5, we will explore several models exhibiting such dissipative phase transitions.

At zero temperature, a quantum phase transition is the non-analytic change of many-body ground state properties when a parameter g of the system Hamiltonian $\hat{H}(g)$ is varied [23]. If we consider the gap $\Delta(g)$ between the ground state energy and the energy of the first excited state, at the critical point $g = g_c$ we have $\Delta(g_c) = 0$. At this point, ground state observables have a singular behaviour. The typical behaviour of the gap $\Delta(g)$ is represented as a function of g in the right panel of Fig. 1.6. A transition breaking a symmetry is described by an order parameter. For example, when studying the Mott Insulator to superfluid phase transition in the Bose-Hubbard model at equilibrium [26], the superfluid phase is characterized by a non-zero coherence. When the coherence is studied across the transition, it vanishes in the Mott-Insulator phase. The behaviour of order parameters is schematically represented for a second-order phase transition on the left panel of Fig. 1.6.

As we have seen in section 1.2, the Hamiltonian alone is not enough to describe the dynamics of open quantum systems: one needs to know the Liouvillian superoperator $\mathcal{L}$. We can write $\mathcal{L}(g)$ to express the fact that it depends on a parameter g. In a dissipative system, the analogous of the ground state is the steady state described by the density matrix $\hat{\rho}_{SS}(g)$ such that $\partial_t \hat{\rho}_{SS}(g) = 0 = \mathcal{L}(g)\hat{\rho}_{SS}(g)$. At the critical point $g = g_c$, a dissipative phase transition is signalled by a non-analytic behaviour of the steady-state observables. The eigenvalue $\lambda(g)$ of the Liouvillian with the smallest real part (in absolute value) then plays a similar role to the energy gap $\Delta(g)$ in quantum phase transitions [90]. When the real part of the first non-zero eigenvalue vanishes, then the lifetime of the corresponding mode becomes infinite. Furthermore, as the eigenvalue

$\lambda(g)$ goes to zero, it becomes the most relevant one for the long term dynamics of the master equation: the relaxation to the steady state is slowed down and dominated by $\lambda(g)$. This effect is called critical slowing down, which has been recently studied in driven-dissipative lattice systems [59].

1.5 Conclusion

In this chapter, we have introduced the physics of open quantum many-body systems. We have discussed two relevant platforms, namely semiconductor microcavities and superconductor quantum circuits, as well as their lattice implementations of Hubbard models for photons. We have reviewed the general formalism of the master equation for the density matrix and some state-of-the-art numerical methods. Finally, we have introduced the main concepts for dissipative phase transitions.

Chapter 2

Single-site critical phenomena: dynamical optical hysteresis in the Kerr model

Since its first observation in 1976 [91], optical bistability has been an intensively studied subject (see Refs. [92, 93, 94, 95] for some recent examples). Experiments show the existence of two stable solutions for the field inside a non-linear optical cavity. From the theoretical point of view, this effect can be well described by a semiclassical analysis. However, at first sight the simple semiclassical theory of bistability seemed to be in contradiction with the exact steady-state solution found by Drummond and Walls in 1980 [96] for the Kerr model describing a single-mode cavity with a third order nonlinearity: the Drummond-Walls solution of the master equation is unique.

The key point is that the inclusion of quantum fluctuations induces switching between the semiclassical solutions [97, 98, 99, 56] resulting in a unique mixed steady state. Without fluctuations or for very weak nonlinearity, these lifetimes become very large so that the semiclassical behaviour is recovered. Note that the fluctuation-induced switching can be directly visualized by examining single quantum trajectories [100, 101]. Similar behaviour can be observed by adding classical fluctuations to the system, by adding noise in the drive [102, 103] or thermal fluctuations [104]. In general, it is possible to define a point where both semiclassical metastable solutions have equal lifetimes. Away from this transition point, one branch becomes increasingly more stable compared to the other. It is important to emphasize that this switching time can be extremely long compared to all other timescales, in particular the cavity photon lifetime. This explains why the semiclassical mean-field approach is successful for explaining the observed standard hysteresis of bistability.

In this chapter, we investigate the behaviour of the exact quantum solution when the pump amplitude is modulated in time. In this case, we show that for a finite modulation time the system exhibits a dynamical hysteresis loop. When the modulation timescale is increased, we observe that the hysteresis loop becomes smaller and eventually disappears

in the limit of infinitely slow modulations. Thus, our analysis shows the link between the semiclassical bistability and the exact unique steady state. Furthermore, we show the existence of a double power law in the hysteresis area as a function of the modulation speed. We emphasize that the results of this chapter are for a single-mode cavity for which exact numerical results can be obtained. The concepts presented here, however, can be extended to the many-mode case.

The first section of this chapter is a review of Kerr bistability. The second section contains the main results: the dynamical hysteresis is studied when a coherent drive with time-dependent amplitude is applied to the system. The effect of the amplitude sweep of the pump is investigated using different theoretical approaches.

This work on optical bistability was initiated with Wim Casteels under the direction of Cristiano Ciuti and led to a publication in *Physical Review A* [105]. The observation of the double power-law presented in section 2.3 is the result of a collaboration with the experimental group of Jacqueline Bloch and Alberto Amo at C2N. The experiments were mainly done by Said Rodriguez, resulting in a paper published in *Physical Review Letters* [106].

2.1 Semiclassical versus quantum theory of the steady state in the Kerr model

The Hamiltonian of a coherently driven Kerr non-linear cavity reads:

$$\hat{H} = \omega \hat{a}^\dagger \hat{a} + \frac{U}{2} \hat{a}^\dagger \hat{a}^\dagger \hat{a} \hat{a} + F(\hat{a}^\dagger e^{\mathrm{i}\omega_L t} + \hat{a} e^{-\mathrm{i}\omega_L t}), \tag{2.1}$$

where the operator $\hat{a}$ is the annihilation operator of the cavity mode, ω is the frequency of the optical mode and U quantifies the Kerr non-linearity. The laser pump is characterized by its amplitude F and its frequency ω_L. In order to eliminate the time dependence from the previous Hamiltonian, we can write the Hamiltonian in the frame rotating at the laser frequency ω_L:

$$\hat{H} = -\Delta \hat{a}^\dagger \hat{a} + \frac{U}{2} \hat{a}^\dagger \hat{a}^\dagger \hat{a} \hat{a} + F(\hat{a}^\dagger + \hat{a}), \tag{2.2}$$

with $\Delta = \omega_L - \omega$.

The photon losses occurring at a rate γ are taken into account using the Lindblad master equation:

$$\partial_t \hat{\rho} = -\mathrm{i}[\hat{H}, \hat{\rho}] + \frac{\gamma}{2} \left(2\hat{a}\hat{\rho}\hat{a}^\dagger - \hat{a}^\dagger \hat{a}\hat{\rho} - \hat{\rho}\hat{a}^\dagger \hat{a} \right), \tag{2.3}$$

where the density matrix $\hat{\rho}$ describes the cavity mode. Note that this master equation is valid for a bath at $T = 0K$, which is equivalent to a number of thermal excitations $n_{th} = 0$. In order to include thermal effect, we recall the master equation derived in the

previous chapter:

$$\partial_t\hat{\rho} = -\mathrm{i}[\hat{H},\hat{\rho}] + \frac{\gamma(n_{th}+1)}{2}\left(2\hat{a}\hat{\rho}\hat{a}^\dagger - \hat{\rho}\hat{a}^\dagger\hat{a} - \hat{a}^\dagger\hat{a}\right) + \frac{\gamma n_{th}}{2}\left(2\hat{a}^\dagger\hat{\rho}\hat{a} - \hat{\rho}\hat{a}\hat{a}^\dagger - \hat{a}\hat{a}^\dagger\hat{\rho}\right). \tag{2.4}$$

The Kerr model is rather general and can be obtained, e.g., in a system consisting of a coherently driven linear cavity coupled to an ensemble of two-level atoms in the dispersive limit (large detuning between the atoms and the cavity resonance frequency with respect to the coupling strength) [107]. In recent years, novel quantum optical systems with large nonlinearities such as superconducting quantum circuits and semiconductor microcavities have emerged (see Chapter 1). In semiconductor micropillars with embedded quantum wells, a normalized U/γ up to a few percent has been demonstrated. For these systems the low temperature $T = 4K$ (liquid helium bath) together with the cavity photon energy around 1.5 eV results in a negligible number of thermal photons $n_{th} \approx 0$. In the context of circuit QED, much larger non-linearities can be achieved $|U|/\gamma \gg 1$. A typical dilution fridge temperature of 50 mK and a resonator frequency of 5 GHz correspond to a thermal population of $n_{th} \simeq 0.008$ photons, which have a small but non-negligible impact on the solution. In the following, unless explicitly specified, the results are presented in the zero temperature limit ($n_{th} = 0$).

2.1.1 Mean-field equation for a single-mode Kerr cavity

To solve the Kerr model, the simplest approach is the mean-field one. Let us write the equation of motion for the intracavity field $\langle\hat{a}\rangle = \mathrm{Tr}(\hat{\rho}\hat{a})$:

$$\partial_t\langle\hat{a}\rangle = \left(-\mathrm{i}\Delta - \frac{\gamma}{2}\right)\langle\hat{a}\rangle + \mathrm{i}U\langle\hat{a}^\dagger\hat{a}\hat{a}\rangle - \mathrm{i}F. \tag{2.5}$$

The mean-field approximation is $\langle\hat{a}^\dagger\hat{a}\hat{a}\rangle \simeq |\langle\hat{a}\rangle|^2\langle\hat{a}\rangle$. Within this approximation, one finds a Gross-Pitaevskii-like equation for the field $\alpha = \langle\hat{a}\rangle$, namely

$$\partial_t\alpha = -\left(\mathrm{i}\Delta + \frac{\gamma}{2}\right)\alpha + \mathrm{i}U|\alpha|^2\alpha - \mathrm{i}F. \tag{2.6}$$

The cubic nonlinear equation (2.6) exhibits bistability. For some values of the parameters, it can admit two distincts stable steady-state solutions. In the steady state ($\partial_t\alpha = 0$), the number of photons $n = |\alpha|^2$ satisfies the following equation:

$$0 = U^2n^3 - 2\Delta Un^2 + \left(\Delta^2 + \left(\frac{\gamma}{2}\right)^2\right)n - F^2. \tag{2.7}$$

Let us introduce the function:

$$f(n) = U^2n^3 - 2\Delta Un^2 + \left(\Delta^2 + \left(\frac{\gamma}{2}\right)^2\right)n - F^2. \tag{2.8}$$

The solutions of Eq.(2.7) correspond to the zeros of function $f(n)$. If

$$\Delta > \frac{\sqrt{3}}{2}\gamma, \tag{2.9}$$

is verified, then $f(n) = 0$ has three distinct solutions. Furthermore, if we consider the derivative of the function (2.8), it is possible to analyse the stability of the different solutions: if $f'(n) > 0$ the solution is stable, otherwise it is not.

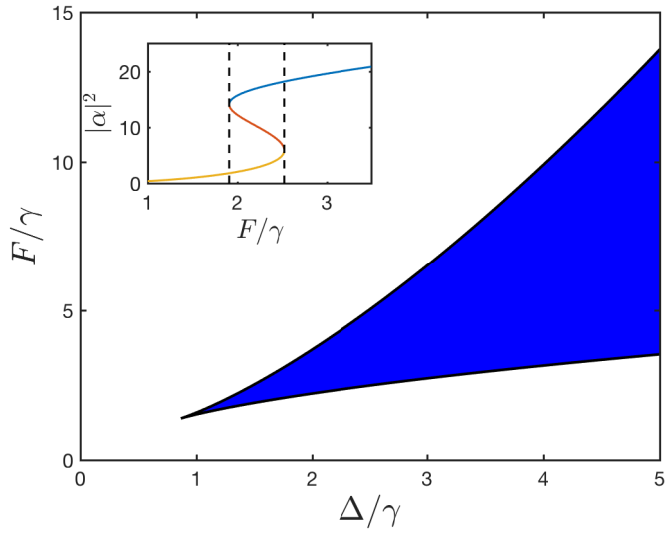

Figure 2.1: Phase diagram obtained from Eq. (2.7) in the (Δ, F) plan for $U = 0.1\gamma$. The white area corresponds to the monostable phase and the coloured area corresponds to the the bistable phase. Inset: number of photons $n = |\alpha|^2$ as a function of the pump strength F/γ obtained by solving Eq. (2.7) (continuous line). The two dashed lines represent the frontier of the bistable region. In this region, there are three solutions, however the one in the middle is not stable (see main text). For the inset, $\Delta = 1.5\gamma$.

Figure 2.1 shows the phase diagram obtained from the analysis of the mean-field equation. The region marked in blue corresponds to the bistable phase. The boundaries of the bistable region correspond to the extremal values of f. In this region, Eq. (2.7) admits three solutions. However, the solution in the middle (yellow curve in the inset of Fig. 2.1) is unstable ($f'(n) < 0$).

2.1.2 Analytical exact solution of the master equation

Even though the semiclassical analysis provides already a good description of the experimental observations, the transposition of this phenomenology into a purely quantum description raises many interesting questions. Indeed, a single quantum solution is expected in the steady state instead of the two found in the previous section. The exact solution was found by Drummond and Walls in their seminal work published in 1980 [96]. The solution was obtained using the complex P representation of the density matrix [108, 109]. The density matrix $\hat{\rho}$ can be mapped into a scalar function of two

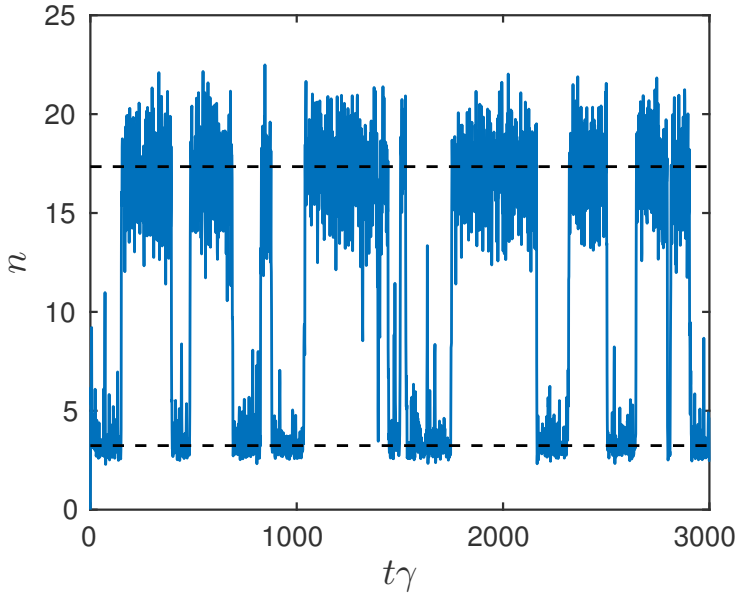

Figure 2.2: Number of photon n for a single quantum trajectory as a function of time (blue line). The corresponding stable mean-field solutions are the horizontal dashed lines. The quantum trajectory has been obtained with a Montecarlo wavefunction algorithm in the Fock basis [62, 63]. Parameters are $\Delta = 1.5\gamma$, $U = 0.1\gamma$, $F = 2.3\gamma$.

complex numbers $P(\alpha, \beta)$ via the relation:

$$\hat{\rho} = \int_{\mathcal{D}} P(\alpha, \beta) \frac{|\alpha\rangle\langle\beta^*|}{\langle\beta^*|\alpha\rangle} \mathrm{d}\mu, \tag{2.10}$$

where $\mathcal{D}$ is the integration domain in the complex plane, $\mathrm{d}\mu = \mathrm{d}^2\alpha\mathrm{d}^2\beta$ is the integration measure and $|\beta^*\rangle$ and $|\alpha\rangle$ are coherent states. This mapping transforms the Lindblad master equation into a Fokker-Planck equation which can be solved exactly for the Kerr model (the details of the derivation can be found in Ref. [96]). As a result, it is possible to compute exactly the various correlation functions $\langle(\hat{a}^\dagger)^i\hat{a}^j\rangle$ in the unique steady state, namely,

$$\langle(\hat{a}^\dagger)^i\hat{a}^j\rangle = \left(\frac{-2F}{U}\right)^i \left(\frac{2F^*}{U}\right)^j \frac{\Gamma(c)\Gamma(c^*)}{\Gamma(c+j)\Gamma(c^*+i)} \times \frac{\mathcal{F}(c+j, c^*+i, 8|F/U|^2)}{\mathcal{F}(c, c^*, 8|F/U|)}, \tag{2.11}$$

with $c = -2(\Delta + \mathrm{i}\gamma/2)/U$, $\Gamma(\bullet)$ being the gamma special function and $\mathcal{F}$ being the hyperbolic function

$$\mathcal{F}(c, d, z) = \sum_{n=0}^{\infty} \frac{\Gamma(c)\Gamma(d)}{\Gamma(c+n)\Gamma(d+n)} \frac{z^n}{n!}. \tag{2.12}$$

To understand the exact steady-state solution, it is insightful to inspect single quantum trajectories. Figure 2.2 shows the number of photons as a function of time for a single quantum trajectory. The trajectory was obtained using a Montecarlo wavefunction algorithm [62, 63] in the Fock number state basis. The black dashed lines represent the

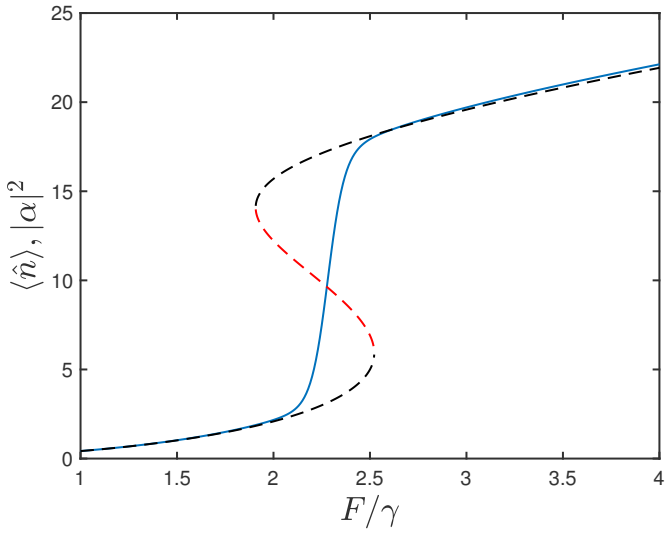

Figure 2.3: Number of photons as a function of the driving amplitude F/γ. The continuous line corresponds to exact quantum solution given in Eq. (2.11). The dashed line depicts the mean-field value of the number of photons $|\alpha|^2$. The branch plotted in red is the unstable solution. Parameters: $\Delta = 1.5\gamma$, $U = 0.1\gamma$.

two stable semi classical solutions for the following parameters: $\Delta = 1.5\gamma$, $U = 0.1\gamma$, $F = 2.3\gamma$. At random times the state of the cavity switches between the two mean-field solutions and the time spent in each branch is much longer than the photon lifetime γ^{-1}. When many trajectories are averaged, the resulting density matrix is a mixture of the two semiclassical solutions with relative weight given by the relative time spent in each branch.

Figure 2.3 shows the number of photons as a function of the pump intensity F. The dashed line shows the multivalued solution obtained by solving the mean-field equation. The black lines represent the two stable solutions whereas the red line represents the unstable one. The continuous line is the exact solution of the master equation. It is worth noting that the semiclassical solution shows small quantitative discrepancies with the quantum solution outside of the bistable region.

2.2 Time-dependent master equation

The results given so far are the steady-state results for a time-independent master equation. In order to understand how the experimental observations and the semiclassical analysis fit into the quantum description of bistability, we investigate the time-dependent solution of the master equation considering a time-dependent pump. In order to study dynamical hysteresis phenomena, we consider in particular a triangular modulation,

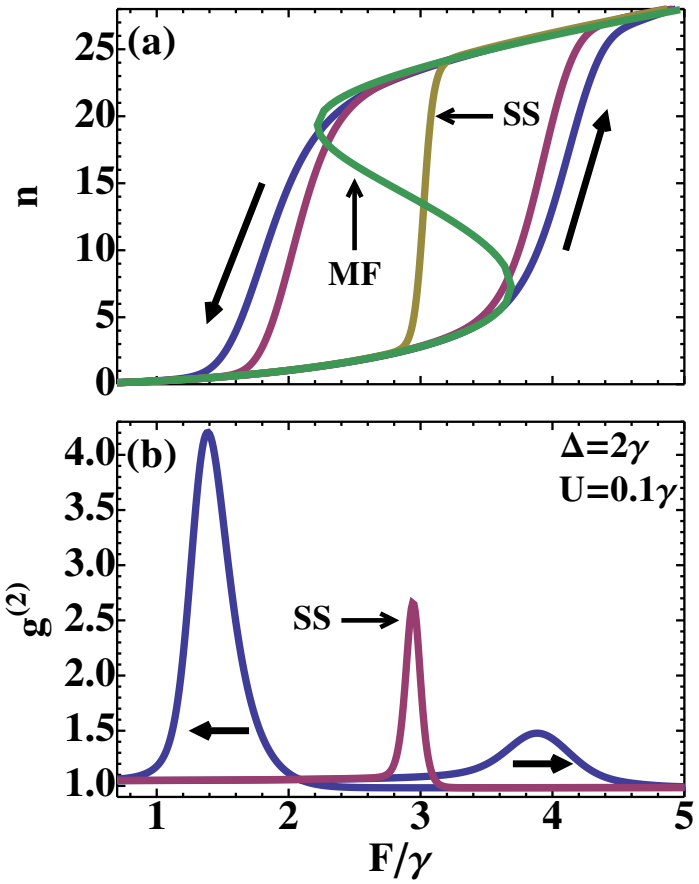

Figure 2.4: (a) The photon population n and (b) the $g^{(2)}$ second-order correlation function versus the driving amplitude F (units of γ) for a single-mode driven-dissipative quantum resonator with a nonlinearity $U = 0.1\gamma$ and detuning $\Delta = 2\gamma$. In panel (a), the steady-state mean-field (MF) result and the quantum steady-state solution (SS) from Ref. [96] are presented. The other two curves are dynamic hysteresis cycles predicted by the time-dependent quantum master equation obtained by using two different sweep times t_s ($t_s/\Delta F = 10/\gamma^2$ for the curve with the largest hysteresis cycle and $t_s/\Delta F = 20/\gamma^2$ for the smaller one). In panel (b) the steady-state solution is shown together with the result for a time-dependent sweep with $t_s/\Delta F = 10/\gamma^2$ (the arrows indicate the direction of the sweep).

consisting of one linear sweep from F_0 to $F_0 + \Delta F$ and one from $F_0 + \Delta F$ back to F_0:

$$F(t) = F_0 + \frac{t}{t_s}\Delta F\theta(t_s - t) - \frac{t - 2t_s}{t_s}\Delta F\theta(t - t_s) \tag{2.13}$$

where t_s is the sweep duration and $\theta(\tau)$ is the Heavyside step function.

In order to solve numerically the master equation (2.3), we have expressed the time-dependent density matrix in the basis of Fock number states $|n\rangle$. Convergence of the results have been carefully checked by increasing the cutoff number of photons. Using this numerical method, we can explore regimes with a number of photons of up to a few tens. Figure 2.4 compares the steady-state results obtained from Eqs. (2.7) and (2.11) (noted respectively MF and SS) with the results obtained by numerical integration of the master equation (2.3) with a time-dependent drive amplitude (2.13). The top panel of Fig. 2.4 reports the number of photons as a function of the drive amplitude. The yellow and green curves represent the steady-state values respectively for the mean-field and the exact solutions. The mean-field solution exhibits the characteristic "S" shape due to the existence of three solutions of Eq.(2.7). The two other curves of this panel are the numerical results of the time-dependent master equation (2.3), showing that when the triangular modulation is applied a dynamical hysteresis appears. The largest hysteresis loop is the result of a faster pump modulation ($t_s/\Delta F = 10/\gamma^2$) while the smaller one is obtained with a slower pump sweep ($t_s/\Delta F = 20/\gamma^2$). This implies that the area of the hysteresis loop decreases for increasing t_s. In the adiabatic limit of an infinitely slow sweep ($t_s \to +\infty$) the hysteresis disappears and the exact unique solution is recovered. It is also interesting to study the equal-time second order correlation function $g^{(2)}$:

$$g^{(2)} = \frac{\langle \hat{a}^\dagger \hat{a}^\dagger \hat{a}\hat{a}\rangle}{\langle \hat{a}^\dagger \hat{a}\rangle^2}. \tag{2.14}$$

In Fig. 2.4(b) the $g^{(2)}$ function is plotted as a function of the pump amplitude both for the steady state and the modulated case. In the steady state, an important peak occurs at the transition, with $g^{(2)}$ being significantly larger than one. This feature cannot be recovered from the mean-field equation for which $g^{(2)} = 1$. For a time-dependent sweep of the pump, two peaks are observed when the number of photons goes from one branch to the other. The peak is more (less) pronounced for decreasing (increasing) F.

2.2.1 Area of the dynamical hysteresis

As it is visible in the top panel of figure 2.4, when the sweep is slower, the size of the hysteresis loop is reduced. In order to be able to quantify such behaviour of the dynamical hysteresis, we introduce the hysteresis area A:

$$A = \int_{F_0}^{F_0+\Delta F} \mathrm{d}F|n_\downarrow - n_\uparrow|, \tag{2.15}$$

with $n_\uparrow(t)$ being the photon population when the pump is increased and $n_\downarrow(t)$ being the photon population when the pump is decreased.

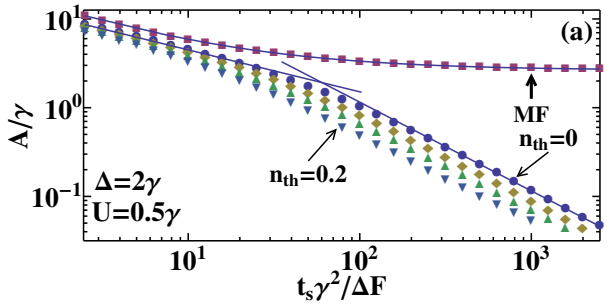

Figure 2.5: The area A of the hysteresis loop as a function of the sweep time t_s (units of $\Delta F/\gamma^2$) for different temperatures (from bottom to top the thermal population n_{th} is 0.2, 0.1, 0.05, and 0, corresponding respectively to $\beta\omega_c \simeq 1.8$, 2.4, 3, and $+\infty$), together with the result from the mean-field (MF) approximation for $U = \gamma/2$ and $\Delta = 2\gamma$. The solid lines are power-law fits to the different limiting regimes for which two separate power laws are observed. For large t_s we find the behavior $A \propto t_s^{-1}$ while for small values of t_s we find $A \propto t_s^{-b}$ with a coefficient b that depends on the system parameters. For the mean-field result we find an overall good agreement with $(A - A_0) \propto t_s^{-2/3}$ with $A_0 > 0$ the static hysteresis area.

Figure 2.5 shows the values of A as a function of the speed of the modulation $t_s\gamma^2/\Delta F$ for different number of thermal photons. The hysteresis area of the time-dependent mean-field theory result is also shown (noted MF). Our results show that for a relatively fast sweep (small $t_s/\Delta F$ limit), the hysteresis areas obtained with the exact and the mean-field theory follow a similar behaviour. However, for slower sweeps, a significant difference appears: while the time-dependent mean-field result converges to a finite area $A_0 > 0$, the quantum solution tends to 0. Note that the static area A_0 is the area between the two stable branches obtained with the mean-field theory. In the quantum case, the hysteresis area as a function of the sweep duration follows two distinct power-laws in the slow and fast sweep limits. Moreover, the double power-law behaviour survives in the presence of moderate thermal fluctuations. Notice that a slight decrease of the area is observed with respect to the zero-temperature solution. This is expected because the thermal fluctuations contribute to the switching between the two branches. In the slow sweep limit, the power-law behaviour allows us to determine a characteristic timescale τ from the fit:

$$A = \left(\frac{t_s}{\tau\Delta F}\right)^{-1}. \tag{2.16}$$

When the sweep timescale is similar to τ ($t_s\gamma/\Delta F \sim \tau$), the quantum fluctuations start to play a significant role and induce a deviation from the mean-field behaviour.

Figure 2.6 shows the dependence of the characteristic time τ (from Eq. 2.16) as a function of the nonlinearity U (top panel) and the detuning Δ (bottom panel). It is worth noting that the characteristic time can be several orders of magnitude larger than the lifetime $1/\gamma$ inside of the cavity for large detuning and/or small nonlinearity. The top

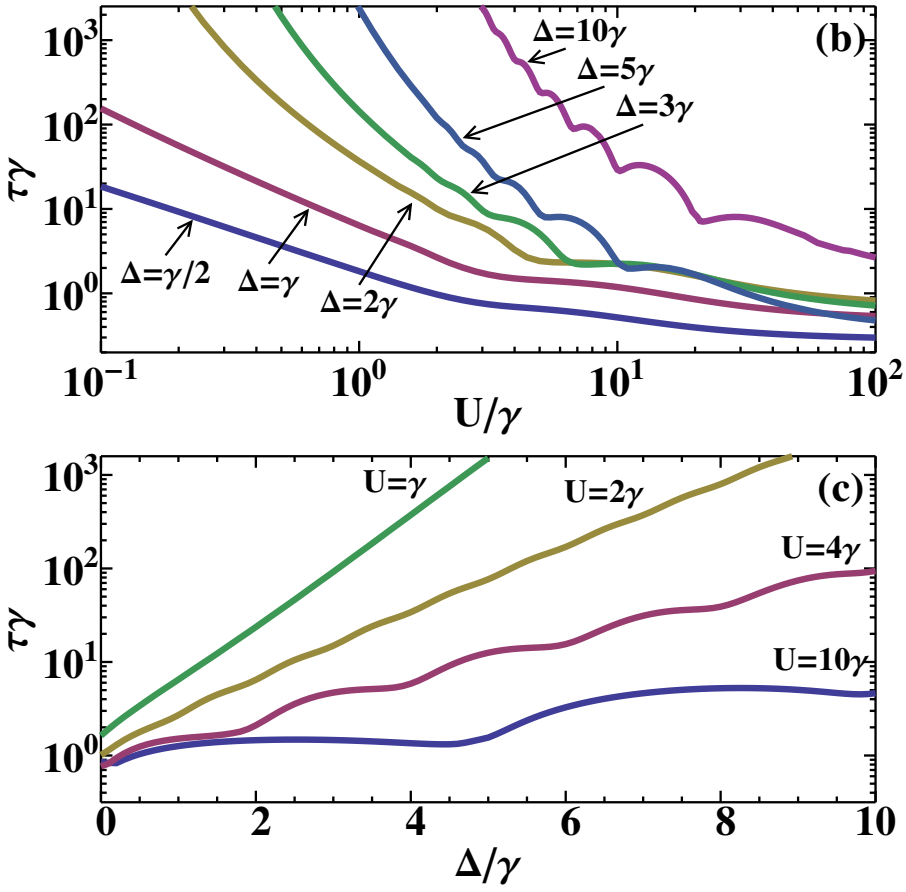

Figure 2.6: The characteristic time scale τ, as determined from the behaviour $A = (t_s/(\tau\Delta F))^{-1}$ for large t_s, is shown (top panel) as a function of the nonlinearity U (units of γ) for different values of the detuning Δ and (bottom panel) as a function of the detuning Δ (units of γ) for different values of the nonlinearity U. Note the oscillating behaviour with minima satisfying the n-photon resonance conditions: $Un(n-1)/2 = n\Delta$.

panel shows that in the limit $U \to \infty$, the hysteresis survives and its characteristic time converges to a finite value. As a function of the detuning, an overall exponential increase of the characteristic hysteresis time is observed. The bottom panel indicates that the dynamical hysteresis survives for $\Delta < \sqrt{3}\gamma/2$ where the semiclassical prediction shows no static hysteresis. In both panels, modulations in the behaviour of τ appear due to photon quantization. The minima correspond to the resonance condition $\Delta n = U/2(n-1)n$ with n a positive integer. These are obtained when the energy of n pump photons is equal to the energy of n interacting photons in the resonator [110].

2.2.2 Analytical scaling behaviour in connection with the Kibble-Zurek mechanism

In the previous section, we presented a comprehensive set of numerical results showing the rich properties of the dynamical hysteresis of a Kerr nonlinear optical resonator with a time-dependent pump. This section gives a semi-analytical derivation of the double power-law behaviour. We find that the dynamical hysteresis is due to the non-adiabatic response of the system when the pump is modulated around a critical point.

When changing in time one parameter of an Hamiltonian system, by definition the response becomes non-adiabatic when the time scale of the change is much shorter than the time scale of the system internal dynamics. Such a time is proportional to the inverse of the energy gap between the ground state and the excited state manifold. In the case of quantum phase transitions, the energy gap vanishes at a critical point (softening of the excitation mode) leading to a divergence of the corresponding internal dynamics time scale (critical slowing down). Therefore, when crossing a critical point, there is always a non-adiabatic response region around the transition. This property is at the heart of the Kibble-Zurek mechanism for the formation of topological defects in quenched quantum phase transitions [111, 112, 113] (see for example Ref. [114] for a review).

As seen in Chapter 1, in driven-dissipative systems, the Hamiltonian gap is no longer the quantity characterizing the adiabaticity of the change. The relevant quantity is the spectrum of the Liouvillian super-operator. The eigenvalue equation for the Liouvillian reads:

$$\mathcal{L}\hat{\rho}_\lambda = \lambda\hat{\rho}_\lambda, \tag{2.17}$$

where λ is a complex eigenvalue of $\mathcal{L} = -\mathrm{i}[\hat{H}, \bullet] + \gamma/2(2\hat{a} \bullet \hat{a}^\dagger + \hat{a}^\dagger\hat{a} \bullet + \bullet \hat{a}^\dagger\hat{a})$ and $\hat{\rho}_\lambda$ is the corresponding eigen-density operator. The eigenvalues λ are complex with negative real parts ($\mathrm{Re}(\lambda) \leq 0$) to ensure the evolution toward a steady state corresponding to the eigenvalue $\lambda = 0$. The real and imaginary parts of the eigenvalues λ correspond respectively to the damping rate and the frequency of the excitations. Here, we focus on the Liouvillian gap, given by the eigenvalue with the smallest non-zero real part (in absolute value). Figure 2.7 shows the real and imaginary parts of the first non-zeros eigenvalues of the Liouvillan as a function of the drive amplitude for $\Delta = 2\gamma$ and $U = 0.1\gamma$. Around the transition point $F \approx 3\gamma$, the imaginary part of the first non-zeros

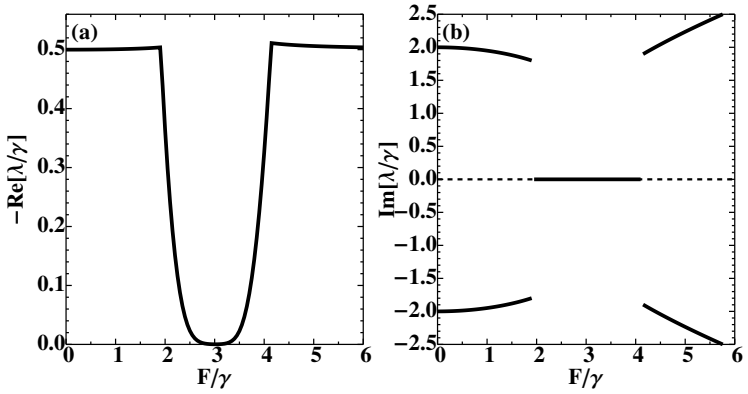

Figure 2.7: The real (a) and the imaginary (b) part of the Liouvilian eigenvalue λ (in units of γ), corresponding, respectively, to the damping rate and the frequency of the excitation mode. In particular, we consider the least damped mode (different from the steady state corresponding to $\lambda = 0$) as a function of the drive amplitude F (in units of γ) for $U = 0.1\gamma$ and $\Delta = 2\gamma$. Around the transition point (at $F_c \approx 3\gamma$) the damping rate (real part) is strongly suppressed, while the imaginary part is exactly zero, indicating the presence of a soft diffusive mode. Away from the transition region there are two symmetric least damped modes with equal damping rates but opposite frequencies (the imaginary parts).

eigenvalues goes strictly to zero (right panel) and the real part is strongly suppressed (left panel). As a result, the excitation mode around the transition is degenerate with the steady state in frequency, i. e. it is a soft mode, while it has a small but finite damping, i.e. it has a diffusive behaviour. As a result of this energy degeneracy, it is expected that the response of the system to a sweep will have a non-adiabatic contribution. From this diffusive soft mode, we can define the relaxation time $\tau_R = 1/|\mathrm{Re}(\lambda)|$. It is important to note that the so called tunneling time τ_T correspond to the value of the relaxation time when $|\mathrm{Re}(\lambda)|$ is minimal. This tunneling time sets the scale for the switching between one semiclassical state to the other induced by quantum fluctuations at the transition [98, 99, 56].

In order to be able to evaluate the non-adiabatic region leading to the hysteresis loop quantitatively, we define the distance to the value of the pump at the transition F_c:

$$\epsilon(t) = F_c - F(t). \tag{2.18}$$

We consider a linear sweep between $F_c - \Delta F/2$ to $F_c + \Delta F/2$ with a total duration t_s. Following Ref. [113], we define the normalized sweep rate:

$$\left|\frac{\dot{\epsilon}(t)}{\epsilon(t)}\right| = \frac{\Delta F}{t_s}\frac{1}{|F_c - F(t)|} = \frac{1}{\tau_s}. \tag{2.19}$$

This equation defines the sweep timescale τ_s which is plotted on the top panel of Fig. 2.8 for two different values of the sweep duration ($t_s\gamma^2/\Delta F = 10^2$ and 10^4). Note

that this timescale is different from the sweep duration t_s as it also takes the change of amplitude into account. On the top panel of Fig. 2.8 we also plot the relaxation timescale $\tau_R = 1/\mathrm{Re}(\lambda)$. As mentioned above, it is possible, at equilibrium, to use the Kibble-Zurek approach to estimate the region around the critical point when the system response is not adiabatic by comparing the sweep rate with the gap of the Hamiltonian [114]. We generalize this criterion to open quantum systems by comparing the sweep timescale τ_S to the relaxation time τ_R defined from the spectrum of the Liouvillian: when $\tau_s > \tau_R$ we expect that the system enters the nonadiabatic regime. The hysteresis loop we observed in the previous section is a result of the nonadabatic response of the system: the system freezes in the nonadiabatic region and jumps to the other solution at the end of it. The dotted lines on the top panel of Fig. 2.8 represent the boundaries of the nonadiabatic region for $t_s\gamma^2/\Delta F = 10^2$.

In the slow sweep time limit, $t_s \to 0$, the width of the non-adiabatic region vanishes $\delta F \to 0$. In this limit, the relaxation time τ_R gets close to its maximum value τ_T (the so-called tunneling time [98]).The change in the pump becomes non-adiabatic when $\tau_s < \tau_r \simeq \tau_T$, The boundaries of the non adiabatic region can be evaluated by imposing $\tau_s = \tau_T$ in Eq. (2.19), giving the expected -1 exponent:

$$\delta F = 2\tau_T \left(\frac{t_s}{\Delta F}\right)^{-1}. \tag{2.20}$$

The panel (b) of Fig.2.8 shows the width of the non-adiabatic region δF presented as a function of the sweep time duration t_s, showing the double power-law behaviour also found for the area of the dynamic hysteresis. Furthermore, in the slow sweep limit, the -1 exponent ($\delta F \propto t_s^{-1}$) is recovered. The hysteretic behaviour of the number of photons is caused by nonadiabaticity as the system does not have time to relax to the steady state. Hence, the area of the hysteresis loop is linked to the width δF of the nonadiabatic region as confirmed by our numerical results. In panel (c) the tunneling time τ_T is compared with the characteristic time τ (see previous section) as a function of the detuning Δ for two values of the nonlinearity. This reveals qualitatively similar behavior with an overall exponential increase as a function of the detuning and oscillations due to the multiphotonic resonances.

For conservative systems with a finite energy gap the Kibble-Zurek mechanism breaks down for slow sweeps since the evolution becomes adiabatic [115, 116]. In this case an effective description is provided by the Landau-Zener approximation for the evolution of a system through an avoided energy crossing [117, 118]. Applying the Kibble-Zurek approach results in a good agreement with the Landau-Zener result only for sufficiently fast sweeps [115, 116]. Note that the Landau-Zener formula for a dissipative excited state does not depend on the decay rate [119] and its applicability is connected to the existence of a finite gap for the frequency.

For the considered dissipative system on the other hand we find that the scaling laws based on a Kibble-Zurek-like approach for the non-adiabatic regime agree with the numerical results for the hysteresis area, also in the slow sweep limit. This shows that

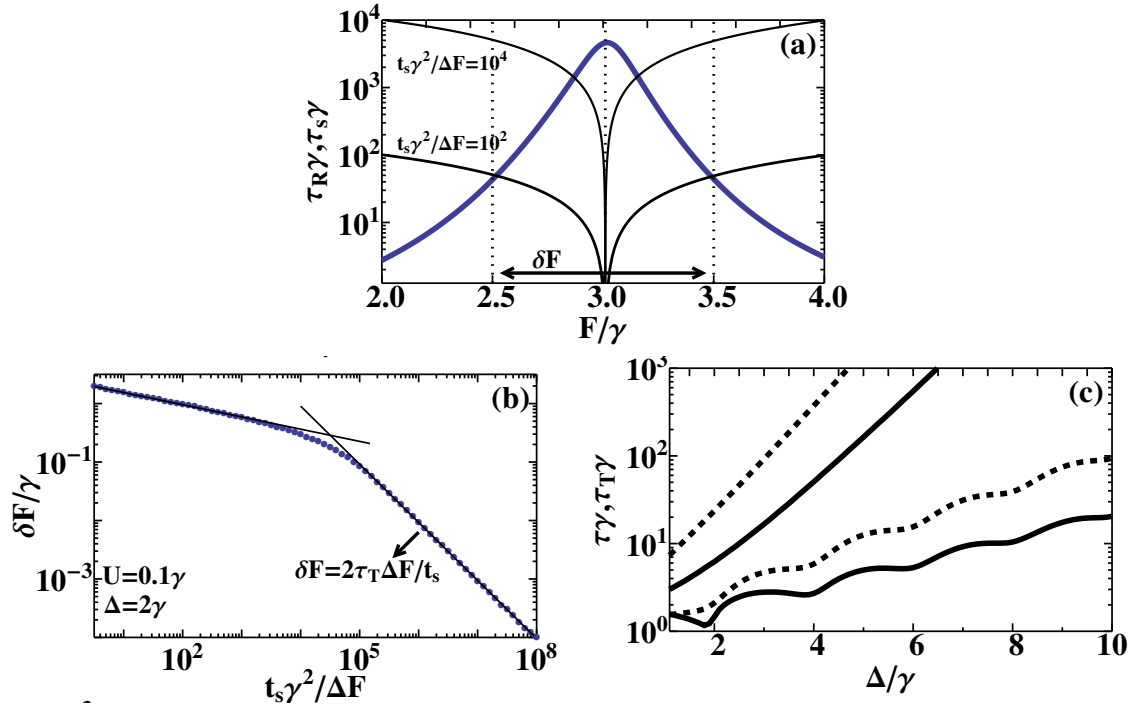

Figure 2.8: (a) The relaxation time τ_R as a function of the pumping strength F/γ (the blue curve that is peaked close to $F_c \approx 3$). The two other curves represents the sweep timescale τ_s. The width of the non-adiabatic region δF is marked by the two dashed vertical lines around F_c for the fastest sweep. (b) The width of the non-adiabatic region δF as a function of the speed of the pump sweep. The two straight lines are the two power laws. The one for slow sweep is obtained with the analytical formula (2.20). For (a) and (b), $\Delta = 2\gamma$ and $U = .1\gamma$ (c) The tunneling time τ_T (continuous line) and the characteristic time τ (dashed line)as a function of the cavity-pump detuning Δ for $U/\gamma = 1$ (upper curves) and $U/\gamma = 4$ (lower curves).

an adiabatic regime is never reached, no matter how slow the sweep. At first sight this might seem in conflict with the results for the Kibble-Zurek mechanism for conservative systems since the real part of the Liouvillian gap remains finite. However, for dissipative systems it is the imaginary part of the Liouvillian eigenvalue that gives the analogous of the excitation energy.

2.2.3 Truncated Wigner Approximation

So far the numerical results have been obtained by integrating the exact master equation Eq. (2.3) or by diagonalizing the Liouvillian. However, in the case of smaller non-linearities, convergence with respect to the photon cutoff might be impossible to reach.

In order to be able to deal with non-linearities much smaller than γ, we use the stochastic method hased on the so-called truncated Wigner approximation. Mapping the density matrix into the Wigner function W [56], the master equation is transformed into the equation:

$$\begin{aligned}\partial_t W = &\partial_\alpha \left[\mathrm{i}\Delta\alpha - \mathrm{i}U(|\alpha|^2-1)\alpha + \frac{\gamma}{2}\alpha + \mathrm{i}F\right] W \\ &+ \partial_{\alpha^*}\left[-\mathrm{i}\Delta\alpha^* + \mathrm{i}U(|\alpha|^2-1)\alpha^* + \frac{\gamma}{2}\alpha^* - \mathrm{i}F\right] W \\ &+ \frac{\gamma}{2}(\partial_\alpha\partial_{\alpha^*}W + \partial_{\alpha^*}\partial_\alpha W) \\ &+ \mathrm{i}\frac{U}{4}\partial_\alpha\partial_{\alpha^*}\left(\partial_{\alpha^*}\alpha^* W - \partial_\alpha \alpha W\right). \end{aligned} \tag{2.21}$$

The general solution of such an equation is unknown. However in the limit of small nonlinearity U, the third-order derivative term can be neglected and a Fokker-Planck equation for a well defined probability distribution is recovered [82]. This equation can be solved using a Langevin approach based on a stochastic equation for the complex field $\alpha(t)$:

$$\partial_t\alpha = -\left(\mathrm{i}\Delta + \frac{\gamma}{2}\right)\alpha + \mathrm{i}U(|\alpha|^2-1)\alpha - \mathrm{i}F + \xi(t). \tag{2.22}$$

The stochastic term $\xi(t)$ is a complex random Gaussian noise following the statistics:

$$\overline{\xi(t)} = 0, \tag{2.23}$$

$$\overline{\xi(t)\xi^*(t')} = \frac{\gamma}{2}\delta(t-t'), \tag{2.24}$$

where $\delta(\tau)$ is the Dirac distribution and $\overline{\bullet}$ is the statistical average. Within the Wigner representation, averages of *symmetrised* observables are obtained from averages over different stochastic realisations of the field $\alpha(t)$: $\langle\{\hat{a}^{\dagger i}, \hat{a}^j\}_S\rangle = \overline{\alpha^{*i}\alpha^j}$. For example, the number of photon $\langle\hat{n}\rangle$ is computed in the following way:

$$\overline{|\alpha|^2} = \langle\{\hat{a}^\dagger, \hat{a}\}_S\rangle = \frac{1}{2}\langle\hat{a}^\dagger\hat{a} + \hat{a}\hat{a}^\dagger\rangle = \langle\hat{n}\rangle + \frac{1}{2}.$$

A time-dependent driving amplitude can also be included in the truncated Wigner function approach. Figure 2.9 shows the number of photons as a function of the pump

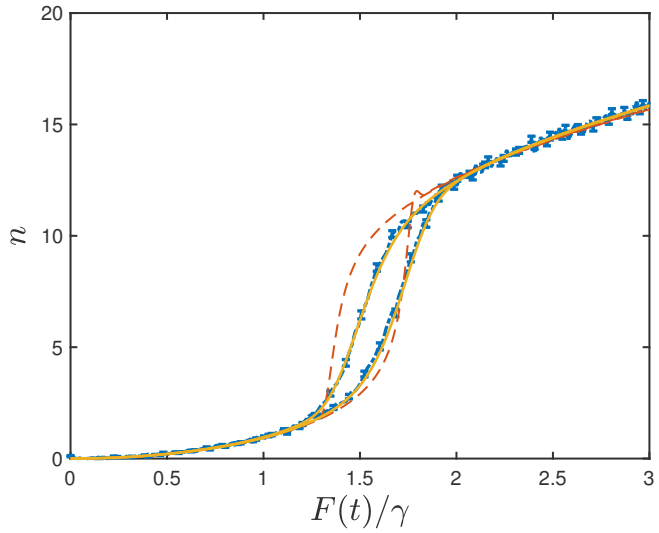

Figure 2.9: Number of photons n as a function of the driving amplitude $F(t)$. The number of photons is obtained with the dynamical mean-field theory (dashed line), the time-dependent master equation (continuous line) and the truncated Wigner approximation (dotted dashed line with error bars). Parameters: $\Delta = \gamma$ and $U = 0.1\gamma$ and $t_s = 20\gamma^{-1}$, 500 stochastic trajectories.

strength obtained with the truncated Wigner approximation, together with the results given by the time-dependent mean-field equation and the exact master equation (2.3). Note that, the Gaussian noise term induces switching from one branch to the other.

Figure 2.10 compares the result of the truncated Wigner stochastic method to the exact one for the area A of the hysteresis loop for different durations of the pump sweep. The continuous straight line is the result of a power-law fit for the area computed from the integration of the Langevin equation (2.22) in the slow sweep limit. Since the detuning and the nonlinearity are small, both curves super-impose. The power-law fit of the hysteresis area as a function of the speed of the sweep is in very good agreement with expected behaviour.

2.3 Experimental observation in semiconductor micropillars

The previous predictions where observed experimentally by the team of Jacqueline Bloch and Alberto Amo at the C2N laboratory in Marcoussis [106]. In this implementation, the nonlinear cavity is a semiconductor micropillar: a single-mode cavity is obtained by etching an heterostructure composed of two Bragg mirrors with quantum wells embedded in between. The properties of the sample will not be discussed here but can be found in Ref. [106]. The sample is maintained at 4K and driven by a frequency-tunable single-

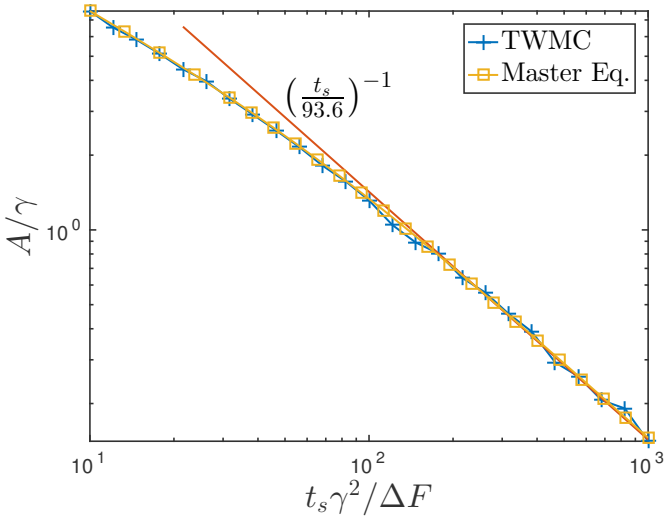

Figure 2.10: The area A/γ as a function the speed of the sweep $t_s\gamma^2/\Delta F$ computed with the master equation (2.3) (line with $\square$ symbols) and with the truncated Wigner approximation (line with the + symbols) for $U = 0.1\gamma$ and $\Delta = \gamma$. The continuous line is a power law fit of the hysteresis area in the long t_s limit. For the truncated Wigner method, each point was obtained by averaging over 1000 trajectories. The longest simulation ($t_s\gamma^2/\Delta F = 10^3$) took approximately 7 hours.

mode laser. The laser power is modulated by an electro-optic modulator (EOM on Fig. 2.11). The waveform sent to the modulator contains a series of $\sim$ 50 triangular ramps with different durations. The transmission through the cavity is measured with a photodiode connected to an oscilloscope. The scanning times t_s span the 0.8−50kHz range. The different trajectories are averaged in order to obtain the mean value of the transmitted intensity. Note that the transmitted intensity measured by the photodiode is proportional to the number of photons inside the cavity.

Panels (b) and (c) of Fig. 2.11 compare the transmitted intensity for one trajectory with the averaged hysteresis loop for two different speeds for a detuning $\Delta/\gamma = 1.09$. As a result of a slower sweep, panel (c) shows more switchings from one branch to the other with respect to panel (b). Consequently, the hysteresis area is reduced in panel (c) with respect to panel (b). Panel (d) shows measurements of the dynamical hysteresis for $\Delta = 1.01\gamma$ at different speeds (faster sweeps are in the bottom). In the case of a slow sweep, the measured hysteresis strongly deviates from the mean-field solution (dashed line). Panel (e) shows the dependence on the detuning ($\Delta = 1.35\gamma$) of the hysteresis for the same sweep speeds. This dependence on Δ is conform to the behaviour showed in figure 2.6.

Here, we consider a different definition of the hysteresis area

$$A = \int_{P_0}^{P_0+\Delta P} \mathrm{d}P |n_\downarrow(P) - n_\uparrow(P)|, \tag{2.25}$$

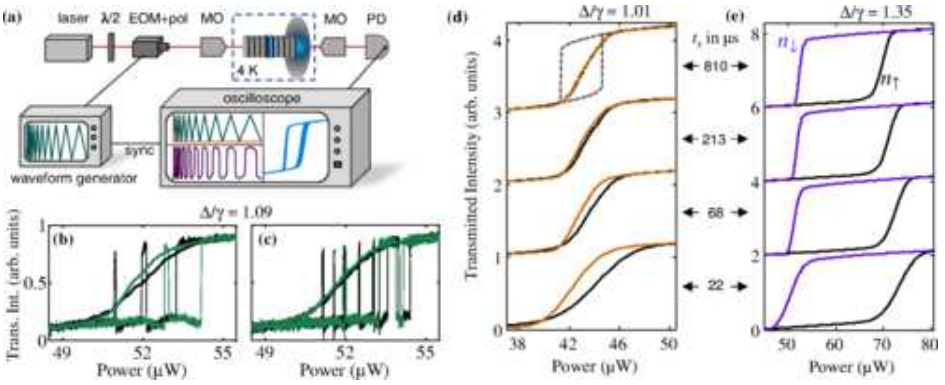

Figure 2.11: (a) Experimental setup for the dynamical optical hysteresis experiments: $\lambda/2$, MO, PD, and EOM+pol, stand for half-wave plate, microscope objective, photodiode, and electro-optic modulator with a polarizer, respectively. The green (purple) traces in the waveform generator and in the oscilloscope are measurements of the incident (transmitted) signals. The hysteresis cycles in the oscilloscope are obtained by plotting the transmitted versus the incident signal, overlaid for various scanning times. The colored and black lines in (b)-(e) represent the transmission when the power is ramped down and up, respectively. (b) and (c) show single shot (thin lines) and averages over 1000 realizations (thick lines) of dynamic hysteresis. The scanning time is $t_s = 0.11$ ms in (b), and $t_s = 0.43$ ms in (c). (d) and (e) show dynamic hysteresis averaged over 1500 realizations. The dashed line in (d) is the mean-field calculation corresponding to the experiment.

with $n_\uparrow(P)$ (resp. $n_\downarrow(P)$) being the transmitted number of photons averaged over many realization of the experiments when the power P is increased (resp. decreased). The different definition with respect to Eq. (2.15) is due to the fact that the triangular modulation concerns the driving power $P = |F|^2$ instead of the amplitude F. As seen in Fig. 2.11, the hysteretic behaviour remains similar to what was found in the previous section.

The hysteresis area, obtained experimentally, is plotted as a function of the speed of the modulation on the left panel of Fig. 2.12. The different curves correspond to different values of the detuning. As expected, the double power law and the $A \propto (t_s)^{-1}$ (in the long sweep limit) are visible for small enough detuning. This is in good agreement with the theoretical result of the panel (b) of Fig. 2.12 that represents the width of the non-adiabatic region as a function of the duration of the power sweep. The width of the non-adiabatic δI was obtained following the reasoning of section 2.2.2 (as shown in the inset).

By changing the spatial size of the micropillars it is possible to modify the Kerr nonlinearity U. In particular, the larger the size the smaller the value of U. Figure 2.13 shows the area of the hysteresis loop as a function of t_s for three cavities of different nonlinearities U/γ at a fixed detuning $\Delta = 1.15\gamma$ (top and bottom curves) and $\Delta = 1.13\gamma$

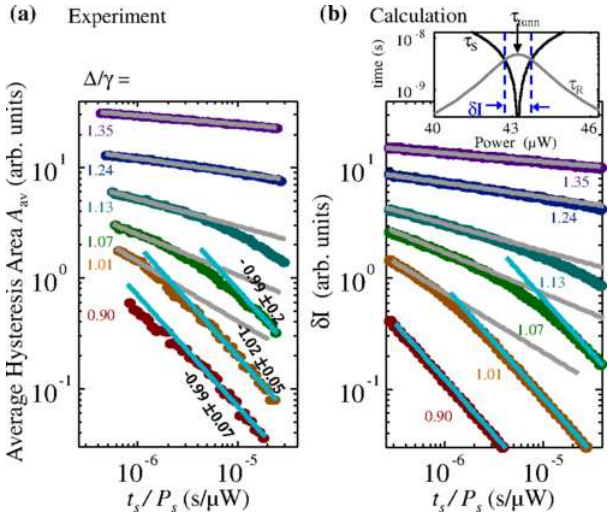

Figure 2.12: (a) Measured hysteresis area $A_{\rm av}$ (defined in Eq. 2.25) as a function of t_s/P_s, where P_s is the scanned power range. Different colors correspond to different values of Δ/γ. The gray lines are power law fits with an exponent greater than -1. The blue lines indicate power laws in the regime influenced by quantum fluctuations. The experimentally retrieved exponents in this regime are shown with 2σ confidence intervals on the fits. (b) Calculations of the non-adiabatic range δI of the driving intensity using the scaling analysis described in the text. The power laws in (b) all have the same exponents retrieved from the fits in (a). The inset in (b) shows the system reaction time τ_R in gray, and the sweep time scale τ_S in black, for $U = 0.0075\ \gamma$ and $\Delta = 1.01\ \gamma$. The dashed blue lines indicate the non-adiabatic range δI. The conversion of the theoretical intensity units to the experimental power units is described in the Supplemental Material of [106].

(middle curve). The double power-law behaviour is still visible for cavity 1 and the inflection in the curve corresponding to cavity 2 suggests it in this case whereas a single power-law is visible for cavity 3. Furthermore, the size of the nonlinearity is larger for cavity 1 than cavity 2 and the least nonlinear cavity is cavity 3. Hence the observation of the increase of the time of the sweep to observe the -1 exponent is in agreement with the results of the previous section (see Fig. 2.6). The right panel of Fig. 2.13 shows the non-adiabatic region as a function of the duration of the sweep of the pump computed using the results from 2.2.2. The nonlinearities are fitted and are consistent with independent estimates. Note that as the nonlinearity is decreased, the number of photons inside the cavity increases and the double power-law becomes a single power-law. This is the signature of a thermodynamic limit for the photon population $n \to \infty$ in a single cavity [120].

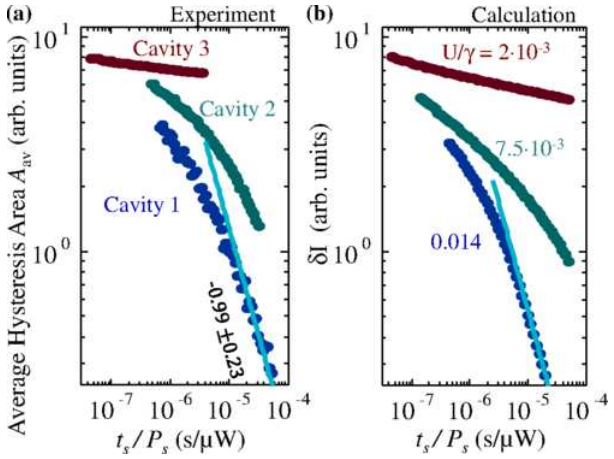

Figure 2.13: (a) Measurements of the hysteresis area A for three cavities with different U/γ and approximately equal Δ/γ. U/γ decreases from cavity 1 to cavity 3. (b) Calculations of δI as explained in the text and in Fig. 2.12. For the highest and lowest curves $\Delta/\gamma = 1.15 \pm 0.1$, while for middle curve $\Delta/\gamma = 1.13 \pm 0.1$, both in experiments and calculations. In (a), the curve corresponding to cavity 3 was divided by 80. In (b), the curve corresponding to the smallest U/γ was divided by 4, and the curve corresponding to the largest U/γ was multiplied by 2. These multiplications (for improving visibility) only shift the curves vertically and do not change the exponent.

2.4 Conclusion

In this chapter, we have investigated the time-dependent exact solutions of the quantum master equation for driven-dissipative nonlinear quantum resonators described by the Kerr model, thus including the role of quantum fluctuations and correlations. In particular, we have focussed on the regime where the semiclassical mean-field approximation predicts bistability and investigated temporal sweeps of the drive amplitude revealing dynamic hysteresis loops. The time-dependent quantum solution, in contrast to predictions of mean-field approaches, shows that the hysteresis area as a function of the total sweep time tends to 0 following a double power-law decay. These results have been shown to be robust with respect to thermal excitations for typical experimental temperatures. We have determined a characteristic time associated to the power-law decay of the dynamic hysteresis area, showing a rich behavior as a function of the nonlinearity and of the frequency detuning. Importantly, we have demonstrated that the dynamic hysteresis is associated to a non-adiabatic response region with connections to the Kibble-Zurek mechanism for quenched phase transitions. We have been able to describe analytically the power-law behaviour with scaling arguments and shown the role of a soft diffusive mode, i.e. having zero excitation energy, but a finite damping. The results were confirmed using a truncated Wigner appproximation. Our theoretical predictions were experimentally demonstrated in Kerr systems based on semiconductor micropillars.

The concepts presented here about dynamical hysteresis are not limited to single-mode systems, but can be exported to lattice systems exhibiting a dissipative phase transition. For example, driven-dissipative lattices of Kerr cavities (described by the Bose-Hubbard model) are promising in this respect [59].

Chapter 3

Corner-space renormalization method for open quantum lattice systems

This chapter is devoted to the presentation of the corner-space renormalization method, a novel numerical method used in most of the calculations discussed in the rest of this thesis. The corner-space renormalization method has been successfully applied on complex lattices exhibiting long range correlations and geometrical frustration [121], non-equilibrium anisotropic spin-1/2 Heisenberg XYZ model [122] and Bose-Hubbard model with coherent [123, 124] as well as incoherent [125] driving schemes and two-photon pumping [126].

The main challenge encountered while simulating large quantum lattice systems is the complexity growing exponentially with their size. Indeed, the dimension of the Hilbert space for a multipartite system constituted of m subsystems, each of them described in a Hilbert space of dimension N, is N^m. Furthermore, the complete description of open quantum systems requires the knowledge of the density matrix, hence the number of variables scales as the square of the Hilbert space dimension. In the case of one-dimensional systems, Matrix Product Operator approaches have proven to be powerful [15, 14]. Recent variational approaches could be a major step forward for the simulation of one-dimensional dissipative arrays [43, 44]. In the case of two-dimensional dissipative lattices, a recent proposal based on projected entanglement pairs [45] is another example of the on going effort to address this type of problems.

In the first section, a general description of the corner-space renormalization method is given with a particular focus on the most technical parts. In section 3.2, the method is benchmarked to the driven-dissipative Bose-Hubbard model with coherent pumping. In section 3.3, the main limitations of the method linked to the entropy of the system density matrix are discussed.

This project directed by Cristiano Ciuti was initiated by Alexandre Le Boité and Alexandre Baksic with the latter addition of Stefano Finazzi and myself. The method was published in *Physical Review Letters* [123].

3.1 Description of the algorithm

The problem we want to solve is defined by the Lindblad master equation for the density matrix $\hat{\rho}$ of a driven-dissipative quantum lattice system:

$$\partial_t \hat{\rho} = -\mathrm{i}\left[\hat{H}, \hat{\rho}\right] + \sum_j \left[\hat{c}_j \hat{\rho} \hat{c}_j^\dagger - \frac{1}{2}(\hat{c}_j^\dagger \hat{c}_j \hat{\rho} + \hat{\rho} \hat{c}_j^\dagger \hat{c}_j)\right], \tag{3.1}$$

where $\hat{H}$ is the Hamiltonian of the system and $\hat{c}_j$ are jump operators. For simplicity, we will consider a zero-temperature reservoir. In the case of optical cavities, the jump operators $\hat{c}_j$ will take the form $\hat{c}_j = \sqrt{\gamma_j}\hat{b}_j$ where $\hat{b}_j$ is the photon annihilation operator and γ_j is the dissipation rate on the jth site of the lattice.

The method we propose is based on the selection of a subspace of the Hilbert space, (that we call the "corner space") using the eigenvectors of the steady-state density matrix of smaller lattices. At each step, two lattices are merged and the M pairs of states maximizing their joint probabilities are selected to construct the basis of the corner space. The accuracy of the method can be controlled by enlarging the dimension of the corner space until convergence is reached.

More precisely, the algorithm can be decomposed into the following steps represented in Fig. 3.1:

1. Determine the steady-state density matrix for two small lattices for which we can solve the Lindblad Master equation (3.1) by brute-force integration.

2. Merge spatially two lattices for which the steady state is known and select the M most probable product states to construct the basis of the corner space.

3. Determine the steady-state solution in the corner-space.

4. Increase the dimension M of the corner space until convergence in the observables is achieved.

5. Repeat from the second step in order to create a larger lattice.

Note that in order to solve the master equation (3.1) in steps 1 and 3, any method can be used. In our calculations, if the dimension of the corner space (or the Hilbert space) is small enough ($M \lesssim 800$) the master equation is integrated using a Runge-Kutta algorithm, otherwise a Montecarlo wavefunction method is used [62, 63].

In the following, we will discuss in detail the two fundamental steps of the algorithm, i. e., the construction of the corner space (step 2) and the check for the convergence (step 4).

3.1.1 Construction of the corner space

Let us assume that we know the steady-state density matrices $\hat{\rho}_A$ and $\hat{\rho}_B$ of two lattices A and B with respective Hilbert spaces $\mathcal{H}_A$ and $\mathcal{H}_B$. Each density matrix can be

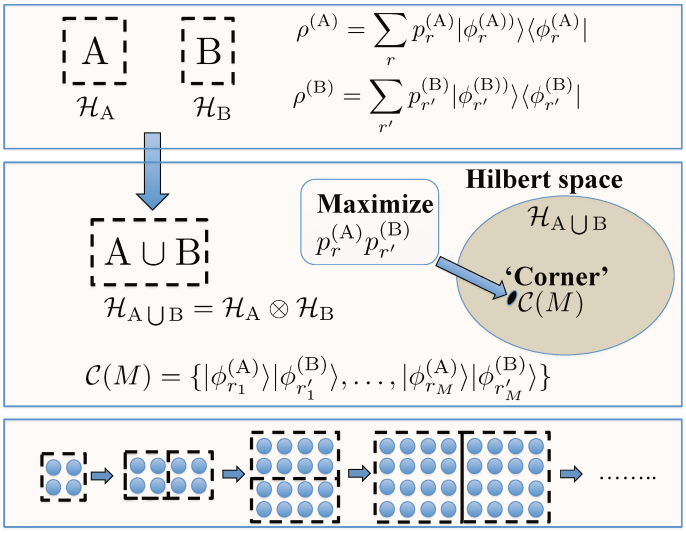

Figure 3.1: Sketch of the corner-space renormalization method.

diagonalized as

$$\hat{\rho}_A = \sum_r p_r^{(A)} |\psi_r^{(A)}\rangle\langle\psi_r^{(A)}|,$$
$$\hat{\rho}_B = \sum_r p_r^{(B)} |\psi_r^{(B)}\rangle\langle\psi_r^{(B)}|,$$

where the states $|\psi_r^{(A)}\rangle$ (respectively $|\psi_r^{(B)}\rangle$) form an orthonormal basis of the Hilbert space $\mathcal{H}_A$ (resp. $\mathcal{H}_B$) and $p_r^{(A)}$ (resp. $p_r^{(B)}$) are the corresponding probabilities. It is worth noting that each ket $|\psi_r^{(A)}\rangle$ represents a many-body state of the system A with no limitation on the correlations.

When the two lattices are merged, the Hilbert space becomes $\mathcal{H}_{A\cup B} = \mathcal{H}_A \otimes \mathcal{H}_B$ which can be spanned by the orthonormal basis $|\psi_r^{(A)}\rangle|\psi_{r'}^{(B)}\rangle$. To select a small "corner" $\mathcal{C}(M)$ of the larger space $\mathcal{H}_{A\cup B}$, we will consider the subspace spanned by the M most probable states of this basis ranked according to the *joint* probability $p_r^{(A)} p_{r'}^{(B)}$. Let us call $|\psi_{r_1}^{(A)}\rangle|\psi_{r'_1}^{(B)}\rangle$ the most probable product state, i.e. such that $p_{r_1}^{(A)} p_{r'_1}^{(B)} \geq p_r^{(A)} p_{r'}^{(B)}$ for every value of r and r'. We will call $|\psi_{r_2}^{(A)}\rangle|\psi_{r_2}^{(B)}\rangle$ the second most probable product state and so on and so forth. In other words, we will consider the subspace generated by the orthonormal basis

$$\left\{|\psi_{r_1}^{(A)}\rangle|\psi_{r'_1}^{(B)}\rangle, |\psi_{r_2}^{(A)}\rangle|\psi_{r'_2}^{(B)}\rangle, \ldots, |\psi_{r_M}^{(A)}\rangle|\psi_{r'_M}^{(B)}\rangle\right\}, \tag{3.2}$$

where

$$p_{r_1}^{(A)} p_{r'_1}^{(B)} \geq p_{r_2}^{(A)} p_{r'_2}^{(B)} \geq \ldots \geq p_{r_M}^{(A)} p_{r'_M}^{(B)}. \tag{3.3}$$

Thus we have selected the M most probable pairs of states. Note that the criterion we used is the joint probability, this implies that $p_{r_j}^{(A)}$ can be smaller than $p_{r_{j+1}}^{(A)}$ or $p_{r'_j}^{(B)}$ can be smaller than $p_{r'_{j+1}}^{(B)}$, but we always have $p_{r_j}^{(A)} p_{r'_j}^{(B)} \geq p_{r_{j+1}}^{(A)} p_{r'_{j+1}}^{(B)}$.

The states in Eq. (3.2) are eigenstates of the density matrix $\hat{\rho}_A \otimes \hat{\rho}_B$. In the limit of strong pumping and dissipation, correlations vanish and they become the exact eigenstates of the system density matrix. Therefore they are a natural basis to describe the driven-dissipative steady-state phases. Moreover, a generic state belonging to the corner, of the form $|\Psi\rangle = \sum_s c_s |\psi_{r_s}^{(A)}\rangle |\psi_{r'_s}^{(B)}\rangle$, can describe correlations and quantum entanglement between A and B while keeping correlations within A and B. As a result, the resolution of the master equation (3.1) can introduce correlations and entanglement between the subsystems A and B.

3.1.2 Convergence

The master equation (3.1) is solved in order to obtain the steady-state density matrix in the corner space. We emphasize that by arbitrarily increasing M, the method becomes exact because the considered basis spans the entire Hilbert space. Note that the convergence of the corner space is studied for observables $\mathcal{O}(M) = \mathrm{Tr}(\hat{\mathcal{O}}\hat{\rho}_{\mathcal{C}(M)})$. Hence, the number of states M to reach convergence depends on the considered observables. Since for driven-dissipative systems the correlation lengths are reduced by the presence of dissipation, convergence can be reached with a number of states M much smaller than the dimension of the Hilbert space, as it is shown below. This aspect will be detailed in the following as an example is considered.

3.2 Applications of the algorithm to driven-dissipative Bose-Hubbard models

In order to illustrate the proposed method, we consider the dissipative Bose-Hubbard model under a coherent drive. The Hamiltonian in the frame rotating at the pump frequency and for homogeneous pumping reads:

$$\hat{H} = \sum_j \left[-\Delta \hat{b}_j^\dagger \hat{b}_j + \frac{U}{2} \hat{b}_j^\dagger \hat{b}_j^\dagger \hat{b}_j \hat{b}_j + F(\hat{b}_j^\dagger + \hat{b}_j) \right] - \frac{J}{z} \sum_{<j,l>} \hat{b}_j^\dagger b_l \tag{3.4}$$

where $\Delta = \omega_p - \omega_c$ is the detuning between the pump and the bare boson frequency, U is the on-site boson-boson interaction and F is the amplitude of the pump field. J is the hopping coupling, z is the coordination number and $\sum_{<i,j>}$ denotes the sum over all the pairs of nearest neighbours. For simplicity, we have fixed the phase of the pump in such a way that F is real. Finally, each site is subject to losses with a dissipation rate γ.

3.2.1 Convergence for the corner-space dimension

In the following we focus on 4×4 lattices of hard-core bosons ($U/\gamma \to \infty$) for which the maximum number of boson per site is $N_{\max} = 1$. The dimension of the full Hilbert space for hard-core bosons on a 4×4 lattice is $2^{16} = 65536$ which can still be treated exactly.

Although it is computationally heavy, the master equation can be solved in the full Hilbert space using a Montecarlo wavefunction algorithm using the Fock number state basis and sparse matrices. This allows us to benchmark the corner-space renormalization method.

In table 3.1 we show the results for a lattice with periodic boundary conditions. These results have been obtained starting from a 2×2 lattice, merging two 2×2 and then doubling again, to get a 4×4 lattice. The table reports the results averaged over all the lattice sites for the boson population per site $n = \langle \hat{b}_j^\dagger \hat{b}_j \rangle$, the real part of the bosonic coherence $\Re(\langle b_j \rangle)$ and the nearest-neighbour correlation function: $g^{(2)}_{\langle i,j \rangle} = \langle \hat{b}_i^\dagger \hat{b}_j^\dagger \hat{b}_i \hat{b}_j \rangle / (n_i n_j)$. Note that for a factorized Gutzwiller-like density matrix $\hat{\rho}_G = \otimes_j \hat{\rho}_j$, $g^{(2)}_{\langle i,j \rangle} = 1$. Hence, the difference $g^{(2)}_{\langle i,j \rangle} - 1$ quantifies the degree of correlations between nearest-neighbours beyond mean-field theory. Moreover, for hard-core bosons, the second-order correlation function $g^{(2)} = \langle \hat{b}_j^\dagger \hat{b}_j^\dagger \hat{b}_j \hat{b}_j \rangle / n_j^2$ is always equal to 0 since two bosons cannot be on the same site.

Remarkably, for the parameters $J/\gamma = 1$, $F/\gamma = 2$, $z = 4$ and $\Delta/\gamma = 5$ corresponding to moderate correlations, table 3.1 shows that a very accurate result is obtained for a corner-space dimension as small as $M = 200$. Indeed, we find negligible error for n, namely 0.1% for the bosonic coherence and 0.3% for $g^{(2)}_{\langle i,j \rangle}$.

Similarly to table 3.1, in table 3.2, we gather the results for the number of photons n, the real part of the coherence $\Re(\langle \hat{b} \rangle)$ and the second-order nearest-neighbour correlation function $g^{(2)}_{\langle i,j \rangle}$ for the same parameters but with open boundary conditions instead of periodic ones. The results presented here were obtained by merging two 4×2 lattices. Convergence is achieved with a corner-space dimension $M = 400$: the estimation of the number of photons n and the real part of the coherence $\Re(\langle \hat{b} \rangle)$ are within the error bars of the Montecarlo wavefunction for the 4×4 lattice and there is a 0.8% error for $g^{(2)}_{\langle i,j \rangle}$.

In Fig. 3.2 we present the value of the site-dependent boson population on each site for open boundary conditions. The top panel has been obtained by solving the master equation considering the full Hilbert space (of dimension 65536) using a Montecarlo wavefunction algorithm. The statistical errors are due to the Montecarlo sampling procedure. The two bottom panels have been calculated with 400 (left) and 200 (right) states in the corner space. Notice that for these corner-space dimensions the integration of the master equation is done using a Runge-Kutta method. Hence, there are no statistical errors. Clearly, the boson population is intrinsically site-dependent in this case. For the considered positive detuning Δ the fact that the sites on the boundary have fewer neighbours than the ones in the bulk translate into a higher density of bosons. The results of corner-space renormalization method (bottom panels) are in very good agreement with the result in the full Hilbert space.

In the presence of driving, the influence of a specific boundary conditions is greatly reduced with respect to the equilibrium case [7]. Indeed, the spatial symmetry is imposed by the spatial shape of the driving field together with the dissipation and the correlations are limited by the dissipation processes. We emphasize that when the lattice size is in-

M	n	$\Re(\langle b \rangle)$	$g^{(2)}_{<j,l>}$
20	0.09443	0.2772	1.029
50	0.09469	0.2770	0.9693
100	0.09513	0.2768	0.9652
200	0.09541	0.2767	1.061
400	0.09544	0.2767	1.058
800	0.09549(3)	0.27671(5)	1.0644(1)
1600	0.09547(3)	0.27672(6)	1.0643(1)
65536	*0.0954(1)*	*0.2764(2)*	*1.0643(3)*

Table 3.1: Results of the corner-space renormalization method for the driven-dissipative Bose-Hubbard model with periodic boundary conditions and the following parameters: 4×4 square lattice ($z = 4$), $U = +\infty$ ($N_{max} = 1$, hard-core bosons), $J/\gamma = 1$, $F/\gamma = 2$, $\Delta/\gamma = 5$. The numbers in parenthesis indicate the statistical errors on the last significative digit due to finite Monte Carlo sampling when applied. In this example, the dimension of the full Hilbert space is $2^{16} = 65536$. The case of 65536 states has been solved by an independent Monte Carlo wavefunction code using a Fock basis for the entire space and sparse matrix calculations.

M	n	$\Re(\langle b \rangle)$	$g^{(2)}_{<j,l>}$
20	0.1004	0.2840	1.035
50	0.1008	0.2838	0.940
100	0.1011	0.2833	0.938
200	0.1013	0.2829	1.058
400	0.1013	0.2829	1.055
800	0.1014(8)	0.2829(9)	1.063(3)
1600	0.1013(8)	0.2828(9)	1.0624(3)
65536	*0.1012(9)*	*0.282(1)*	*1.064(2)*

Table 3.2: Convergence of the observables for different values of the corner-space dimension M for a 4×4 lattice with open boundary conditions (same parameters as in Fig. 3.2). The $M = 65536$ corresponds to the whole Hilbert space. Data with error bars have been calculated by solving the master equation via the Montecarlo wavefunction method. All the quantities are averaged over all the sites of the lattice.

creased through several spatial mergings, the convergence is ensured at each merging. In Fig. 3.3, the convergence for increasing values of the corner-space dimension M is illustrated for different lattice sizes for hard-core bosons with periodic boundary conditions (same parameters as in table 3.1). The results have been obtained by doubling the block size at each iteration. For each lattice size, the curve shows a convergence parameter

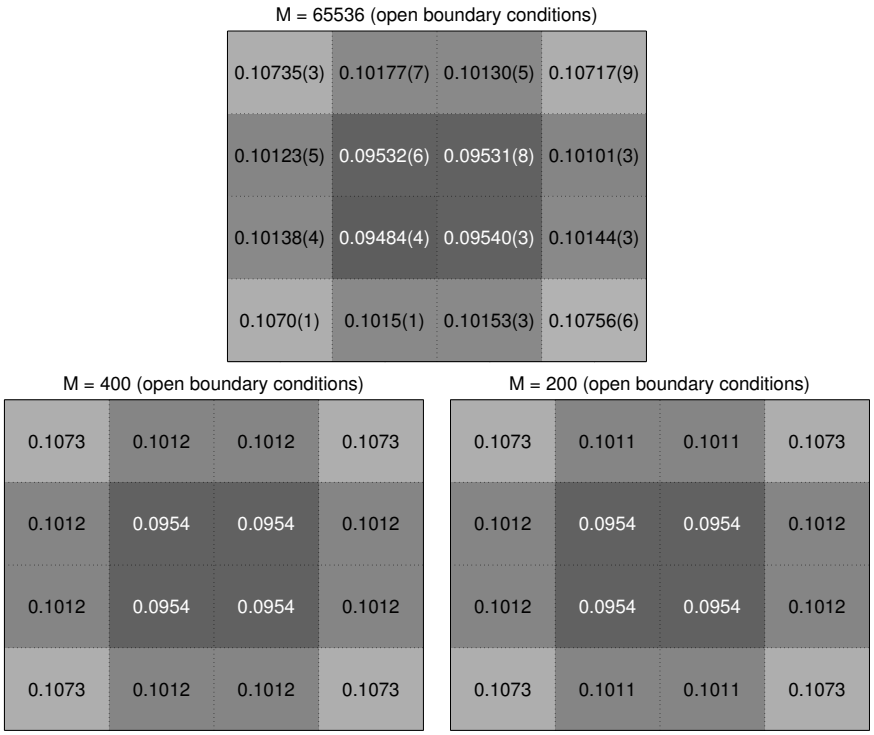

Figure 3.2: Site-dependent steady-state boson population for the driven-dissipative Bose-Hubbard model for a 4×4 square lattice ($z = 4$) with open boundary conditions. Parameters: $J/\gamma = 1$, $\Delta/\gamma = 5$, $U/\gamma = \infty$ (hard-core bosons). The results in the top panel have been obtained by considering the full Hilbert space (65536 states) via a Montecarlo wavefunction calculation (5500 quantum trajectories for the case of open boundary conditions). The bottom left panel is obtained with the corner-space renormalization method (obtained by merging two 4×2 lattices) and a number of states $M = 400$. The bottom right panel is obtained with only $M = 200$ basis states. The gray scale shades are a guide for the eye.

for the boson population, namely the quantity $u_n(M) = n(M)/n(M_{max})$ where M_{max} is the largest value of M considered. This convergence parameter is convenient to see the relative deviations and visualize the results for different lattice sizes in the same graph. The red dashed lines represent a deviation of $\pm 1\%$.

When the lattice size is increased, convergence is achieved for larger values of M. However, while the size of the Hilbert space grows exponentially with the number N of lattice sizes, the growth of M needed to obtain a given relative error is much milder. Moreover, we can extract the scaling of the corner-space dimension as a function of the number of sites N from Fig. 3.3. For the parameters considered here, when N is doubled, M must be multiplied approximately by 5. Thus, the value of M to obtain a given accuracy for this observable and this model follows a power-law, namely it scales as N^α with $\alpha \approx 2.3$.

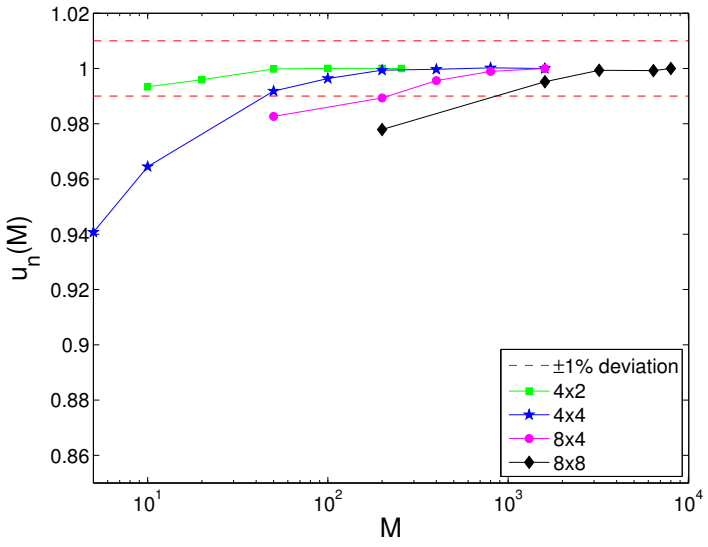

Figure 3.3: Convergence curves as a function of the corner space dimension M for different lattice sizes (see the legend in the inbox). For each lattice size, the boson population convergence parameter $u_n(M)$ (see definition in the text) is plotted. The dashed lines represent a $\pm 1\%$ deviation. Parameters: $J/\gamma = 1$, $\Delta/\gamma = 5$, $U/\gamma = \infty$ (hard-core bosons), $z = 4$ and periodic boundary conditions.

3.2.2 Application of the corner-space renormalization method to soft-core bosons

In order to explore the phase diagram for the coherently driven Bose-Hubbard model [47, 50], it is interesting to apply our method to the case of soft-core bosons ($U/\gamma < +\infty$). In this case, depending on the drive and the number of excited bosons, a brute-force numerical integration of the master equation can become out of reach even for lattice sizes as modest as 3×3. Indeed, the local boson cutoff $N_{\max}$ necessary to accurately recover the single-site physics is larger than one. For a cutoff $N_{\max} = 4$ the Hilbert space dimension is $5^9 \simeq 2 \times 10^6$, which is too big for an exact treatment.

In table 3.3, we present the results for soft-core bosons and a larger hopping coupling with respect to the previous section ($U/\gamma = 20$ and $J/\gamma = 3$). As shown by the convergence progression presented in table 3.3, results with deviation below 1% can be obtained for a corner-space dimension $M = 3200$, that is 6 orders of magnitude smaller than the full Hilbert space for a systam with large spatial correlations ($g^{(2)}_{\langle i,j \rangle} - 1 = 0.63$).

An example of the temporal dynamics leading to steady-state solutions is reported in Fig. 3.4, plotting n and g_2 for different lattice sizes. The corner method results are compared with the non-equilibrium mean-field approach used in Refs. [47, 50, 110], based on the exact analytical solution of the master equation for the one-site problem[96]. The initial condition for the density-matrix dynamics for the 2×2 lattice is the mean-field solution. After a transient, a steady-state solution is obtained. The initial condition for

M	n	$\Re(\langle b \rangle)$	g_2	$g^{(2)}_{<j,l>}$
20	0.0902	0.1967	1.646	1.28
50	0.1006	0.1907	1.513	1.34
100	0.1044	0.1886	1.454	1.26
200	0.0968	0.1922	1.324	1.51
400	0.1006	0.1905	1.291	1.51
800	0.1009(2)	0.1903(3)	1.242(3)	1.57(2)
1600	0.1014(2)	0.1896(2)	1.226(3)	1.58(2)
3200	0.1002(2)	0.1897(2)	1.185(2)	1.63(2)
6400	0.0994(2)	0.1899(2)	1.179(3)	1.63(1)

Table 3.3: Parameters: 4×4 square lattice ($z = 4$) with periodic boundary conditions, $U/\gamma = 20$, $J/\gamma = 3$, $F/\gamma = 2$, $\Delta/\gamma = 5$. A number $N_{max} = 3$ of bosons per site has been considered. In this case, the dimension of the full Hilbert space is $4^{16} \simeq 4.3 \cdot 10^9$.

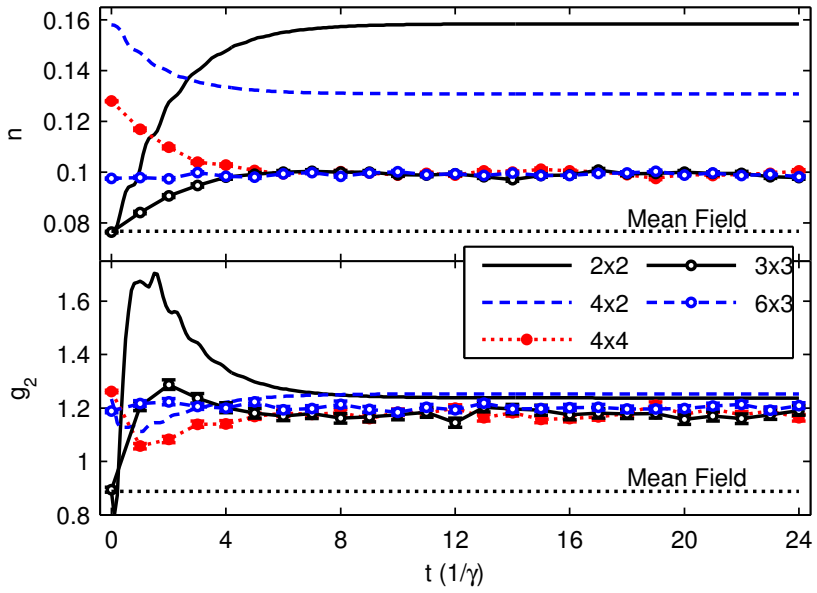

Figure 3.4: Evolution of n and g_2 versus time t (units of $1/\gamma$) for the driven-dissipative Bose-Hubbard model with periodic boundary conditions on lattices of various size for the following parameters: $U/\gamma = 20$, $J/\gamma = 3$, $F/\gamma = 2$, $\Delta/\gamma = 5$. Solid lines represents evolutions performed by direct integration of the master equation, while points depict Monte Carlo wavefunction calculations. When error bars are not shown, the statistical error is smaller than the point size. The black-dotted lines represent the mean-field values. The initial conditions for the 2×2 and 3×3 are the mean-field solution whereas the steady-state value for the 2×2 is the initial state for the 4×2, the 3×3 for the 6×3 and the 4×2 for the 4×4.

the 4×2 lattice is constructed from the steady-state solution of the 2×2 lattice and so on and so forth. We have also merged 3×1 clusters to get the 3×3 lattice and then the 6×3 case by doubling. We see that the steady-state observables for the 3×3, 4×4 and 6×3 lattices with periodic boundary conditions tend to converge to the same value, so the results are already approaching those for a lattice with an infinite number of sites. The finite spatial range of the correlations of the driven-dissipative system is responsible for such relatively quick convergence. For the parameters in Fig. 3.4, the deviations from the mean-field theory are around 20% for n and g_2.

	Mean-field		Corner method			
U/γ	n	g_2	$N_{\text{sites}}^{(M)}$	n	g_2	$g_{<j,l>}^{(2)}$
∞	0.0953	0	$8 \times 4^{(1600)}$	0.09527(2)	0	1.0436(3)
			$8 \times 8^{(8000)}$	0.0948(2)	0	1.0237(6)
20	0.125	0.836	$4 \times 4^{(3200)}$	0.1281(4)	0.859(4)	1.172(5)
			$6 \times 3^{(6400)}$	0.1282(9)	0.858(9)	1.173(4)
20*	0.0768	0.8879	$4 \times 4^{(6400)}$	0.0994(2)	1.179(3)	1.63(1)
			$6 \times 3^{(6400)}$	0.0992(1)	1.202(4)	1.65(1)
10	0.9587	0.6088	$4 \times 2^{(6400)}$	0.9275(8)	0.631(1)	1.0127(8)
			$3 \times 3^{(8000)}$	0.9281(9)	0.617(1)	1.0069 (6)
1	0.1156	1.265	$16 \times 8^{(600)}$	0.1156	1.259	0.9897
0.5	0.1126	1.112	$16 \times 16^{(400)}$	0.1126	1.1105	0.9941

Table 3.4: Parameters: $J/\gamma = 1$ (except the third line with the * sign, obtained with $J/\gamma = 3$), $F/\gamma = 2$ and $\Delta\omega/\gamma = 5$. The maximum number of bosons per site is $N_{\max} = 1$ for hard-core bosons, $N_{\max} = 3$ for $U/\gamma = 20$, $N_{\max} = 5$ for $U/\gamma = 10$, $N_{\max} = 4$ for $U/\gamma = 1$ and 0.5.

Finally, in table 3.4, we gather results for different lattices and compare them to mean-field solutions [47, 110]. We checked the convergence of the results with respect to M for errors below 0.5%. It is apparent that in the considered case the deviation from mean-field are rather small for hard-core bosons and a large 8×8 lattice, as quantified by a $g_{\langle i,j \rangle}^{(2)} - 1 \simeq 0.02$. Significant deviations are instead present when the on-site interaction U is competing with the hopping coupling J (the cases with $U/\gamma = 20$ and $J/\gamma = 1$ and 3 in Table 3.4). For example, the value for $U/\gamma = 10$ and $J/\gamma = 1$ is close to a two-photon resonance [110] and indeed the the population of bosons per site is much higher (close to one boson per site) with the on-site g_2 correlation function quite close to 0.5. For $U/\gamma = 0.5$, it is possible to simulate very large lattices (a 16×16 lattice is reported) with a very small number of states ($M = 400$).

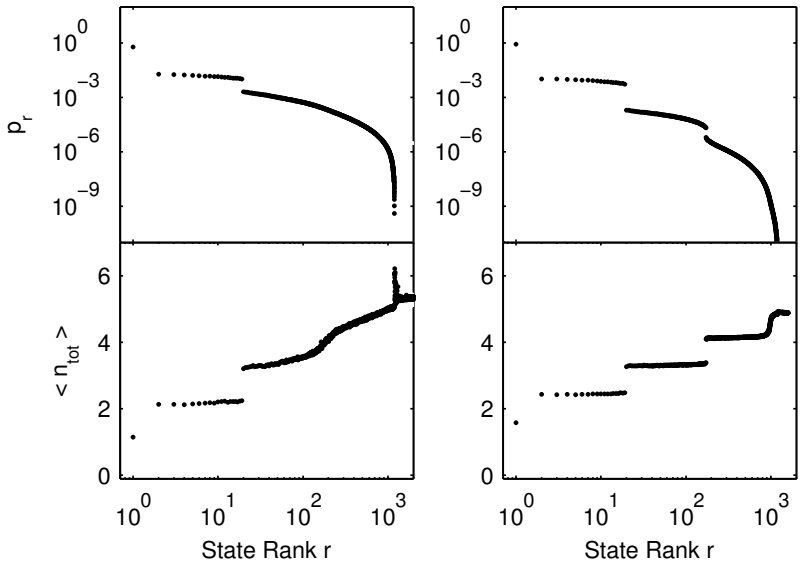

Figure 3.5: Probabilities p_r (top panels, logarithmic scale) and expectation value of the total boson population $\langle n_{\rm tot}\rangle = \sum_j \langle n_j\rangle$ for the orthonormal eigenvectors $|\Psi_r\rangle$ of the steady-state density-matrix ($\hat{\rho} = \sum_r\ p_r|\Psi_r\rangle\langle\Psi_r|$ and $p_r \geq p_{r+1}$). The state rank r is in logarithmic scale. Lattice size: 6×3. Driving parameters: $F/\gamma = 2$, $\Delta\omega/\gamma = 5$. Left: $U/\gamma = 20$ and $J/\gamma = 3$. Right: hard-core bosons with $J/\gamma = 1$.

3.3 Limitations of the method

Computationally, the main limitation comes from the memory usage. It can be estimated as a function the number of sites $N_{\rm sites}$ as $O(N_{\rm sites}M^2)$ where M is the dimension of the corner-space, since there are $N_{\rm sites}$ jump operators.

Physically, if we consider the diagonal decomposition of the steady-state density matrix $\hat{\rho} = \sum_r p_r|\Psi_r\rangle\langle\Psi_r|$ where $p_r > p_{r+1}$, convergence will be met more easily when the probabilities p_r decrease fast. Visually, this can be appreciated from the probability spectra as the ones plotted in Fig. 3.5 in which we show an example of the probability distribution p_r (top panels, logarithmic scale). For the bottom panels, we show the expectation value of the total number of bosons in the lattice versus the state rank r for a 6×3 lattice of soft-core bosons with $U = 20\gamma$ (left panels) and hard-core bosons (right panels). In the hard-core boson case, a rather well definite shell structure is apparent. The first state ($r = 1$), which captures a large part of probability, is followed by shells of states having close probabilities and densities. In the case of a homogeneous system, a factorized Gutzwiller density-matrix with each site having the same reduced density-matrix leads to a shell structure with exactly flat plateaux structures due to symmetry reasons. In fact, a permutation of the role of the different sites does not change the probability of a state and observables like n_{tot}, which is a sum of the photon number over all the sites. In the right panel of Fig. 3.5 (hard-core boson case), the situation is qualitatively close to the Gutzwiller case, even though the plateaux are not exactly flat.

In the case of soft-core bosons in the left panel of Fig. 3.5, a first shell is clearly visible, while higher shells merge into a continuous curve where the different quantities increase gradually, denoting a large degree of correlations (indeed $g^{(2)}_{<j,l>} - 1 \simeq 0.6$ in the case considered).

Moreover, we observe that after the first plateau, the decrease in probability is sharper in the hard-core bosons case (left panel) than in the soft-core one (right panel). As a result, a much bigger dimension of the corner space is required to achieve convergence in the strongly correlated case ($M = 6400$) with respect to the hard-core case ($M = 1600$).

The main limitation of the method is linked to the von Neumann entropy of the system:

$$S = -\mathrm{Tr}\left[\hat{\rho}\ln(\hat{\rho})\right] = -\sum_r p_r \ln(p_r). \tag{3.5}$$

Indeed, lower entropy requires a lower dimension for the corner space. For example, in the limit of $\hat{\rho}$ being a quasi-pure state, we have $S \simeq 0$ and the corner-space dimension tends to one. In the opposite limit of a density matrix where all the states have the same probability, the entropy is maximal, namely $S = N\ln(N)$ (N being the Hilbert space dimension) and the corner-space renormalization method cannot converge until the complete Hilbert space is considered. The link between the entropy and the convergence of the corner-space renormalization method will be further discussed in Chapter 4.

In contrast, note that the limiting factor in MPO method is not the entropy of the density matrix but long-range correlations, which can require too large bond-link dimension to reach convergence (see Chapter 5).

3.4 Conclusion

In this chapter, we have presented a theoretical method for driven-dissipative correlated lattice systems. The proposed numerical algorithm follows a hybrid real-space renormalization group approach: the states considered for the computations in large lattices are selected as product-states of the eigenvectors of the steady-state density matrices in smaller systems, in order to maximize their joint probability. We have successfully benchmarked the method by applying it to the driven-dissipative Bose-Hubbard model on two-dimensional square lattices. Unlike mean-field theories, where the decoupling approximation is not controlled, the present numerical method allows us to get results with controllable accuracy, depending on the dimension of the corner space.

In the following chapters, the proposed method will be applied to anisotropic Heisenberg spin lattices (Chapter 4) and to the incoherently pumped Bose-Hubbard model (Chapter 5).

Chapter 4

Critical behaviour in the 2D XYZ model

The emergence of phase transitions in extended driven-dissipative quantum systems raises many question. In particular, the extent and the critical behaviour of quantum correlations as a function of the system size is yet to be explored in conjunction with the mixed nature of the steady-state. Moreover, the computation of the steady-state of extended lattices is of an outstanding difficulty. As a result, the evaluation of critical exponents at the transition remains an open problem. The main advance in that direction has been obtained using the Keldysh functional formalism in a renormalization group approach. This has allowed to show some thermodynamic limit aspects of phase transitions for boson systems [127, 128, 129] or for spin systems [67]. However, up to now, such formalism has not allowed to study the role of quantum correlations in dissipative phase transitions.

In this chapter, we focus our study on a physical system undergoing a genuine dissipative phase transition that has recently been under intense study [48, 52]: a non-equilibrium anisotropic Heisenberg XYZ model for a lattice of 1/2-spins. A single-site mean-field analysis shows that the system undergoes a transition (among others) between a phase where all the spins are aligned along the z-axis to a phase where a non-zero magnetization in the xy-plane appears. Furthermore, a cluster mean-field study of that transition shows that it survives in two dimensions, and MPO simulations showed that there is no transition in one dimension [52].

The first section of this chapter introduces the XYZ model and reviews the mean-field phase diagram obtained in previous studies [48, 52].

In section 4.2, we show results for two-dimensional lattices obtained with the corner-space renormalization method being able to evaluate the critical exponents for the magnetic susceptibility and the quantum correlations. Furthermore, we studied the behaviour of the entropy across the critical region as a function of the system size, showing that the transition shares properties from both thermal and quantum phase transitions. Moreover, we also present calculations of the Liouvillian gap. For comparison, a finite-

size analysis in the one-dimensional case is performed in the last section.

This work was done in a collaboration with Riccardo Rota, Nicola Bartolo under the direction of Rosario Fazio and Cristiano Ciuti. The main results of the second section have been published in *Physical Review B* [122].

4.1 Dissipative XYZ Model

We consider a two-dimensional lattice of 1/2-spins governed by the Heisenberg XYZ Hamiltonian:

$$\hat{H} = \sum_{<i,j>} \left(J_x \hat{\sigma}_i^x \hat{\sigma}_j^x + J_y \hat{\sigma}_i^y \hat{\sigma}_j^y + J_z \hat{\sigma}_i^z \hat{\sigma}_j^z \right), \tag{4.1}$$

with $\hat{\sigma}_i^x$, $\hat{\sigma}_i^y$ and $\hat{\sigma}_i^z$ being the x, y and z Pauli matrices for site i. Losses enter the master equation through on-site spin flip operators $\hat{\sigma}_i^-$, occurring at a rate γ:

$$\partial_t \rho = -\mathrm{i}[\hat{H}, \hat{\rho}] + \frac{\gamma}{2} \sum_{i=1}^{N_{\text{sites}}} (2\hat{\sigma}_i^- \hat{\rho} \hat{\sigma}_i^+ - \hat{\sigma}_i^+ \hat{\sigma}_i^- \hat{\rho} - \hat{\rho} \hat{\sigma}_i^+ \hat{\sigma}_i^-). \tag{4.2}$$

Even if at first glance in Eq. (4.2) no driving term seems to be present in the system, the considered model is not at equilibrium. Indeed, since in the case of an anisotropic coupling ($J_x \neq J_y$) the jump operators are not commuting with the Hamiltonian, dissipation will not lead the system to the ground state of $\hat{H}$. Indeed, as we show in the next section, this master equation can describe the dynamical behaviour of laser drives on an atomic cloud creating dressed atomic states that will give Eq. (4.2).

4.1.1 Experimental implementation

We detail here an experimental proposal to realize the effective model given by the Hamiltonian (4.1). Even though this model does not directly describe a physical system, it is a relevant description of realistic experiments. In particular, this proposal is based on Rydberg atoms that are pumped using a two-photon scheme [48]. The two-photon pump is used to create and tailor effective interactions between the nearest-neighbouring atoms.

For the sake of simplicity, we consider two two-level systems (we denote the ground state of the atom $|g\rangle$ and the excited state $|e\rangle$). The Hamiltonian describing the two neighbouring atoms is:

$$\hat{H}_{\text{ryd}} = \omega(\hat{\sigma}_1^z + \hat{\sigma}_2^z) + V \hat{\sigma}_1^{ee} \hat{\sigma}_2^{ee}, \tag{4.3}$$

with, ω being the resonance frequency of the atom, V denoting the frequency shift induced by the dipole-dipole interaction and $\hat{\sigma}_j^{ee} = |e\rangle\langle e|_j$. The atoms are pumped using four lasers of different frequencies Ω_1, Ω_2, Ω_3 and Ω_4. Moreover, the lasers are detuned from the atom frequency by a detuning Δ. This excitation scheme is presented in Fig. 4.1. More details can be found in Ref. [48].

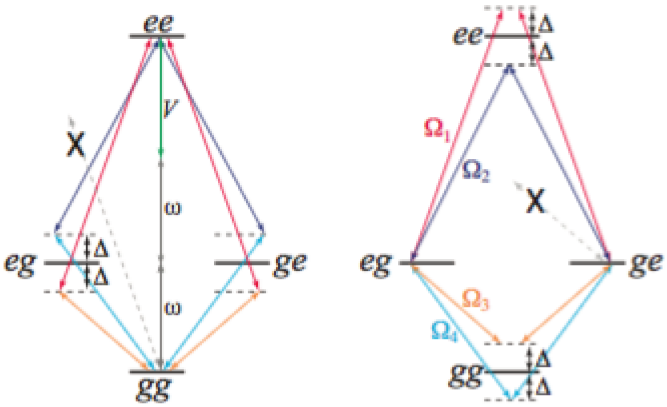

Figure 4.1: Level structure and laser coupling to synthesize the anisotropic Heisenberg XYZ Hamiltonian. The levels are coupled using four lasers of frequencies Ω_1, Ω_2, Ω_3 and Ω_4. The frequencies are chosen so that the pairs (Ω_1, Ω_3) and (Ω_2, Ω_4) are at the two-photon resonance. A detuning $\Delta \ll V$ is introduced between the lasers and the frequency of the atoms. The left panel represents the squeezing interaction where both spins are raised or lowered at the same time. The right panel represents the flip-flop processes that transfer an excitation from one atom to the other. From Lee *et al.* [48].

As a result of the pumping scheme, two types of effective interactions are introduced between the Rydberg atoms. The first one is a squeezing interaction (left panel of Fig. 4.1) that reads $J_{sq}(\hat{\sigma}_1^+\hat{\sigma}_2^+ + \hat{\sigma}_1^-\hat{\sigma}_2^-)$. This Hamiltonian describes the process in which the pump promotes both atoms in the excited state. The second effective interaction is the transfer of one excitation from one atom to another mediated by the lasers. This reads $J_{ff}(\hat{\sigma}_1^+\hat{\sigma}_2^- + \hat{\sigma}_2^+\hat{\sigma}_1^-)$ (right panel of Fig. 4.1).

The transfer of excitations and the squeezing interaction are essential ingredients to synthesize the XYZ Hamiltonian. Indeed, rewriting these two interactions with the Pauli matrices $\hat{\sigma}^x$ and $\hat{\sigma}^y$ we obtain:

$$J_{sq}(\hat{\sigma}_1^+\hat{\sigma}_2^+ + \hat{\sigma}_1^-\hat{\sigma}_2^-) = \frac{J_{sq}}{2}(\hat{\sigma}_1^x\hat{\sigma}_2^x - \hat{\sigma}_1^y\hat{\sigma}_2^y), \tag{4.4}$$

$$J_{ff}(\hat{\sigma}_1^+\hat{\sigma}_2^- + \hat{\sigma}_2^+\hat{\sigma}_1^-) = \frac{J_{ff}}{2}(\hat{\sigma}_1^x\hat{\sigma}_2^x + \hat{\sigma}_1^y\hat{\sigma}_2^y). \tag{4.5}$$

Therefore, if we write $J_x = (J_{ff} + J_{sq})/2$ and $J_y = (J_{ff} - J_{sq})/2$, we recover the x and y components of the XYZ Hamiltonian. Furthermore, detuning the lasers from the 2 photon resonance will give the z component, allowing to reconstruct the total Hamiltonian.

4.1.2 Emergence of the phase transition at mean-field level

Lee *et al.* first explored the XYZ model via a Gutzwiller mean-field analysis producing a rich phase diagram. In Ref. [48], four different phases have been predicted at the

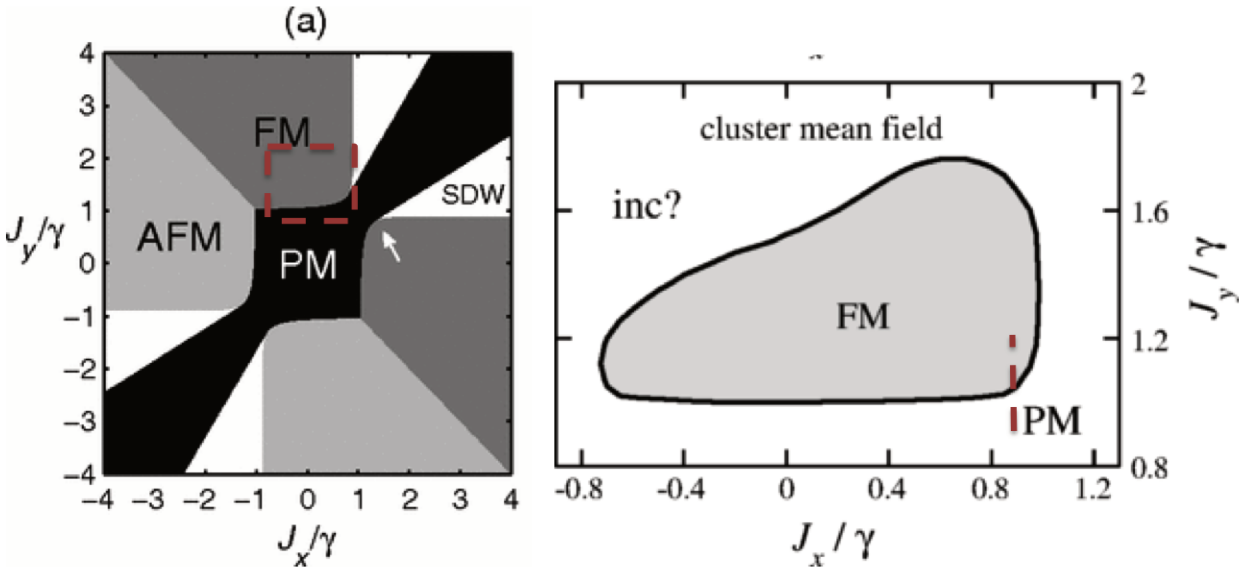

Figure 4.2: Phase diagram for the dissipative XYZ model with $J_z = \gamma$. The left panel is obtained with a mean-field analysis [48]. Four different phases appear: ferromagnetic (FM), antiferromagnetic (AFM), paramagnetic (PM) and spin density waves (SDW). The right panel is obtained using cluster mean-field [52]. It is a close up on the red dashed line box of the right panel. We can see that the PM and the FM phases survive when we consider short range correlations.

mean-field level. The first one is a paramagnetic phase (noted PM in Fig. 4.2): the decay dominates over the Hamiltonian part, the spins align in the z direction and there is no magnetization in the xy plane. When J_x and J_y are different enough, the system is driven into in a non-trivial magnetic state. Under the mean-field approximation, the spins are submitted to an effective magnetic field $\vec{h}_{eff}$ in the xy plane:

$$\vec{h}_{eff} = \begin{pmatrix} J_x\langle\hat{\sigma}^x\rangle \\ J_y\langle\hat{\sigma}^y\rangle \end{pmatrix}. \tag{4.6}$$

As a result, the local magnetization in the xy plane becomes finite. Nonetheless, a small magnetization in the z direction is always present in the steady-state. Different ordered phases have been predicted depending on the values of J_x and J_y resulting in the rich phase diagram shown in the left panel of Fig. 4.2.

In order to check if the different phases survive beyond the mean-field approximation, a cluster mean-field analysis was performed in Ref. [52]. This analysis considered finite-size lattices (up to 4×4) with a mean-field coupling at the boundary, so that short range correlations are included. The right panel of Fig. 4.2 is the result of the cluster mean-field analysis. The corresponding parameter region is highlighted by the red dashed line box in the left panel. Figure 4.2 shows that the ferromagnetic phase survives the inclusion of correlations for small values of J_y but that the phase disappears for large J_y. This could be due to the appearance of states that are incommensurable with the

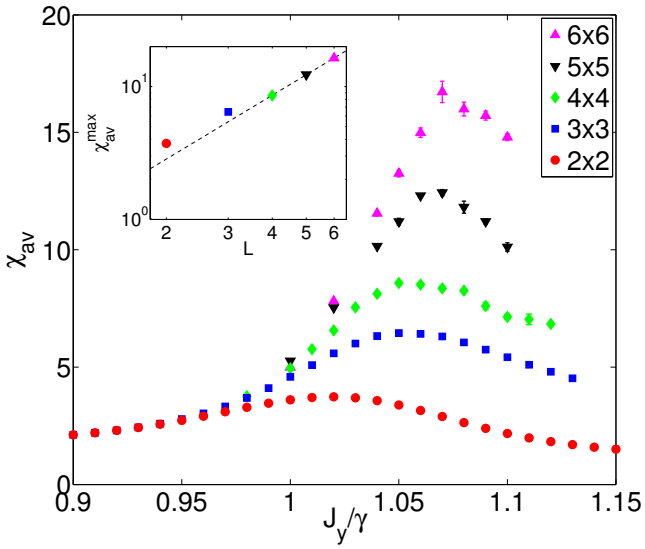

Figure 4.3: Angularly averaged susceptibility (Eq. (4.11)) as a function of J_y, for different lattice sizes. The other parameters are $J_x = 0.9\gamma$ and $J_z = \gamma$. The inset shows the value of $\chi_{av}^{\max}$ as a function of the lattice size L. The dotted line is a power-law fit of the finite-size analysis. When not shown, the error bars are smaller than the symbols. All the simulations were done with periodic boundary conditions.

size of the cluster under consideration (region noted inc? on the right panel of Fig. 4.2).

4.2 Results with the corner-space renormalization method

In the following, we study the phase transition from a paramagnetic to ferromagnetic phase along the red dashed line of the right panel of Fig. 4.2. Applying the corner-space renormalization method (see Chapter 3), we investigated the critical behaviour at the transition.

In order to address criticality quantitatively, we have performed a finite-size analysis. In a phase transition, when the number of sites is increased some quantities should diverge. In our case, we consider the magnetic susceptibility, the von Neumann entropy and entanglement witnesses: the negativity [130] and the Quantum Fisher Information [131, 132, 133, 134].

4.2.1 Magnetic susceptibility

In general, a crucial indicator for a paramagnetic to ferromagnetic phase transition is the magnetic susceptibility $\hat{\chi}$: this quantity measures the response of the magnetization of the system when a small magnetic field is applied.

Since the system under study is anisotropic, the response of the magnetization in the xy plane depends on the direction of the magnetic field $\vec{h} = h(\cos(\theta), \sin(\theta))^T$ ($(\bullet)^T$

representing the transpose operation) producing the perturbation

$$\hat{H}_{ext}(h,\theta) = \hat{H} + \sum_i \left[h\cos(\theta)\hat{\sigma}_i^x + h\sin(\theta)\hat{\sigma}_i^y\right]. \tag{4.7}$$

The resulting magnetization $\vec{M}$ can be measured in the xy plane:

$$\vec{M}(h,\theta) = \frac{1}{L^2}\begin{pmatrix} \langle\sum_j \hat{\sigma}_j^x\rangle \\ \langle\sum_j \hat{\sigma}_j^y\rangle \end{pmatrix} = \begin{pmatrix} \chi_{xx} & \chi_{xy} \\ \chi_{yx} & \chi_{yy} \end{pmatrix} \cdot \begin{pmatrix} h\cos(\theta) \\ h\sin(\theta) \end{pmatrix}, \tag{4.8}$$

with L being the size of the $L \times L$ lattice. The induced magnetization depends on the susceptibility tensor characterized by the matrix elements:

$$\chi_{\alpha\beta} = \left.\frac{\partial M_\alpha}{\partial h_\beta}\right|_{h\to 0}, \tag{4.9}$$

where

$$M_\alpha = \frac{1}{L^2}\sum_{i=1}^{L^2} \mathrm{Tr}(\hat{\sigma}_i^\alpha \hat{\rho}). \tag{4.10}$$

In order to evaluate the size dependence, it is more convenient to deal with a scalar value. Hence, we take the angular average of the susceptibility tensor:

$$\chi_{av} = \frac{1}{2\pi}\int_0^{2\pi} \mathrm{d}\theta \left.\frac{\partial|\vec{M}(h,\theta)|}{\partial h}\right|_{h\to 0}. \tag{4.11}$$

The averaged susceptibility is plotted in Fig. 4.3 for different $L \times L$ lattices with L going from 2 to 6 and with the parameters $J_x = 0.9\gamma$ and $J_z = \gamma$. For all values of L, χ_{av} exhibits a peak close to $J_y \approx 1.05\gamma$. The peak value of χ_{av}, $\chi_{av}^{\max}(L)$ obtained for $J_y^{\max}(L)$, increases following a power law:

$$\chi_{av}^{\max}(L) \propto L^\kappa, \tag{4.12}$$

with κ being the critical exponent for the susceptibility. This power law behaviour is shown in the inset of Fig. 4.3. The best fit with the available data gives:

$$\kappa = 1.59 \pm 0.10.$$

By doing a critical scaling of $J_y^{\max}(L)$, we can also estimate the critical value of the coupling J_y, $J_y^{(c)} \simeq 1.07 \pm 0.02$. For comparison, in Ref. [52] via a 4×4 cluster mean-field solution, it was found that the transition occurs for $J_y \simeq 1.03$.

The computation of χ_{av} is rather demanding: for each value of the parameters J_y we compute the magnetization for four different amplitudes h of the magnetic field both applied on the x and the y components. This corresponds to $\theta = \pi$ and $\theta = \pi/2$ in Eq. (4.7).

Note that for $L \leq 3$, the master equation was solved in the full Hilbert space by integrating it exactly using a Runge-Kutta algorithm. For larger lattices than 4×4, we used the corner-space renormalization method detailed in Chapter 3. The hardest point, the 6×6 lattice with highest J_y required a week of computation time (5000 was the dimension of the Hilbert space to reach convergence).

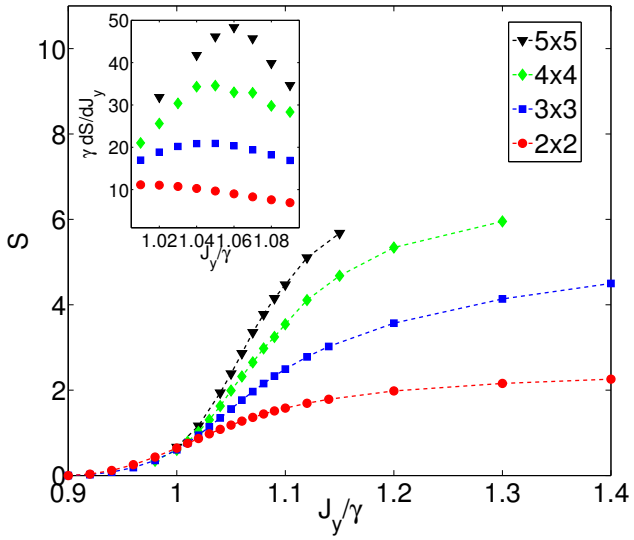

Figure 4.4: Von Neumann entropy S as a function of the normalized coupling parameter J_y/γ for different values of the size L of the square lattice. Same parameters as in Fig. 4.3. Inset: the derivative of the entropy with respect to the coupling parameter J_y .

4.2.2 Entropy of the system density matrix

In thermal phase transitions, the entropy shows signatures of the transition from an ordered to a disordered phase. However, in a quantum phase transition at zero temperature the ground state is a pure state, so its entropy is always zero.

Let us recall the von Neumann entropy associated with the system density matrix:

$$S = -\mathrm{Tr}(\hat{\rho}\ln\hat{\rho}) = -\sum_{i=1}^{\dim(\mathcal{H})} p_i \ln p_i, \tag{4.13}$$

where $\hat{\rho} = \sum_i p_i |\psi_i\rangle\langle\psi_i|$ and $\{|\psi_i\rangle\}$ form the orthonormal basis of the eigenvectors of $\hat{\rho}$. The eigenvalues p_i are the corresponding probabilities.

In Fig. 4.4, the entropy S is plotted as a function of J_y across the critical region. For $J_y \simeq J_x$ the entropy is small (zero in the isotropic coupling case). As the dissipation dominates the system dynamics, the resulting steady-state is close to the trivial state: $\hat{\rho} \approx |\downarrow\downarrow\downarrow\cdots\downarrow\rangle\langle\downarrow\cdots\downarrow\downarrow\downarrow|$. For larger J_y, we observe an abrupt increase of the entropy close to the critical point. As a result, there is peak in the derivative of the entropy $\partial S/\partial J_y$ close to the critical point. This can be seen in the inset of Fig. 4.4 that shows the derivative of the entropy with respect to J_y across the critical region. When the size of the lattice increases the peak gets sharper and more pronounced. By fitting the maximum of the $\partial S/\partial J_y$ with a power law,

$$\left(\frac{\partial S}{\partial J_y}\right)^{\max} \propto L^{\lambda}, \tag{4.14}$$

we find the critical exponent $\lambda = 1.6 \pm 0.2$.

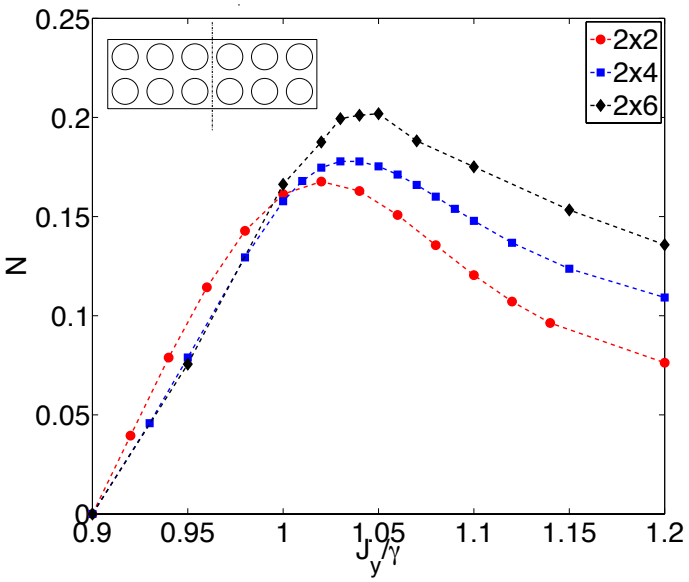

Figure 4.5: Entanglement negativity $\mathcal{N}$ vs. the normalized coupling parameter J_y/γ for small lattices. Same parameters J_x/γ and J_z/γ as in Fig. 4.3. Inset : sketch of the separation of the two subsystems in the 2×6 case.

The behaviour of the von Neumann entropy when J_y is varied across the phase boundary is reminiscent of the behaviour of the entropy during thermal phase transitions when the temperature varies across the critical temperature. In this analogy, the derivative $\partial S/\partial J_y$ plays the role of the specific heat in classical phase transitions.

4.2.3 Entanglement witnesses

A key feature of quantum phase transitions is the critical behaviour of quantum correlations. In that perspective, we studied two entanglement witnesses, the negativity [130] and the Quantum Fisher Information [131, 132, 133, 134].

An entanglement witness is a quantity whose value fulfilling a given condition implies the presence of entanglement. To sum up, if the entanglement witness shows entanglement then it is present, but the the reciprocal is not necessarily true. As a result, studying several entanglement witness can be necessary. Indeed, if the presence of entanglement is not indicated by a witness it can be by another one.

In order to define the negativity, we consider a lattice that can be divided in two subsystems A and B. The Hilbert space of the system can be written $\mathcal{H} = \mathcal{H}_A \otimes \mathcal{H}_B$. It is convenient to use an orthonormal basis of product states $|\phi_i^A; \phi_j^B\rangle$. Using this base, we can compute the partial transpose of $\hat{\rho}$ with respect to A:

$$\langle \phi_k^A; \phi_i^B | \hat{\rho}^{T_A} | \phi_l^A; \phi_j^B \rangle = \langle \phi_l^A; \phi_i^B | \hat{\rho} | \phi_k^A; \phi_j^B \rangle. \tag{4.15}$$

The key point in the computation of the negativity is that in the presence of entanglement

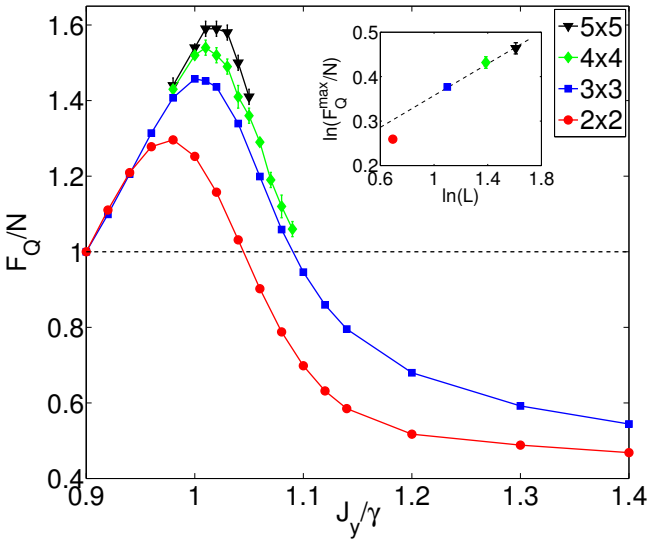

Figure 4.6: Quantum Fisher Information F_Q/N (normalized by the number $N = L^2$ of sites in the square lattice) as a function of the normalized coupling parameter J_y/γ for different sizes L. Same parameters as in Fig. 4.3. The inequality $F_Q/N > 1$ witnesses bipartite entanglement. Inset: maximum value of F_Q/N versus the lattice size L (log-log scale) with a power-law fit (dashed line).

the partial-transposed matrix $\hat{\rho}^{T_A}$ is not necessarily a density matrix. In particular, it may have negative eigenvalues, a sufficient condition to witness entanglement. The negativity is defined as

$$\mathcal{N} = \frac{\|\hat{\rho}^{T_A}\|_1 - 1}{2}, \tag{4.16}$$

where $\|\cdot\|_1$ denotes the trace norm, $\|\hat{A}\|_1 = \mathrm{Tr}(\sqrt{\hat{A}^\dagger \hat{A}})$. When $\hat{A}$ is Hermitian, the trace norm is the sum of the absolute values of the eigenvalues. Hence, a finite $\mathcal{N}$ measures entanglement.

The computation of the negativity $\mathcal{N}$ requires the diagonalization of a non-hermitian matrix obtained by partial transpose of the density operator. These operations are very sensitive the truncation errors in the corner space, so that the corner-space renormalization method is not efficient to compute this quantity and we are limited to small lattices.

The negativity $\mathcal{N}$ is represented across the critical region for different lattice sizes in Fig. 4.5. Close to the critical point, a peak appears and becomes more pronounced as the size of the lattice increases, suggesting a critical behaviour of quantum correlations. Furthermore, the negativity indicates that entanglement is present on the ferromagnetic side of the transition for couplings $J_y \gtrsim 1.15$. This is a good indicator of the quantum nature of the ferromagnetic phase.

The difficulty to compute the negativity for larger lattices motivated us to study another entanglement witness: the Quantum Fisher Information. For a mixed quantum

state $\hat{\rho} = \sum_r p_r |\psi_r\rangle\langle\psi_r|$, the Quantum Fisher Information is defined as:

$$F_Q = 2 \sum_{r,r'} \frac{(p_r - p_{r'})^2}{p_r + p_{r'}} |\langle\psi_r|\hat{\mathcal{O}}|\psi_{r\prime}\rangle|^2 \ , \tag{4.17}$$

where we include only terms with $p_r + p_{r'} > 0$ and the operator $\hat{\mathcal{O}}$ is a sum of on-site operators ($\hat{\mathcal{O}} = \sum_{i=1}^{N_{\text{sites}}} \hat{\mathcal{O}}_i$) with a spectrum width of 1 (the spectrum width is the difference between the maximum and the minimum eigenvalues). The Quantum Fisher Information has been used to witness multipartite entanglement in quantum phase transitions and at thermal equilibrium [131, 132, 133, 134, 135]. Indeed if $F_Q/N > m$ then there is $m+1$-partite entanglement. Hence, $F_Q > 1$ is a sufficient condition for bipartite entanglement [135].

Since the order parameter of the phase transition is the magnetization in the xy plane, we considered $\mathcal{O} = \frac{1}{2}\sum_i [\cos(\tau)\hat{\sigma}_i^x + \sin(\tau)\hat{\sigma}_i^y]$ where τ is chosen to maximize F_Q. Furthermore, the value of F_Q can be computed using the corner-space renormalization method in a convenient and straightforward way. Indeed, the eigenvalues p_r and local observables are directly calculated. As a result, we have been able to compute F_Q for lattice sizes up to 5×5 sites.

In Fig. 4.6, the value of F_Q/N is shown as a function of J_y across the critical region. Close to the critical value J_c, we can observe that $F_Q/N > 1$, which is a signature of bipartite entanglement. Moreover, the peak close to the critical point gets more pronounced when the size of the lattice is increased. In the inset of Fig. 4.6 we plotted the maximal value of F_Q/N as a function of the lattice size L in logarithmic scale. The dotted line is a power law fit that is matching the data very well for $L \geq 3$:

$$\left(\frac{F_Q}{N}\right)^{\max} \propto L^{\eta}, \quad \eta = 0.18 \pm 0.03. \tag{4.18}$$

This is a signature of the critical behaviour of entanglement at the transition. However the growth is much slower than the one of the susceptibility.

The critical behaviour of the Quantum Fisher Information and of the derivative of the entropy is a key result in the understanding of dissipative phase transitions. Indeed, they show properties of both quantum and thermal phase transitions.

4.2.4 Liouvillian gap

As mentioned in the first chapter, in a dissipative phase transition the gap between the two first eigenvalues of the Liouvillian super operator $\mathcal{L}$ plays a similar role to the gap between the two first eigenvalues of the Hamiltonian in a quantum phase transition.

In order to evaluate the Liouvillian gap, we investigate the dynamics of the magnetization along the x component: $\langle\hat{\sigma}^x(t)\rangle = 1/L^2 \sum_i \langle\hat{\sigma}_i^x(t)\rangle = 1/L^2 \sum_i \mathrm{Tr}(\hat{\sigma}_i^x \hat{\rho}(t))$. Figure 4.7 shows the dynamics of $\langle\hat{\sigma}^x(t)\rangle$ for a 4×4 lattice and different values of J_y close to the transition. The curves, presented in logarithmic scale, show a clear exponential decay

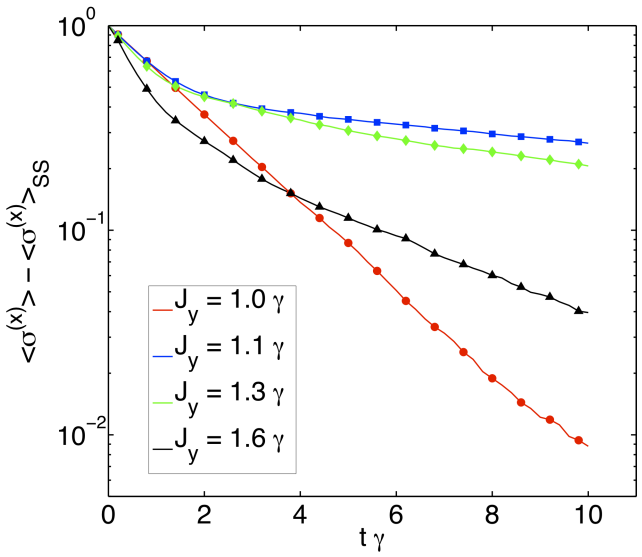

Figure 4.7: Time evolution of $\langle\hat{\sigma}^x\rangle(t) - \langle\hat{\sigma}^x\rangle_{\rm SS}$ for a 4×4 lattice with $J_z = \gamma$, $J_x = 0.9\gamma$ and $J_y = \gamma$ (red •), $J_y = 1.1\gamma$ (blue ■), $J_y = 1.3\gamma$ (green ♦) and $J_y = 1.6\gamma$ (black ▲). In the steady state, $\langle\hat{\sigma}^x\rangle_{\rm SS} = 0$. From Ref. [136].

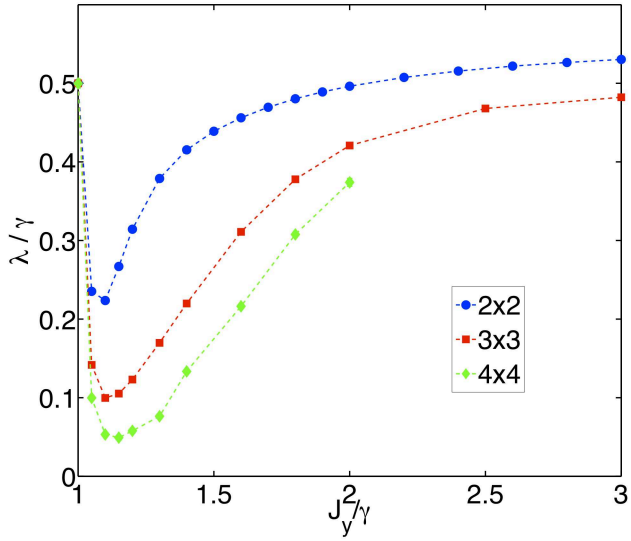

Figure 4.8: Liouvillian gap λ normalized by γ as a function of the normalized coupling J_y/γ across the critical region. The other parameters are the same as in Fig. 4.3. The calculations were done in the full Hilbert space with spatial periodic boundary conditions. From Ref. [136].

to 0 in the long time limit. Note that, since no external field is applied to the system, $\langle\hat{\sigma}^x\rangle = 0$ in the steady state for both phases. Hence, the Liouvillian gap λ corresponding

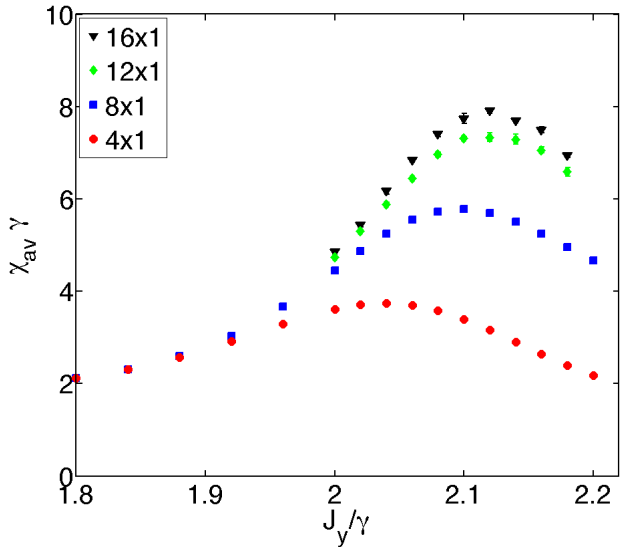

Figure 4.9: Angularly averaged susceptibility χ_{av}(Eq. (4.11)) as a function of J_y, for different lattice sizes, the other parameters are are $J_x = 1.8\gamma$ and $J_z = 2\gamma$. When not shown, the error bars are smaller than the symbols. All the simulations were done with periodic boundary conditions.

to the decay can be extracted by fitting the dynamics with:

$$\langle\hat{\sigma}^x(t)\rangle = \langle\hat{\sigma}^x\rangle_{SS} + Ae^{-\lambda t}, \tag{4.19}$$

where A is a constant depending on the parameters.

In Fig. 4.8, we represent the values of Liouvillian gap across the critical region for different lattice sizes. The results show an important dip around the critical point ($J_y \simeq 1.07$). When the size of the lattice is increased, the dip is getting more pronounced. This is consistent with a critical behaviour. Since we were unable to evaluate the dynamics for lattices bigger than 4×4, it is not yet possible to estimate the critical exponent of the Liouvillian gap at the transition [136].

4.3 Comparison with one dimensional lattices

A previous study [52] found that the phase transition does not survive in one dimensional arrays and that it is replaced by a crossover. Instead of a power-law divergence, the peaks at the transition should saturate. This is confirmed by the numerical results presented in Figs. 4.9 and 4.10 representing respectively the averaged magnetic susceptibility and the Liouvillian gap [136].

In Fig. 4.9, the averaged susceptibility χ_{av} is shown as a function of J_y close to the critical point, for lattice sizes going from 4×1 to 16×1. Even though we see that a peak appears and get more pronounced for small lattice sizes (up to 12×1) it saturates

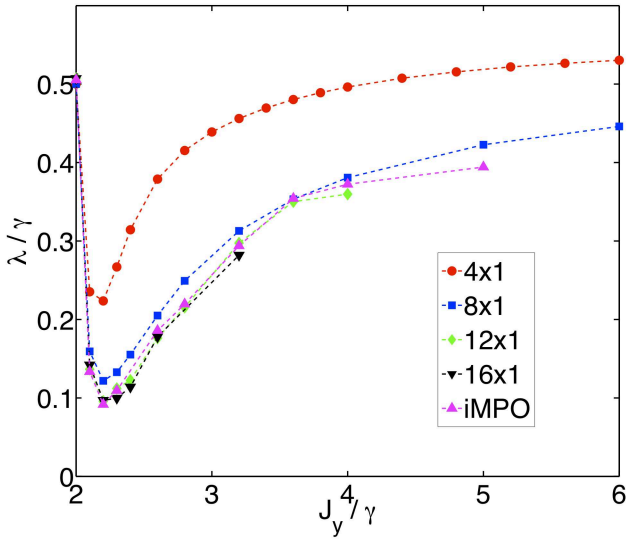

Figure 4.10: Liouvillian gap λ normalized by γ as a function of the normalized coupling J_y/γ across the critical region, for different 1D lattice sizes and infinite lattices (obtained with an iMPO algorithm). The other parameters are $J_x = 1.8\gamma$ and $J_z = 2\gamma$. The simulations were done in the full Hilbert space with periodic boundary conditions except for the infinite lattice. From Ref. [136]

between 12×1 and 16×1. This is a signature of the absence of criticality in the averaged susceptibility for 1D lattices.

Figure 4.10 shows the Liouvillian gap λ as a function J_y for different lattice sizes (from 4×1 to 16×1) and for infinite lattices using an iMPO method [137]. As for Fig. 4.9, we observe that the dip is increasing for small lattice sizes but saturates to the values obtained for an infinite lattice when the number of cavities $N > 12$. This means that the Liouvillian gap is not closing in the thermodynamic limit. Hence, there is no phase transition in one dimension for the XYZ model, just a crossover.

4.4 Conclusion

In this chapter, we have theoretically explored a genuine disspative phase transition in a two-dimensional spin lattice system described by an anisotropic XYZ model. In section 4.2, we have demonstrated that a critical behaviour emerges in two-dimensional lattices by using the corner-space renormalization method. The finite-size scaling analysis of the magnetic susceptibility provided an evaluation of the corresponding critical exponent.

This work also shows that dissipative phase transition share properties of both thermal and quantum phase transitions. Indeed, we have demonstrated that the von Neumann entropy sharply increases across the transition, as it happens in thermal phase transitions. Furthermore, the crucial role of quantum correlations, as witnessed by the

negativity and the Quantum Fisher information, is a signature of the quantum nature of the system.

In the section 4.3, we confirmed the role of dimensionality in the dissipative phase transition under study. Indeed, we have shown that in one dimension, the characteristic power-law divergence is replaced by a saturation.

An interesting development is the study of different entanglement witnesses to see how their critical properties may change. Moreover, the study of other physical models with different symmetries is an intriguing perspective.

Chapter 5

Dissipative phase transitions in incoherently pumped Bose-Hubbard lattices

Interacting many-body systems can exhibit interesting collective behaviours whose peculiar features differ from what is usually observed in equilibrium situations. In order to explore these new phases, the high level of control provided by photonic-based quantum simulators [30, 138] is a powerful tool. The complex dynamics of such systems is governed by the competition between the Hamiltonian evolution, the (coherent or incoherent) drive and the unavoidable photon losses. As a result, the scenario is considerably enriched and the nonequilibrium nature of these platform emerges in different aspects, ranging from their dynamical response [139] and transport properties [140, 141] to their steady-state behaviour [142, 47, 50].

In this chapter, we study the steady-state phases of incoherently pumped Bose-Hubbard lattices. After introducing the model, we will recall some of the main results obtained for a single site [143]. In particular, we show that the photon injection mediated by the two-level system is equivalent to a non-Markovian pump able to stabilize n-photon Fock states in the cavity.

After the single-site treatment, we will present our results on the steady-state phase diagram for a lattice of coupled cavities via a Gutzwiller ansatz for the system density matrix. This analysis shows that for a hopping rate above a critical value, the system undergoes a second-order phase transition associated with the breaking of the $U(1)$ symmetry.

Next to the mean-field predictions, we will show a finite-size analysis of one-dimensional lattices obtained with both the Matrix Product Operators and the corner-space renormalization method.

This work hove been done in collaboration with Alberto Biella and José Lebreuilly under the direction of Davide Rossini, Rozario Fazio, Iacopo Carusotto and Cristiano Ciuti. The main results have been published in *Physical Review A* [125]. Within that

collaboration, another study of a slightly different system exploiting a non-Markovian bath was done, whose results can be found in Ref. [144]. In particular, we found that using a tailored square emission spectrum it is possible to cool down the photonic many-body system into a ground-state-like steady state with a tunable effective chemical potential. This allowed us to exhibit and characterize numerically a phase transition between n-photon Mott-Insulator-like phases and a superfluid-like phase.

5.1 Description of the model

We consider here the following single-site Hamiltonian [143]:

$$\hat{H}_i^{\text{site}} = \omega_c \hat{a}_i^\dagger \hat{a}_i + U \hat{a}_i^\dagger \hat{a}_i^\dagger \hat{a}_i \hat{a}_i + \Omega_R (\hat{a}_i \hat{\sigma}_i^+ + \hat{\sigma}_i^- \hat{a}_i^\dagger) + \omega_{at} \hat{\sigma}_i^+ \hat{\sigma}_i^-, \tag{5.1}$$

where $\hat{a}_i$ is the annihilation operator of the photonic mode on the ith site, $\hat{\sigma}_i^\pm$ are the Pauli ladder operators of the two-level system of frequency ω_{at} . The photonic cavity has a bare frequency ω_c and U quantifies the Kerr nonlinearity. The two-level system and the photonic modes are interacting through a Rabi coupling of frequency Ω_R. The coupling with the environment is described by three Lindblad superoperators taking into account for the losses of the photonic mode:

$$L_{phot}^i[\hat{\rho}] = \frac{\Gamma_l}{2} \left(2\hat{a}_i \hat{\rho} \hat{a}_i^\dagger - \hat{\rho} \hat{a}_i^\dagger \hat{a}_i - \hat{a}_i^\dagger \hat{a}_i \hat{\rho} \right), \tag{5.2}$$

the losses of the two level system,

$$L_{losses}^i[\hat{\rho}] = \frac{\gamma}{2} \left(2\hat{\sigma}_i^- \hat{\rho} \hat{\sigma}_i^+ - \hat{\rho} \hat{\sigma}_i^+ \hat{\sigma}_i^- - \hat{\sigma}_i^+ \hat{\sigma}_i^- \hat{\rho} \right), \tag{5.3}$$

and the two-level system incoherent pumping,

$$L_{pump}^i[\hat{\rho}] = \frac{\Gamma_p}{2} \left(2\hat{\sigma}_i^+ \hat{\rho} \hat{\sigma}_i^- - \hat{\rho} \hat{\sigma}_i^- \hat{\sigma}_i^+ - \hat{\sigma}_i^- \hat{\sigma}_i^+ \hat{\rho} \right). \tag{5.4}$$

As a result, the single-site master equation:

$$\partial_t \hat{\rho}_i = -\mathrm{i} \left[\hat{H}_i^{\text{site}}, \hat{\rho}_i \right] + L_{phot}^i[\hat{\rho}_i] + L_{losses}^i[\hat{\rho}_i] + L_{pump}^i[\hat{\rho}_i] \tag{5.5}$$

is invariant under the transformation:

$$\hat{a}_i \to \hat{a}_i e^{\mathrm{i}\theta}, \tag{5.6}$$

$$\hat{\sigma}_i^- \to \hat{\sigma}_i^- e^{\mathrm{i}\theta}. \tag{5.7}$$

The $U(1)$ symmetry of the Hamiltonian is preserved by the incoherent drive. In order to have a better understanding of the steady-state physics resulting from the interplay of the incoherent pump scheme with the non-linear photonic resonator, the next section is dedicated to a brief review of the single-site phenomenology.

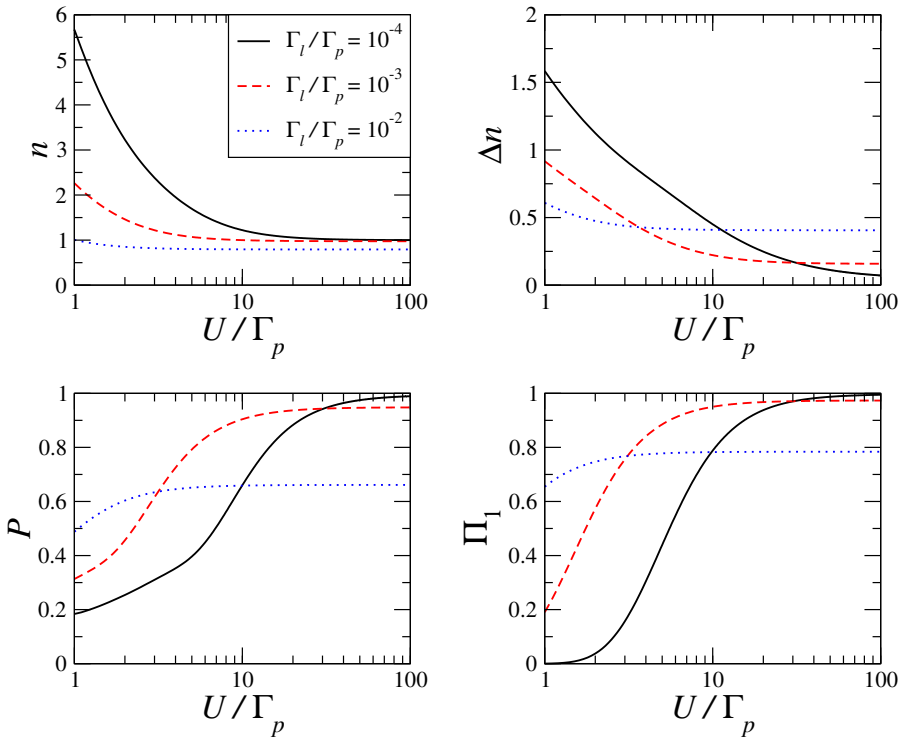

Figure 5.1: Steady-state observables for a single-cavity system. The steady-state value of the photon number n, photon number fluctuations Δn, purity $\mathcal{P}$ and one-photon Fock state population Π_1 are plotted as a function of the nonlinearity U/Γ_p for different values of the cavity dissipation rate Γ_l/Γ_p, as indicated in the legend. The other parameters are $\omega_{at} = \omega_c$, $\Omega_R/\Gamma_p = 10^{-1}$ and $\gamma/\Gamma_p = 10^{-4}$.

5.1.1 Single-site physics

In this section we analyze the physics of a single resonator. In particular, we will show that, by properly exploiting the incoherent driving scheme, it is possible to stabilize single-photon states in the steady state with arbitrary accuracy.

The eigenvalues of the single-site Hamiltonian are

$$\omega_N = N\omega_c + N(N-1)U, \tag{5.8}$$

with N being the number of photons in the cavity. This implies that the transition frequency between the N photon state and the $N+1$ photon state is $\omega_{N,N+1} = \omega_c + 2NU$. By tuning the atomic frequency, we can selectively drive the $N \to N+1$ transition. Moreover, no coherence between the Fock number states $|n\rangle$ is introduced by the drive. Hence, the steady state will be a mixture of Fock number states dominated by the $|N+1\rangle$ state. To do so, we impose parameters so that the emission rate inside the cavity is important but only one photonic transition is pumped, namely:

$$\frac{\Gamma_{em}}{\Gamma} \gg 1, \quad \frac{\Gamma_{em}\Gamma_p^2}{\Gamma_l U} \ll 1 \tag{5.9}$$

with $\Gamma_{em} = 4\Omega_R^2/\Gamma_p$. In this limit, the pumped transition is dominated by the drive and the other transitions are dominated by the dissipation processes. That way, by tuning the parameters, we can selectively populate the Fock state $|1\rangle$. The details on the computation of the different state populations are not discussed here but can be found in Ref. [143].

In the case of hard-core bosons ($U/\Gamma_l \to \infty$), we can solve the master equation (5.5) analytically and find the exact steady state. This allows us to compute the number of photons on resonance ($\omega_{at} = \omega_c$):

$$n = \frac{4\Gamma_p\Omega_r^2}{(\Gamma_l + \gamma + \Gamma_p)(\Gamma_l(\Gamma_p + \gamma) + 4\Omega_r^2)}. \tag{5.10}$$

Expanding Eq.(5.10) for a small effective loss/gain ratio $\eta = \Gamma_l/\Gamma_{em}$ we obtain

$$n = \frac{\Gamma_p}{\Gamma_p + \gamma + \Gamma_l} - \frac{\Gamma_p + \gamma}{\Gamma_p + \Gamma_l + \gamma}\eta + \mathcal{O}(\eta^2). \tag{5.11}$$

We numerically checked the 1-photon Fock state selection by solving the single-cavity master equation via diagonalization of the corresponding Liouvillian. In the following we will work in units of Γ_p. In Fig. 5.1 we show the steady-state value of the photon density $n = \langle \hat{a}^\dagger \hat{a} \rangle$ (where $\langle \hat{O} \rangle = \mathrm{Tr}[\rho^{SS}\hat{O}]$ and $\mathrm{Tr}[\rho^{SS}] = 1$) and its variance Δn as a function of U/Γ_p for different values of the cavity dissipation rate Γ_l/Γ_p. Moreover, we also show the purity of the density matrix $\mathcal{P} = \mathrm{Tr}[(\rho^{SS})^2]$ and the population $\Pi_1 = \langle 1,\uparrow | \rho^{SS} | 1,\uparrow \rangle$, where $|1,\uparrow\rangle$ denotes the state with one photon in the cavity mode and the two-level system into its excited state. As highlighted in the right bottom panel of Fig. 5.1, it is possible to prepare the desired Fock state with arbitrary precision for large enough nonlinearity and small photon leakage rate.

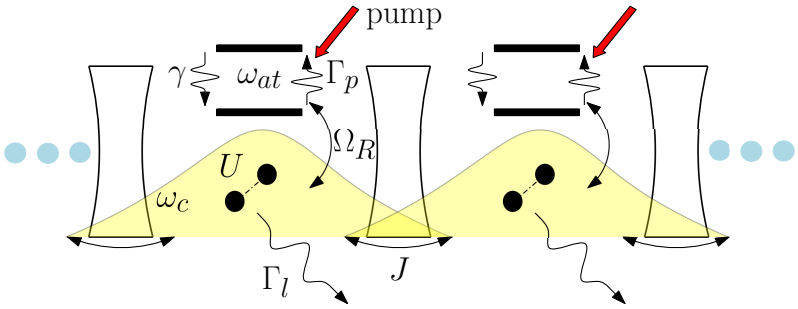

Figure 5.2: A sketch of the considered photonic system, consisting of a lattice of coupled nonlinear cavities. Each lattice site is a cavity coupled to a two-level system, which is incoherently pumped at a rate Γ_p. Ω_R is the coherent coupling rate (vacuum Rabi frequency) between the cavity mode and the two-level emitter, while U is the photon-photon Kerr on-site interaction. The coupling with the environment produces incoherent photon leakage and atomic relaxation at a rate Γ_l and γ respectively. Photons can hop between neighbouring sites at a rate J.

5.2 Gutzwiller mean-field theory

In the following, we focus on the physics in a lattice where nearest-neighbour sites are coupled via a hopping interaction

$$\hat{H}_{hop} = -J \sum_{<i,j>} \hat{a}_i^\dagger \hat{a}_j, \tag{5.12}$$

where J is the hopping rate between. The system is described by the master equation:

$$\partial_t \hat{\rho} = -\mathrm{i}[\hat{H}, \hat{\rho}] + \sum_{i=1}^{N_{\text{sites}}} \left(L^i_{ph} + L^i_{losses} + L^i_{pump} \right), \tag{5.13}$$

where $\hat{H} = \sum_{i=1}^{N_{\text{sites}}} \hat{H}_i - J \sum_{<i,j>} \hat{a}_i^\dagger \hat{a}_j$ and $\hat{H}_i$ is the single-site Hamiltonian given in Eq. (5.1). As we have seen in the previous section, the single-site Hamiltonian and the different Lindblad super-operators can stabilize a Fock state with one photon in each cavity. We are interested in the effects of the competition between the photon hopping and the on-site interactions. The full system is summarized in Fig. 5.2.

Note that the hopping Hamiltonian (5.12) is invariant with respect to the global gauge transformation (5.6). As a result, the master equation of the complete system (5.13) preserves the $U(1)$ symmetry.

The first step of our study is to perform a Gutzwiller mean-field analysis of the steady-state phase diagram. In this framework, the exact lattice dynamics is reduced to the self-consistent evolution of local density matrices.

5.2.1 Gutzwiller ansatz

The Gutzwiller mean-field approximation assumes a factorized ansatz for the global density matrix

$$\hat{\rho} \simeq \bigotimes_{i=1}^{N_{\text{sites}}} \hat{\rho}_i, \tag{5.14}$$

where $\hat{\rho}_i$ is the density matrix of the ith site. If we plug the ansatz (5.14) into the master equation (5.13) and trace out all sites but the ith, the coupling term can be written as:

$$-J \sum_{<i,j>} \hat{a}_i^\dagger \hat{a}_j \longrightarrow -J \sum_{j \in \text{N.N.}} (\hat{a}_i^\dagger \langle \hat{a}_j \rangle + \langle \hat{a}_j^\dagger \rangle \hat{a}_i), \tag{5.15}$$

where we sum only on the nearest neighbours site of the ith ($j \in$ N.N) and $\langle \hat{o}_j \rangle = \text{Tr}(\hat{o}_j \hat{\rho}_j)$. If we are interested in spatially homogeneous phases, we assume that $\forall i,\ \hat{\rho}_i = \hat{\rho}_{\text{MF}}$. Under that assumption, the coupling term becomes:

$$-zJ(\hat{a}^\dagger \langle \hat{a} \rangle + \hat{a} \langle \hat{a} \rangle^*), \tag{5.16}$$

where we dropped the site indexes as they are no longer relevant. The coordination number z is the number of nearest neighbours. Therefore, we can write a master-equation for the local mean-field density matrix, namely

$$\begin{aligned} \partial_t \hat{\rho}_{\text{MF}} = &- \text{i}[\hat{H}_{\text{site}} - zJ(\hat{a}^\dagger \langle \hat{a} \rangle + \hat{a} \langle \hat{a} \rangle^*), \hat{\rho}_{\text{MF}}] \\ &+ L_{phot}\left[\hat{\rho}_{MF}\right] + L_{losses}\left[\hat{\rho}_{MF}\right] + L_{pump}\left[\hat{\rho}_{MF}\right], \end{aligned} \tag{5.17}$$

where the Lindblad super-operators are defined in Eqs. (5.2), (5.3) and (5.4). It is important to note that the term propotional to $\langle \hat{a} \rangle = \text{Tr}(\hat{a} \hat{\rho}_{\text{MF}})$ makes the master equation non-linear with respect to the density operator. The trace $\text{Tr}(\hat{a} \hat{\rho}_{\text{MF}})$ has to be computed at each time step and reintroduced in the master equation to solve it self-consistently in time.

5.2.2 Phase diagram for hard-core bosons

Firstly, we applied the Gutzwiller theory of the previous section for the hard-core boson case ($U/\Gamma_l \to \infty$). In this regime, each site can be populated with at most one photon. In particular, the dynamic of the coherence $|\langle \hat{a} \rangle|$ plotted in Fig. 5.3 shows the emergence of a limit cycle at long times for the parameters $\omega_{at} - \omega_c = -zJ$, $zJ = 2.5\Gamma_p$, $\Gamma_l = \gamma = 10^{-3}\Gamma_p$. Starting from an initial state where $|\langle \hat{a} \rangle| \neq 0$, the coherence evolves in the long time limit as $|\langle \hat{a} \rangle| \exp(\text{i}\omega_L t)$, with $|\langle \hat{a} \rangle| \neq 0$ where ω_L depends on the system parameters. This means that the $U(1)$ symmetry is broken by the nearest-neighbour coupling.

In the left panel of Fig. 5.4, we plotted the amplitude of the limit cycles in the steady-state $|\langle \hat{a} \rangle|$ as a function of the nearest-neighbour hopping rate. As before, we start the integration of the master equation (5.5) with an initial state where $|\langle \hat{a} \rangle| \neq 0$. When the hopping rate is below a critical value J_c, $|\langle \hat{a} \rangle| = 0$ in the steady-state. At

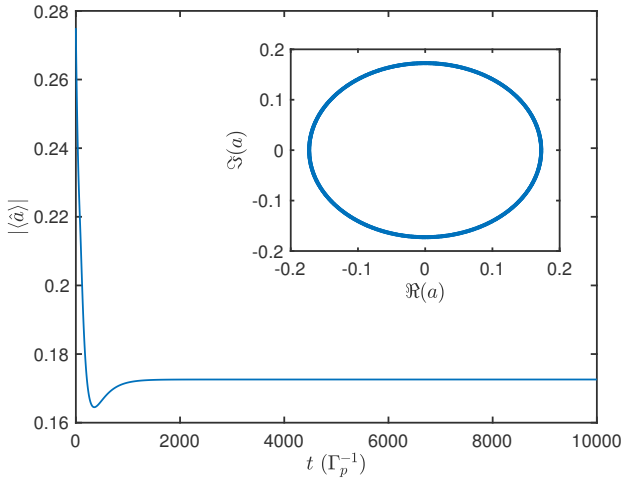

Figure 5.3: Time evolution of the coherence $|\langle\hat{a}\rangle|$ within the Gutzwiller mean-field approximation. Starting from a non-zero value, the system converges to a state with $|\langle\hat{a}\rangle| \neq 0$. The inset shows the imaginary part of $\langle\hat{a}\rangle$ as a function of its real part. We do not obtain a steady-state but a limit cycle where $\langle\hat{a}\rangle = |\langle\hat{a}\rangle| \exp(-\mathrm{i}\omega_L t)$, with ω_L depending on the parameters. Parameters: $\omega_{at} - \omega_c = -zJ$, $zJ = 2.5\Gamma_p$, $U = \infty$, $\Gamma_l = \gamma = 10^{-3}\Gamma_p$.

$J = J_c$, a second order phase transition takes place and for $J > J_c$ the system enters a coherent delocalized phase characterized by the emergence of limit cycles.

The right panel of Fig. 5.4 shows the number of photons n, the variance Δn and the compressibility $\mathcal{K} = \Delta n^2/n$ in the steady state as a function of zJ. For $J < J_c$, the number of photons is close to 1 and the variance is close to 0. By construction, a vanishing value of the mean-field order parameter implies that $\hat{\rho}_{SS}$ is the steady-state solution of the master equation for a single cavity. However, in the exact model, the short-range coupling induced by the photon hopping may play an important role that is neglected since $|\langle\hat{a}\rangle| = 0$ is equivalent to $J = 0$ within the Gutzwiller ansatz. Consequently, in order to characterize the phase with the unbroken symmetry it is necessary to go beyond the mean-field theory. This will be done in section 5.3 where we show that in a range of zJ/Γ_p compatible with the Gutzwiller prediction the number of photons remains very close to one with very small fluctuations.

This Mott-like phase, is also characterized by an (almost) vanishing compressibility $\mathcal{K}$, analogously to what happens in the equilibrium situations. This indicates that the phase is incompressible, the density matrix being close to $|1\rangle\langle 1|$. This is confirmed by Fig. 5.5 that shows the purity $\mathrm{Tr}(\hat{\rho}_{MF}^2)$ of the steady-state density matrix as a function of the coupling zJ. The purity is a measure of the distance of the density operator to a pure state. If the density operator is a pure state, $\mathrm{Tr}(\hat{\rho}_{MF}^2) = 1$, otherwise $\mathrm{Tr}(\hat{\rho}_{MF}^2) < 1$. In the incompressible phase, the state is almost pure, on the contrary in the symmetry-broken phase, the purity decreases showing that the state becomes much more mixed.

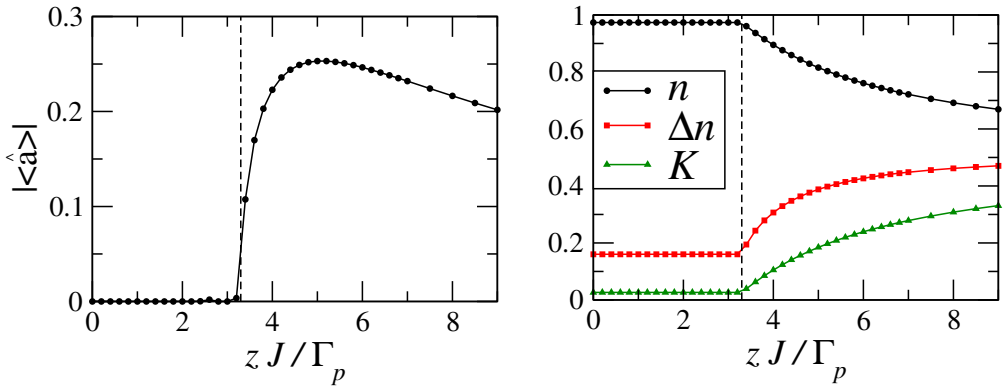

Figure 5.4: The order parameter $|\langle\hat{a}\rangle|$ (left panel), the number of photons n, its variance Δn and the compressibility $\mathcal{K}$ (right panel) of the steady-state of Eq. (5.17) as a function of zJ/Γ_p in the hard-core limit ($U/J = +\infty$). Here $\Gamma_l/\Gamma_p = \gamma/\Gamma_p = 10^{-3}$, $\Omega_R/\Gamma_p = 10^{-1}$, $U/\Gamma_p = 10^2$ and $\omega_{at} = \omega_c$. The dashed vertical line signals the predicted critical value of J.

Similarly, the number of photons decreases and in the $zJ \to \infty$ limit goes to 0.5. The fluctuations Δn and the compressibility increases to finite values in the coherent phase.

It is worth noting that in contrast to the Mott-Insulator to superfluid transition at equilibrium, in our case, the state is mixed in the coherent phase. In order to grasp further information about the nature of the steady-state density matrix in the two phases, in Fig. 5.6 we plot the Wigner function of the photonic reduced density matrix:

$$W(\alpha) = \frac{2}{\pi}\mathrm{Tr}\left[\hat{\rho}^{ph}_{\mathrm{SS}}\hat{D}(\alpha)e^{\mathrm{i}\pi\hat{a}^\dagger\hat{a}}\hat{D}^\dagger(\alpha)\right], \tag{5.18}$$

with $\rho^{ph}_{\mathrm{SS}} = \mathrm{Tr}_{at}(\hat{\rho}_{\mathrm{SS}})$ being the reduced photonic density matrix. $\hat{D}(\alpha)$ denotes the displacement operator $\hat{D}(\alpha) = \exp(\alpha\hat{a}^\dagger - \alpha^*\hat{a})$.

The left panel of Fig. 5.6 represents the Wigner function for $zJ/\Gamma_p = 0$, deep in the incompressible phase. It is symmetric for rotations with respect to $\alpha = 0$ (which implies that $|\langle\hat{a}\rangle| = 0$) and shows a negative dip at $\alpha = 0$. It is very close to the Wigner function of a 1-photon Fock state $|1\rangle$. The right panel shows the Wigner function deep in the symmetry broken phase ($zJ/\Gamma_p = 4$). In this case, there is still a negative dip but $W(\alpha)$ loses its rotational symmetry as a result of the $U(1)$ symmetry breaking.

Figure 5.7 shows the amplitude of the limit cycle as a function of the the coupling strength zJ/Γ_p for multiple values of the detuning between the frequency of the atom and the one of the cavity. The frequency of the $\vec{k} = 0$ mode of the lattice is $\omega_c - zJ$. Hence, for a detuning $\omega_c - \omega_{at} = -zJ$, we expect that the pumping of the spatially homogeneous phase is the most efficient. Indeed, the numerical results shown on Fig.5.7, confirm that the detuning value $\omega_c - \omega_{at} = -zJ$ is optimal to get a large value of the order parameter in a wide range of J.

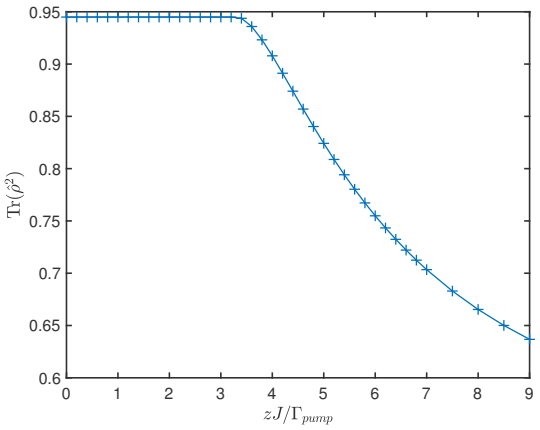

Figure 5.5: The purity $\mathrm{Tr}(\hat{\rho}^2)$ of the steady-state density matrix obtained via integration of Eq. (5.17) as a function of zJ/Γ_p. The other parameters are the same as in Fig. 5.4.

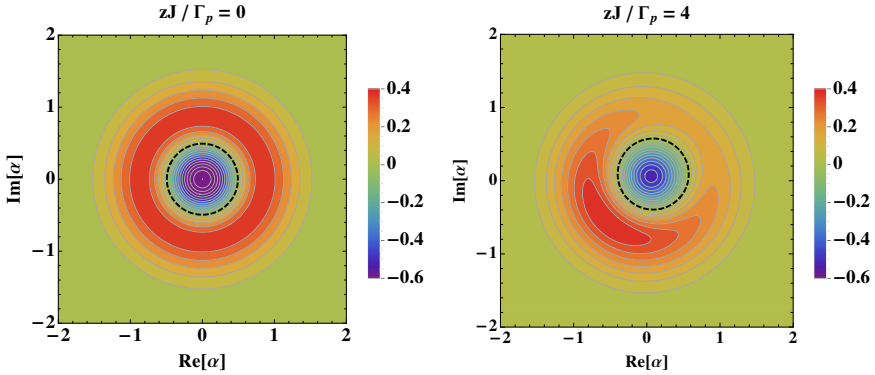

Figure 5.6: Contour plot of the steady-state Wigner distribution $W(\alpha)$ in the Mott-like (left panel) and coherent phases (right panel). Each contour denotes a variation of 0.05 of the value of $W(\alpha)$. The black dashed contour includes the region with $W(\alpha) < 0$. The parameters are set as in Fig. 5.4.

It is worth stressing that the observed transition is not driven by the competition between the hopping and interaction terms. In a one-dimensional chain or a two-dimensional square lattice, the width of the photonic band is $2zJ$. When the band is larger than the width of the Lorentzian emission spectrum, photons are not efficiently pumped in the lattice and the population starts to decrease. At some point the number of photons is not commensurate with the number of sites and when there is a significant number of empty sites, photons can move in the lattice and long-distance coherence starts to build up. This kind of phase transition driven by commensurability between the number of particle and the number of sites have also been proposed for the equilibrium Bose-Hubbard lattice with hard-core bosons [145] in two dimensions.

Based on this argument we can estimate the critical J_c for which the Mott-like phase becomes unstable. In our case, the Lorentzian shaped emission spectrum of the two-level

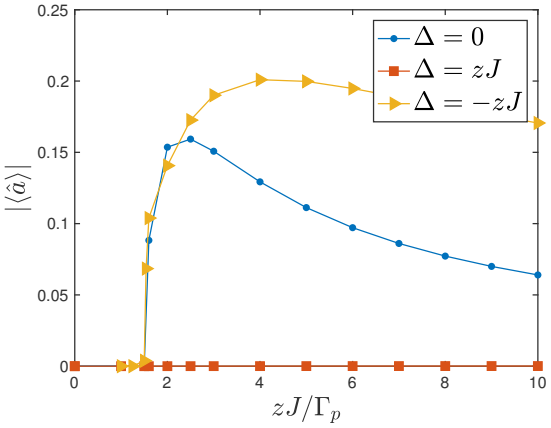

Figure 5.7: The amplitude of the order parameter $|\langle \hat{a} \rangle|$ in the steady-state as a function of zJ/Γ_p for three values of the detuning $\Delta = \omega_{at} - \omega_c$. The other parameters are set as in Fig. 5.4.

system is given by:

$$\Gamma_{em}(\delta) = \Gamma_{em} \frac{(\Gamma_p/2)^2}{\delta^2 + (\Gamma_p/2)^2} \tag{5.19}$$

with δ being the detuning between frequency of the two-level system and the photonic mode. Hence, in order to obtain the condition for the critical coupling, we equal the effective emission for $\delta = \omega_c - zJ_c - \omega_{at}$ with the photon losses:

$$\Gamma_{em} \frac{(\Gamma_p/2)^2}{(\omega_{at} - \omega_c + zJ_c)^2 + (\Gamma_p/2)^2} = \Gamma_l. \tag{5.20}$$

In the regime where the effective pumping dominates over the photon losses, that is

$$\frac{\Gamma_{em}}{\Gamma_l} = \frac{4\Omega_R^2}{\Gamma_l \Gamma_p} \gg 1, \tag{5.21}$$

the critical coupling at resonance ($\omega_{at} = \omega_c$) reads:

$$zJ_c \simeq \sqrt{\frac{\Gamma_p}{\gamma}} \Omega_R. \tag{5.22}$$

For hard-core bosons, we can formulate a mean-field set of equation, in the same way as in subsection 5.1.1. This set of equations can be solved in the case $|\langle \hat{a} \rangle| = 0$ and the stability of the solution can be checked using a Bogoliubov analysis on the density operator [110, 52].

In Fig. 5.8 we show the phase diagram in all the parameter space obtained using the stability analysis for the symmetry-conserving phase. The dashed lines denote the threshold $\Gamma_{em}^0/\Gamma_l > 1$ (see Eq. (5.21)). The continuous lines represent the scaling law that is given in Eq. (5.22). As expected, such scaling law becomes exact in the strong pumping limit (5.21).

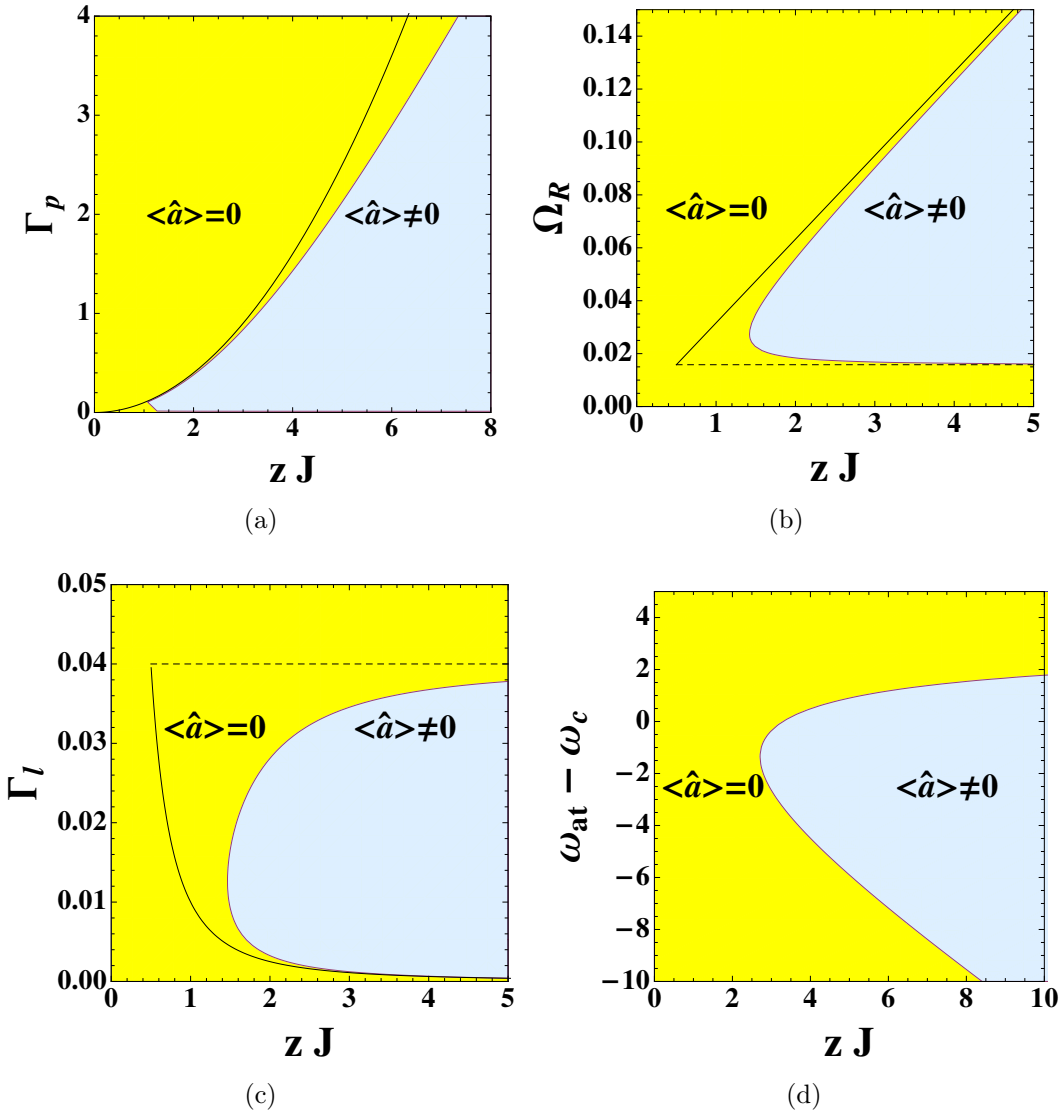

Figure 5.8: Results of the mean-field stability analysis. The yellow area denotes the region where $\langle \hat{a} \rangle = 0$ is stable, while the gray area is the region where the solution $\langle \hat{a} \rangle = 0$ is unstable and the symmetry is broken. The solid lines are the predictions for the critical hopping rate given by Eq. (5.22) which well approximates the phase boundary in the $\Gamma^0_{em}/\Gamma_l \gg 1$ limit (see Eq. (5.21)). The dashed vertical lines denotes $\Gamma^0_{em}/\Gamma_l = 1$. The condition $\Gamma^0_{em}/\Gamma_l > 1$ is necessary in order to have a significant population in the symmetry broken phase.

5.2.3 $J - U$ phase diagram

In order to complete the study, we relaxed the hard-core bosons constraint ($U/\Gamma_l < +\infty$). In this case, the problem has too many degrees of freedom and the stability analysis applied in the hard-core limit is no longer feasible. Therefore, the critical value J_c was obtained by numerically integrating Eq. (5.17) for different values of U and zJ.

Figure 5.9 shows the phase diagram in the $U - J$ plane. For each value of U/Γ_p and

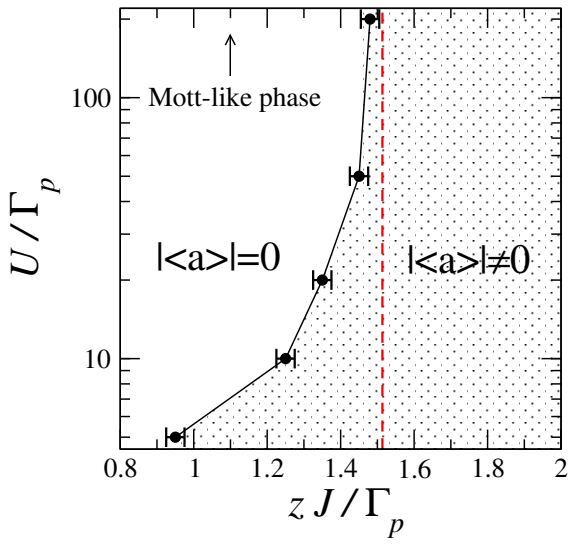

Figure 5.9: Mean-field steady-state phase diagram in the $U/\Gamma_p - zJ/\Gamma_p$ plane. The white area corresponds to the region of the parameters for which $|\langle\hat{a}\rangle| = 0$ while in the shaded region the $U(1)$ symmetry is spontaneously broken and the steady-state exhibits limit-cycle ($|\langle\hat{a}\rangle| \neq 0$). Here $\gamma/\Gamma_p = \Gamma_l/\Gamma_p = 10^{-2}$, $\Omega_R/\Gamma_p = 10^{-1}$ and $\omega_{at} = \omega_c$.

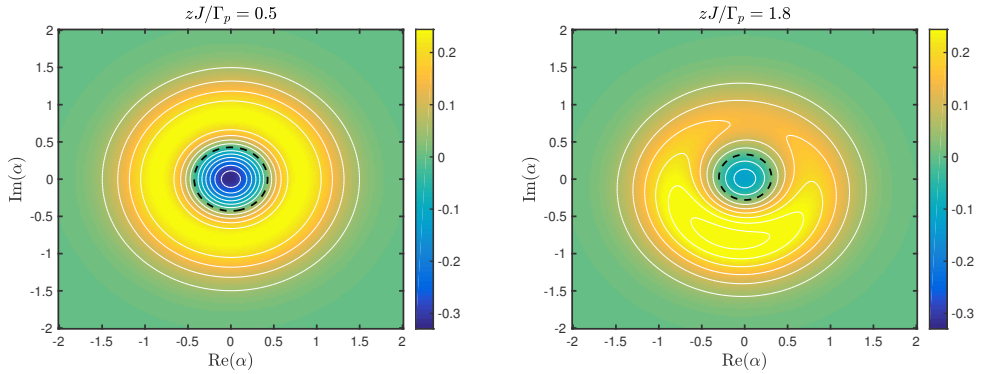

Figure 5.10: Contour plot of the steady-state Wigner distribution $W(\alpha)$ on the Mott-like (left panel) and in the symmetry-broken phase (right panel) in the soft-core boson case ($U = 5\Gamma_p$). The contours denotes variations of 0.05 in the value of $W(\alpha)$. The black dashed contour encircles the regions where $W(\alpha) < 0$. All the other parameters are the same as in Fig. 5.9.

zJ/Γ_p, we computed the coherence in the steady state and found the critical value J_c for which $|\langle\hat{a}\rangle|$ goes from 0 to a finite value in the steady state. The red dashed line represents the transition for $U/\Gamma_l = +\infty$.

The white area corresponds to the Mott-like phase where the coherence is vanishing. Note that there is one photon per cavity and the purity is close to 1. The shaded area corresponds to the symmetry-broken phase. This phase digram shows that the transition survives for finite values of U.

In order to compare the density matrix for $U/\Gamma_p = 5$ with the hard-core case, the contour plots of the steady-state Wigner distributions are plotted on Fig. 5.10. The Wigner functions are very similar to those of the hard-core bosons case shown in Fig. 5.6. Hence, at the mean-field level, the symmetry-conserving and the symmetry-broken phases have similar features for hard-core and soft-core bosons. A notable difference is that in the soft-core bosons case, the negative part of the Wigner function (in both phases) is significatively reduced.

Note that when U is decreased, the selective population of the state $|1\rangle$ is reduced as other states start to be significantly excited in accordance to the selection rule detailed in section 5.1.1. As a result, the photonic part of the density matrix becomes less similar to the one of a single-photon Fock state in this regime.

5.3 Beyond the Gutzwiller approximation

In this section, we go beyond the Gutzwiller approximation employed so far. Numerically, the problem becomes particularly challenging because of the different timescales involved, which differ by several orders of magnitude. In particular, the two-level and cavity dissipation rates are much smaller than the incoherent drive ($\gamma, \Gamma_l \ll \Gamma_p$). In order to compute the steady state $\hat{\rho}_{\rm SS}$ of the complete master equation , we used two different methods: the corner-space renormalization method (Chapter 3) and a matrix product operator (MPO) algorithm [14, 15].

The MPO approach enabled us to investigate arrays of up to 20 sites. However, it failed to explore the regime where long-range correlations develop (convergence with respect to the bond link dimension was not achieved). Therefore, we used the MPO method only to explore the nature of the localized Mott-like phase.

The corner-space renormalization method was instead able to converge in the region where the mean-field theory predicts a phase transition. Moreover, since it computes the density matrix and the corresponding probability spectrum, it is particularly adequate to calculate the von Neumann entropy, albeit for a reduced size (we were able to simulate arrays of up to 8 cavities with full convergence).

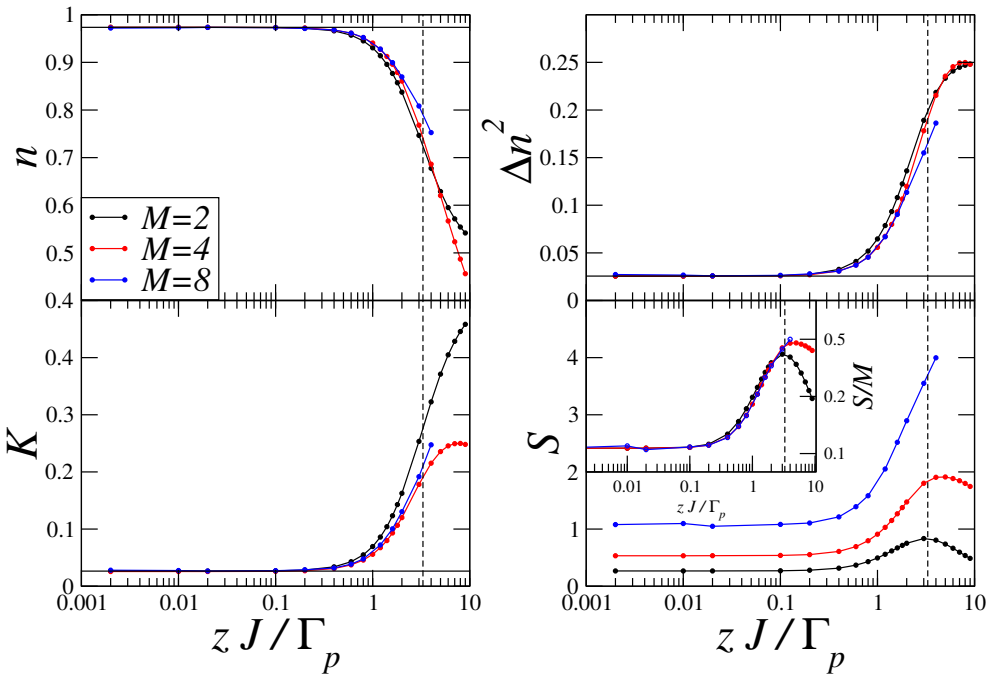

Figure 5.11: Top panels: the average photon density n in the steady-state (left panel) and its variance Δn^2 (right panel) as a function of zJ/Γ_p. Bottom panels: steady-state value of the compressibility $\mathcal{K}$ (left panel) and of the entropy (right panel) as a function of zJ/Γ_p in the hard-core limit ($U/J = +\infty$). The various curves are for different sizes, as indicated in the legend. The solid horizontal lines are the single-cavity values ($J = 0$) of the quantity under consideration. The solid vertical lines denote the critical hopping rates predicted by the Gutzwiller mean-field theory. The parameters are set as $\omega_{at} = \omega_c - zJ$, $\Gamma_l/\Gamma_p = \gamma/\Gamma_p = 10^{-3}$, $\Omega_R/\Gamma_p = 10^{-1}$. For the largest size considered (8 sites), the convergence of the considered quantities has been achieved with 3000 states in the corner space (the full Hilbert space has a dimension equal to $4^8 = 65536$).

5.3.1 Crossover in 1D

Figure 5.11 displays the averaged number of photons $n = \sum_{i=1}^{M} \langle \hat{a}_i^\dagger \hat{a}_i \rangle / M$, as well as the fluctuations $\Delta n^2 = \sum_{i=1}^{M} \Delta n_i^2 / M$, the compressibility $\mathcal{K} = \sum_{i=1}^{M} \Delta n_i^2 / (n_i M)$ and the von Neumann entropy S as a function of zJ/Γ_p close to the transition predicted by mean-field (black dashed line). In these calculations, we have slightly shifted the atomic frequency $\omega_{at} = \omega_c - zJ$. As seen in Fig. 5.7, under that condition, the condensation in the $\vec{k} = 0$ mode is favored. This way, we ensure a spatially homogeneous condensation process as assumed in the mean-field calculation. In particular, we avoid the population of pairs of modes with opposite wavevector that would lead to condensate fragmentation effect [146]. This fragmentation mechanism is likely to be the reason why such a small coherence was numerically found in Ref. [147]. Below the critical coupling predicted by mean-field (black dashed line), the data collapse on the single-site prediction. This is in agreement with the mean-field analysis which predicts a region where the local

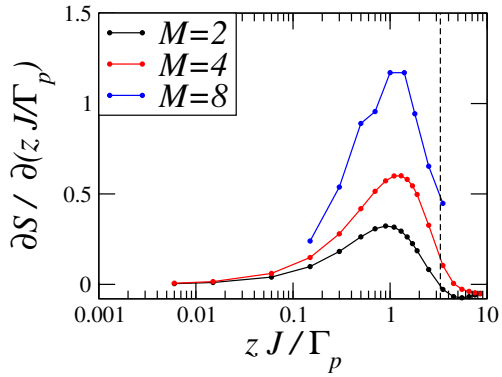

Figure 5.12: Derivative of the entropy with respect to the hopping rate for different system sizes as indicated in the legend. The other parameters are as in Fig. 5.11.

interactions dominate over the cooperative effects. In this Mott-like phase, the photon density is almost integer and the fluctuations are almost vanishing. This implies that in this range, the correlations between the different cavities are very small. This is confirmed by the collapse of the normalized entropy S/M (inset of the bottom right panel of Fig. 5.11).

When the coupling J is increased above the critical value predicted by mean-field, the system enters a completely new regime where the photon density is significantly reduced and the fluctuation are increased. Those characteristics are similar to the one found in the symmetry-broken phase using by the mean-field analysis. Moreover, as expected from the behaviour of the purity at the mean-field level, the entropy quickly increases in this new regime. The main difference is that in 1D the phase transition is replaced by a crossover, which is not surprising considering the low dimensionality.

In section 4.2.2, we showed that the derivative of the entropy can be a meaningful quantity in dissipative phase transitions. In Fig. 5.12, the derivative of the entropy with respect to the coupling strength $\partial S/\partial(zJ/\Gamma_p)$ is plotted as a function of the hopping strength zJ close to the mean-field prediction for the transition (black-dashed line). The maximum of the peak appears to increase when the number of sites in the array grows. However, as it had been predicted in Refs. [148, 149], a crossover is expected in 1D rather than a phase transition.

5.3.2 Correlation length

In second order phase transitions, it is expected that the behaviour of the spatial correlations changes at the transition. In the symmetry conserving phase, the correlations at long distances should fall exponentially. The characteristic length of the exponential should increase when approaching the transition and diverge at the critical point.

Since the MPO algorithm is not able to reach the transition point, we focus here on the build up of the correlations deep in the Mott-like phase. To do so, we study the

two-site first-order correlation function:

$$c(i,j) = \langle \hat{a}_i^\dagger \hat{a}_j \rangle. \tag{5.23}$$

First, we consider a Jordan-Wigner transformation that maps the hard-core bosons in one dimension to fermions, similarly to one-dimensional hard-core boson systems at equilibrium [150, 151]

$$\hat{\rho}_F = \hat{U}\hat{\rho}_B\hat{U}^{-1}, \quad \hat{\rho}_F = \bigotimes_k \hat{\rho}_F^k, \tag{5.24}$$

with $\hat{U}$ being a unitary transformation that anti-symmetrizes the bosonic density matrix $\hat{\rho}_B$. Therefore, the operators are transformed as

$$\hat{a}_j^F = e^{\mathrm{i}\pi \sum_{l<j} \hat{a}_l^\dagger \hat{a}_l} \hat{U} \hat{a}_j^B \hat{U}^{-1}. \tag{5.25}$$

In order to estimate the distribution in k-space for the fermions, we start by estimating it for free bosons following [143, 144]. In this regime, it is possible to define an effective inverse temperature β and a chemical potential μ such that the occupation of a given $\vec{k}$-mode is given by:

$$n_k^B = \frac{1}{e^{\beta(E_k-\mu)} - 1}, \tag{5.26}$$

with E_k being the energy of the $\vec{k}$-mode. They are given by the transition rate between two eigenstates of the photonic part of the Hamiltonian $|f\rangle$ and $|f'\rangle$ with respectively N and $N+1$ photons

$$\frac{T_{f'\to f}}{T_{f\to f'}} = e^{\beta\mu}, \tag{5.27}$$

where the photon loss rate in any mode is given by

$$T_{f'\to f} = \Gamma_l |\langle f|\hat{a}|f'\rangle|^2. \tag{5.28}$$

The gain rate of the mode $\vec{k}$ reads

$$T_{f\to f'} = \Gamma_{em}^0 |\langle f'|\hat{a}^\dagger|f\rangle|^2 \frac{(\Gamma_p/2)^2}{(\omega_{at} - \omega_c + 2J\cos(k))^2 + (\Gamma_p/2)^2}. \tag{5.29}$$

In the limit of small photon hopping ($J \ll \Gamma_p$), we can estimate the effective inverse temperature β:

$$\begin{aligned} T_{f\to f'} &\simeq \Gamma_{em}^0 \frac{(\Gamma_p/2)^2}{\Delta^2 + (\Gamma_p/2)^2} \left(1 - \frac{4J\cos(k)\Delta}{\Delta^2 + (\Gamma_p/2)^2} + O(J^2)\right), \\ &\simeq \Gamma_{em}^0 \frac{(\Gamma_p/2)^2}{\Delta^2 + (\Gamma_p/2)^2} e^{-\beta\Delta}, \end{aligned} \tag{5.30}$$

with

$$\beta = \frac{4J\cos(k)}{\Delta^2 + (\Gamma_p/2)^2}. \tag{5.31}$$

Assuming $J \ll \Gamma_p$, we can approximate $\exp(\beta(E_k - \mu)) \simeq \exp(\beta\mu)$. This gives the boson distribution:

$$n_k^B = \left(\frac{\Gamma_l}{\Gamma_{em}^0} \left[\left(\frac{2\Delta}{\Gamma_p} + \frac{4J\cos k}{\Gamma_p} \right)^2 + 1 \right] - 1 \right)^{-1}. \tag{5.32}$$

This distribution leads to a natural ansatz for the fermionic distribution:

$$n_k^F = \left(\frac{\Gamma_l}{\Gamma_{em}^0} \left[\left(\frac{2\Delta}{\Gamma_p} + \frac{4J\cos k}{\Gamma_p} \right)^2 + 1 \right] + 1 \right).^{-1} \tag{5.33}$$

Using the equation (5.33), we can compute the one-body fermionic correlation function:

$$\begin{aligned} c(j)^F &= \langle \hat{a}_0^F \hat{a}_0^{F\dagger} \rangle, \\ &= \int_{-\pi}^{\pi} \frac{\mathrm{d}k}{2\pi} e^{\mathrm{i}kj} n_k^F. \end{aligned} \tag{5.34}$$

In order to simplify the calculation, let us introduce the complex function:

$$g(z) = \left(\frac{\Gamma_l}{\Gamma_{em}^0} \left[\left(\frac{2\Delta}{\Gamma_p} + z \right)^2 + 1 \right] + 1 \right),^{-1} \tag{5.35}$$

which can be expanded as:

$$g(z) = \sum_n \alpha_n \left(\frac{z}{r_c} \right)^n, \tag{5.36}$$

with $r_c = \sqrt{1 + \Gamma_{em}^0/\Gamma_l + (2\Delta/\Gamma_p)^2}$ being the convergence radius of the power expansion and α_n is a sub-exponential sequence.

If we substitute the expansion (5.36) in the fermionic one-body correlation function (5.34), we get:

$$c(j)^F = \sum_{n \geq j} \alpha_n \left(\frac{4J}{r_c \Gamma_p} \right)^n \int_{-\pi}^{\pi} \frac{\mathrm{d}k}{2\pi} e^{\mathrm{i}kj} \cos(k)^n. \tag{5.37}$$

Since $4J/(r_c\Gamma_p) \ll 1$ we keep only the smallest order of J ($n = j$) in the series expansion

$$\begin{aligned} c(j)^F &\simeq \alpha_j \left(\frac{4J}{r_c \Gamma_p} \right)^j \int_{-\pi}^{\pi} \frac{\mathrm{d}k}{2\pi} e^{\mathrm{i}kj} \cos(k)^j, \\ &= \alpha_j \left(\frac{2J}{r_c \Gamma_p} \right)^j. \end{aligned} \tag{5.38}$$

Assuming that $c(j)^F \propto \exp(-j/\lambda_F)$, we find the following expression for λ_F:

$$\lambda_F = \ln \left(\frac{\Gamma_p \sqrt{1 + \Gamma_{em}^0/\Gamma_l + (2\Delta/\Gamma_p)^2}}{J} \right). \tag{5.39}$$

The next step is to perform the inverse transform and go back to the bosonic system. To do so, we exploit the transformation (5.25):

$$c(j) = \langle \hat{a}_j^B \hat{a}_0^{B\dagger} \rangle = \langle \hat{a}_j^F e^{\mathrm{i}\pi \sum_{l<j} \hat{n}_l} \hat{a}_0^{F\dagger} \rangle. \tag{5.40}$$

Since for a vanishing hopping, the density is homogeneous over the lattice and $n = (\Gamma_l/\Gamma^0_{em} + 1)^{-1}$, we get

$$c(j) \simeq \prod_{l<j} \langle e^{\mathrm{i}\pi\hat{n}_l}\rangle \langle \hat{a}^F_j \hat{a}^{F\dagger}_0\rangle. \tag{5.41}$$

If we consider hard-core particles, using the property $\hat{n}^2 = \hat{n}$, we obtain

$$\langle e^{\mathrm{i}\pi\hat{n}_l}\rangle = \frac{1 - \frac{\Gamma^0_{em}}{\Gamma_l}}{1 + \frac{\Gamma^0_{em}}{\Gamma_l}}. \tag{5.42}$$

In the regime of parameters we are interested in $\Gamma^0_{em}/\Gamma_l > 1$ ($\langle e^{\mathrm{i}\pi\hat{n}_l}\rangle < 0$) which gives

$$c(j) \propto (-1)^j e^{-j/\lambda}, \tag{5.43}$$

with the correlation length:

$$1/\lambda = \ln\left(\left|\frac{1 - \frac{\Gamma^0_{em}}{\Gamma_l}}{1 + \frac{\Gamma^0_{em}}{\Gamma_l}}\right| \frac{\Gamma_p\sqrt{1 + \Gamma^0_{em}/\Gamma_l + (2\Delta/\Gamma_p)^2}}{J}\right). \tag{5.44}$$

In the limit of $J/\Gamma_p \ll 1$ we finally obtain the correlation length:

$$1/\lambda_{ph} \approx \ln(\Gamma_p/J). \tag{5.45}$$

In order to check this scaling law for the correlation length, we used a MPO algorithm to reach dynamically the steady-state for systems of up to 20 cavities in the Mott-like regime. In the right panel of Fig. 5.13, we show the absolute value of $c(i,j)$ since, as Eq. (5.43) clearly shows, it has an alternating sign. By fitting the decay of $|c(i,j)|$ by an exponential, we can obtain the value of λ_{ph} for the different values of J. The right panel of Fig. 5.13 shows the values of the correlation length obtained from the fit. The red line shows the scaling obtained analytically (see Eq. (5.45)). As expected, the characteristic length of the correlation decay increases as zJ/Γ_p is increased.

5.4 Conclusion

In this chapter, we predicted the phases of a driven-dissipative cavity array which is pumped incoherently via two-level systems. Using a Gutzwiller decoupling theory, we determined the non-equilibrium phase diagram of the system. The interplay between the on-site interactions, photon hopping and driven-dissipative processes lead to a second-order dissipative phase transition between a Mott-like phase and a superfluid-like phase where the $U(1)$ symmetry is broken. This transition is driven by commensurability effects. Hence, the critical value of the control parameter can be deduced by comparing the effective emision rate at the band-boundary with the photon loss rate of the cavity.

Furthermore, the incoherent pumping allows the stabilisation of a Mott-like phase with an almost integer photon population and almost vanishing fluctuations. We characterized the transition both in terms of one-body correlations (that indicate the emergence

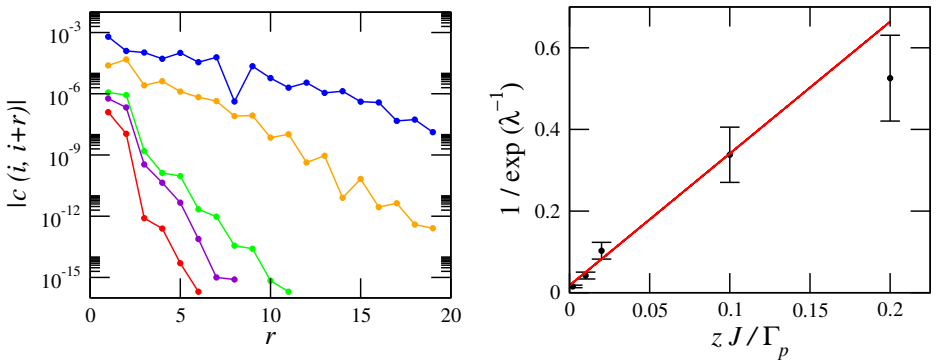

Figure 5.13: Right panel: Spatial decay of the correlation function $c(i, i+r)$ (as defined in Eq. (5.23)) with the distance r for $M = 20$, $zJ/\Gamma_p = 0.002,\ 0.01, 0.02,\ 0.1,\ 0.2$ (red, violet, green, orange and blue line respectively) and $\omega_{at} = \omega_c$. Correlators have been chosen in a symmetric way with respect to the center of the chain. Left panel: The correlation length λ obtained fitting $c(i, i+r)$ with an exponentially decaying function. The red line is the scaling predicted by Eq. (5.45). The other parameters are set as in Fig. 5.11.

of long-range order) and entropy (that quickly increases across the transition). The high entropy in the symmetry-broken phase is due to the intrinsic non-equilibrium nature of this phase. Remarkably, the numerical study showed that signature of the two phases are present already in small arrays.

The strongly correlated photon phases proposed here could be explored using photonic quantum simulators based on circuit QED (see chapter 1). The incoherent pumping scheme we exploit can be implemented by coherently driving the emitter into a third metastable level from which it fast decays into the excited state of the active transition, thus resulting into an effective incoherent pump [107].

Conclusion and outlook

This PhD thesis manuscript has presented original theoretical results about the physics of open quantum many-body systems, with a particular emphasis on non-equilibrium critical phenomena and dissipative phase transitions. The results presented in this manuscript are relevant for several emerging physical photonic platforms, such as semiconductor optical microcavities and superconducting circuit QED lattices. The main critical phenomena explored in the thesis are: (i) the power-law decay of the dynamical optical hysteresis in the quantum regime; (ii) a ferromagnetic transition in the dissipative anisotropic Heisenberg XYZ model in 2D; (iii) a phase transition from a Mott-like insulator to a superfluid phase in the incoherently pumped Bose-Hubbard model.

The dynamical optical hysteresis has been explored for a single-mode Kerr model, but the concepts presented in this manuscript can be applied to multimode and lattice systems, which will be explored in the future. For the single-mode case, we were able to solve the dynamics exactly with arbitrary precision in the considered regime. For lattice systems, the description of both steady-state and dynamical properties represents of course a much tougher challenge, especially when the spatial dimension is larger than one.

In order to explore the physics of lattices, we have extensively applied the corner-space renormalization, a technique which has been developed in our group to tackle the physics of 2D lattices, which are handled with difficulty by other state-of-the-art methods such as Matrix Product Operator techniques. This corner-space renormalization method is particularly suited for open lattices systems whose steady state has a low entropy. This method is far from being fully optimized and several improvements are likely to be implemented in the future. After completion of this manuscript, we became aware that the group of Savona at EPFL has significantly optimized the determination of the steady-state in the corner space, considerably reducing the memory cost and speeding up the calculations.

In the study of the anisotropic XYZ model in 2D, we have been able to evaluate via a finite-size analysis the critical exponents of this second-order dissipative phase transitions. We have also shown the critical behavior of the von Neumann entropy and of an entanglement witness, the Quantum Fisher Information. Additionally, we have explored the dynamics, showing results consistent with the emergence of a critical slowing down. Our results show that a dissipative phase transition can share the properties of both quantum and thermal phase transitions, a point that needs to be further explored

in future studies on different models.

Concerning the Bose-Hubbard model with incoherent pumping, we have presented results for a transition from a Mott-like insulator to a superfluid phase via a Gutzwiller mean-field ansatz for the system density matrix. This model can be applied to describe for example lasing of strongly correlated photons in systems where optical gain is provided by inverted two-level systems. Even in one dimension where a crossover is expected, this problem is particularly hard both for Matrix Product Operator techniques and the corner-space renormalization method: the former is limited by long-range spatial correlations, while the latter by the entropy of the density matrix. Future investigations are required to investigate more in depth this kind of dissipative phase transition with strongly correlated photons, which could be explored, e.g., by quantum simulators based on circuit QED lattices.

Bibliography

[1] M. Aigner and G.M. Ziegler. *Raisonnements divins: Quelques démonstrations mathématiques particulièrement élégantes*. Hermes Science Publications, 2017.

[2] Nikolas Metropolis. The Beginning of the Monte Carlo Method. *Los Alamos Science*, 1987.

[3] E. Fermi, J. Pasta, and S. Ulam. Studies of nonlinear problems I, Los Alamos Report LA 1940, 1955. In A. C. Newell, editor, *reproduced in Nonlinear Wave Motion*, Providence, RI, 1974. Amer. Math. Soc.

[4] Thierry Dauxois, Michel Peyrard, and Stefano Ruffo. The fermi–pasta–ulam 'numerical experiment': history and pedagogical perspectives. *European Journal of Physics*, 26(5):S3, 2005.

[5] Kenneth G. Wilson. The renormalization group: Critical phenomena and the Kondo problem. *Reviews of Modern Physics*, 47(4):773–840, October 1975.

[6] Ralf Bulla, Theo A. Costi, and Thomas Pruschke. Numerical renormalization group method for quantum impurity systems. *Reviews of Modern Physics*, 80:395–450, Apr 2008.

[7] S. R. White and R. M. Noack. Real-space quantum renormalization groups. *Physical Review Letters*, 68(24):3487–3490, 1992.

[8] Steven R. White. Density-matrix algorithms for quantum renormalization groups. *Physical Review B*, 48(14):10345–10356, October 1993.

[9] Stellan Östlund and Stefan Rommer. Thermodynamic limit of density matrix renormalization. *Physical Review Letters*, 75:3537–3540, Nov 1995.

[10] F. Verstraete, D. Porras, and J. I. Cirac. Density matrix renormalization group and periodic boundary conditions: A quantum information perspective. *Physical Review Letters*, 93:227205, Nov 2004.

[11] Guifré Vidal. Efficient Classical Simulation of Slightly Entangled Quantum Computations. *Physical Review Letters*, 91(14):147902, October 2003.

[12] D. Porras, F. Verstraete, and J. I. Cirac. Renormalization algorithm for the calculation of spectra of interacting quantum systems. *Physical Review B*, 73:014410, Jan 2006.

[13] Guifré Vidal. Efficient simulation of one-dimensional quantum many-body systems. *Physical Review Letters*, 93:040502, Jul 2004.

[14] F. Verstraete, J. J. García-Ripoll, and J. I. Cirac. Matrix Product Density Operators: Simulation of Finite-Temperature and Dissipative Systems. *Physical Review Letters*, 93(20):207204, November 2004.

[15] Michael Zwolak and Guifré Vidal. Mixed-State Dynamics in One-Dimensional Quantum Lattice Systems: A Time-Dependent Superoperator Renormalization Algorithm. *Physical Review Letters*, 93(20):207205, November 2004.

[16] Juan José García-Ripoll. Time evolution of matrix product states. *New Journal of Physics*, 8(12):305, 2006.

[17] G. Vidal. Classical simulation of infinite-size quantum lattice systems in one spatial dimension. *Physical Review Letters*, 98:070201, Feb 2007.

[18] F. Verstraete, M. M. Wolf, D. Perez-Garcia, and J. I. Cirac. Criticality, the area law, and the computational power of projected entangled pair states. *Physical Review Letters*, 96:220601, Jun 2006.

[19] F. Verstraete, V. Murg, and J.I. Cirac. Matrix product states, projected entangled pair states, and variational renormalization group methods for quantum spin systems. *Advances in Physics*, 57(2):143–224, 2008.

[20] E.m. Stoudenmire and Steven R. White. Studying Two-Dimensional Systems with the Density Matrix Renormalization Group. *Annual Review of Condensed Matter Physics*, 3(1):111–128, February 2012.

[21] Tao Xiang, Jizhong Lou, and Zhaobin Su. Two-dimensional algorithm of the density-matrix renormalization group. *Physical Review B*, 64:104414, Aug 2001.

[22] M. Fannes, B. Nachtergaele, and R. F. Werner. Finitely correlated states on quantum spin chains. *Communications in Mathematical Physics*, 144(3):443–490, Mar 1992.

[23] Subir Sachdev. *Quantum phase transitions*. Cambridge University Press, 2nd edition, 2011.

[24] Matthias Vojta. Quantum phase transitions. *Reports on Progress in Physics*, 66(12):2069, 2003.

[25] Immanuel Bloch, Jean Dalibard, and Wilhelm Zwerger. Many-body physics with ultracold gases. *Reviews of Modern Physics*, 80(3):885–964, July 2008.

[26] Matthew P. A. Fisher, Peter B. Weichman, G. Grinstein, and Daniel S. Fisher. Boson localization and the superfluid-insulator transition. *Physical Review B*, 40(1):546–570, July 1989.

[27] J. Eisert, M. Friesdorf, and C. Gogolin. Quantum many-body systems out of equilibrium. *Nat Phys*, 11(2):124–130, February 2015.

[28] Gabriele De Chiara, Simone Montangero, Pasquale Calabrese, and Rosario Fazio. Entanglement entropy dynamics of Heisenberg chains. *Journal of Statistical Mechanics: Theory and Experiment*, 2006(03):P03001, 2006.

[29] Pasquale Calabrese and John Cardy. Time dependence of correlation functions following a quantum quench. *Physical Review Letters*, 96:136801, Apr 2006.

[30] Iacopo Carusotto and Cristiano Ciuti. Quantum fluids of light. *Reviews of Modern Physics*, 85(1):299–366, February 2013.

[31] J. J. Hopfield. Theory of the contribution of excitons to the complex dielectric constant of crystals. *Physical Review*, 112:1555–1567, Dec 1958.

[32] J. Kasprzak, M. Richard, S. Kundermann, A. Baas, P. Jeambrun, J. M. J. Keeling, F. M. Marchetti, M. H. Szymańska, R. André, J. L. Staehli, V. Savona, P. B. Littlewood, B. Deveaud, and Le Si Dang. Bose–Einstein condensation of exciton polaritons. *Nature*, 443(7110):409–414, September 2006.

[33] Alberto Amo, Jérôme Lefrère, Simon Pigeon, Claire Adrados, Cristiano Ciuti, Iacopo Carusotto, Romuald Houdré, Elisabeth Giacobino, and Alberto Bramati. Superfluidity of polaritons in semiconductor microcavities. *Nature Physics*, 5(11):805–810, November 2009.

[34] Andrew D. Greentree, Charles Tahan, Jared H. Cole, and Lloyd C. L. Hollenberg. Quantum phase transitions of light. *Nature Physics*, 2(12):856–861, December 2006.

[35] Michael J. Hartmann, Fernando G. S. L. Brandão, and Martin B. Plenio. Strongly interacting polaritons in coupled arrays of cavities. *Nature Physics*, 2(12):849–855, December 2006.

[36] Dimitris G. Angelakis, Marcelo Franca Santos, and Sougato Bose. Photon-blockade-induced Mott transitions and XY spin models in coupled cavity arrays. *Physical Review A*, 76(3):031805, September 2007.

[37] A. Imamoğlu, H. Schmidt, G. Woods, and M. Deutsch. Strongly Interacting Photons in a Nonlinear Cavity. *Physical Review Letters*, 79(8):1467–1470, August 1997.

[38] K. M. Birnbaum, A. Boca, R. Miller, A. D. Boozer, T. E. Northup, and H. J. Kimble. Photon blockade in an optical cavity with one trapped atom. *Nature*, 436(7047):87–90, July 2005.

[39] C. Lang, D. Bozyigit, C. Eichler, L. Steffen, J. M. Fink, A. A. Abdumalikov, M. Baur, S. Filipp, M. P. da Silva, A. Blais, and A. Wallraff. Observation of resonant photon blockade at microwave frequencies using correlation function measurements. *Physical Review Letters*, 106:243601, Jun 2011.

[40] A. J. Daley, C. Kollath, U. Schollwöck, and G. Vidal. Time-dependent density-matrix renormalization-group using adaptive effective Hilbert spaces. *Journal of Statistical Mechanics: Theory and Experiment*, 2004(04):P04005, 2004.

[41] Matteo Biondi, Evert P. L. van Nieuwenburg, Gianni Blatter, Sebastian D. Huber, and Sebastian Schmidt. Incompressible polaritons in a flat band. *Physical Review Letters*, 115:143601, Sep 2015.

[42] Alberto Biella, Leonardo Mazza, Iacopo Carusotto, Davide Rossini, and Rosario Fazio. Photon transport in a dissipative chain of nonlinear cavities. *Physical Review A*, 91:053815, May 2015.

[43] Jian Cui, J. Ignacio Cirac, and Mari Carmen Bañuls. Variational Matrix Product Operators for the Steady State of Dissipative Quantum Systems. *Physical Review Letters*, 114(22):220601, June 2015.

[44] Eduardo Mascarenhas, Hugo Flayac, and Vincenzo Savona. Matrix-product-operator approach to the nonequilibrium steady state of driven-dissipative quantum arrays. *Physical Review A*, 92(2):022116, August 2015.

[45] Augustine Kshetrimayum, Hendrik Weimer, and Roman Orus. A simple tensor network algorithm for 2d steady states. *arXiv:1612.00656 [cond-mat, physics:quant-ph]*, December 2016. arXiv: 1612.00656.

[46] Jiasen Jin, Davide Rossini, Rosario Fazio, Martin Leib, and Michael J. Hartmann. Photon solid phases in driven arrays of nonlinearly coupled cavities. *Physical Review Letters*, 110:163605, Apr 2013.

[47] Alexandre Le Boité, Giuliano Orso, and Cristiano Ciuti. Steady-State Phases and Tunneling-Induced Instabilities in the Driven Dissipative Bose-Hubbard Model. *Physical Review Letters*, 110(23):233601, June 2013.

[48] Tony E. Lee, Sarang Gopalakrishnan, and Mikhail D. Lukin. Unconventional Magnetism via Optical Pumping of Interacting Spin Systems. *Physical Review Letters*, 110(25):257204, June 2013.

[49] Ryan M. Wilson, Khan W. Mahmud, Anzi Hu, Alexey V. Gorshkov, Mohammad Hafezi, and Michael Foss-Feig. Collective phases of strongly interacting cavity photons. *Physical Review A*, 94:033801, Sep 2016.

[50] Matteo Biondi, Gianni Blatter, Hakan E. Türeci, and Sebastian Schmidt. Nonequilibrium gas-liquid transition in the driven-dissipative photonic lattice. *Physical Review A*, 96:043809, Oct 2017.

[51] Jiasen Jin, Davide Rossini, Martin Leib, Michael J. Hartmann, and Rosario Fazio. Steady-state phase diagram of a driven qed-cavity array with cross-kerr nonlinearities. *Physical Review A*, 90:023827, Aug 2014.

[52] Jiasen Jin, Alberto Biella, Oscar Viyuela, Leonardo Mazza, Jonathan Keeling, Rosario Fazio, and Davide Rossini. Cluster Mean-Field Approach to the Steady-State Phase Diagram of Dissipative Spin Systems. *Physical Review X*, 6(3):031011, July 2016.

[53] Peter Degenfeld-Schonburg and Michael J. Hartmann. Self-consistent projection operator theory for quantum many-body systems. *Physical Review B*, 89:245108, Jun 2014.

[54] Hendrik Weimer. Variational principle for steady states of dissipative quantum many-body systems. *Physical Review Letters*, 114:040402, Jan 2015.

[55] Alberto Biella, Jiasen Jin, Oscar Viyuela, Cristiano Ciuti, Rosario Fazio, and Davide Rossini. Linked cluster expansions for open quantum systems on a lattice. *arXiv:1708.08666 [cond-mat, physics:quant-ph]*, August 2017. arXiv: 1708.08666.

[56] K. Vogel and H. Risken. Quasiprobability distributions in dispersive optical bistability. *Physical Review A*, 39(9):4675–4683, May 1989.

[57] Iacopo Carusotto and Cristiano Ciuti. Spontaneous microcavity-polariton coherence across the parametric threshold: Quantum monte carlo studies. *Physical Review B*, 72:125335, Sep 2005.

[58] M. Foss-Feig, P. Niroula, J. T. Young, M. Hafezi, A. V. Gorshkov, R. M. Wilson, and M. F. Maghrebi. Emergent equilibrium in many-body optical bistability. *Physical Review A*, 95:043826, Apr 2017.

[59] Filippo Vicentini, Fabrizio Minganti, Riccardo Rota, Giuliano Orso, and Cristiano Ciuti. Critical slowing down in driven-dissipative Bose-Hubbard lattices. *arXiv:1709.04238 [cond-mat, physics:quant-ph]*, September 2017. arXiv: 1709.04238.

[60] Wim Casteels, Ryan M. Wilson, and Michiel Wouters. Gutzwiller Monte Carlo approach for a critical dissipative spin model. *arXiv:1709.00693 [cond-mat, physics:quant-ph]*, September 2017. arXiv: 1709.00693.

[61] Jean Dalibard, Yvan Castin, and Klaus Mølmer. Wave-function approach to dissipative processes in quantum optics. *Physical Review Letters*, 68(5):580–583, February 1992.

[62] Klaus Mølmer, Yvan Castin, and Jean Dalibard. Monte Carlo wave-function method in quantum optics. *JOSA B*, 10(3):524–538, March 1993.

[63] H. J. Carmichael. Quantum trajectory theory for cascaded open systems. *Physical Review Letters*, 70(15):2273–2276, April 1993.

[64] L. M. Sieberer, M. Buchhold, and S. Diehl. Keldysh field theory for driven open quantum systems. *Reports on Progress in Physics*, 79(9):096001, 2016.

[65] L. M. Sieberer, S. D. Huber, E. Altman, and S. Diehl. Nonequilibrium functional renormalization for driven-dissipative bose-einstein condensation. *Physical Review B*, 89:134310, Apr 2014.

[66] L. M. Sieberer, S. D. Huber, E. Altman, and S. Diehl. Dynamical critical phenomena in driven-dissipative systems. *Physical Review Letters*, 110:195301, May 2013.

[67] Mohammad F. Maghrebi and Alexey V. Gorshkov. Nonequilibrium many-body steady states via Keldysh formalism. *Physical Review B*, 93(1):014307, January 2016.

[68] Amo Alberto and Bloch Jacqueline. Cavity polaritons: Crossroad between nonlinear optics and atomic condensates. In Alexia Auffèves, Dario Gerace, Maxime Richard, Stefano Portolan, Marcelo França Santos, Leong Chuan Kwek, and Christian Miniatura, editors, *Strong Light-Matter Coupling: From Atoms to Solid-State Systems*. World Scientific, 2014.

[69] C Ciuti, P Schwendimann, and A Quattropani. Theory of polariton parametric interactions in semiconductor microcavities. *Semiconductor Science and Technology*, 18(10):S279, 2003.

[70] V. G. Sala, D. D. Solnyshkov, I. Carusotto, T. Jacqmin, A. Lemaître, H. Terças, A. Nalitov, M. Abbarchi, E. Galopin, I. Sagnes, J. Bloch, G. Malpuech, and A. Amo. Spin-orbit coupling for photons and polaritons in microstructures. *Physical Review X*, 5:011034, Mar 2015.

[71] F. Baboux, L. Ge, T. Jacqmin, M. Biondi, E. Galopin, A. Lemaître, L. Le Gratiet, I. Sagnes, S. Schmidt, H. E. Türeci, A. Amo, and J. Bloch. Bosonic Condensation and Disorder-Induced Localization in a Flat Band. *Physical Review Letters*, 116(6):066402, February 2016.

[72] Florent Baboux, Eli Levy, Aristide Lemaître, Carmen Gómez, Elisabeth Galopin, Luc Le Gratiet, Isabelle Sagnes, Alberto Amo, Jacqueline Bloch, and Eric Akkermans. Measuring topological invariants from generalized edge states in polaritonic quasicrystals. *Physical Review B*, 95(16):161114, April 2017.

[73] M. Milićević, T. Ozawa, G. Montambaux, I. Carusotto, E. Galopin, A. Lemaître, L. Le Gratiet, I. Sagnes, J. Bloch, and A. Amo. Orbital Edge States in a Photonic Honeycomb Lattice. *Physical Review Letters*, 118(10):107403, March 2017.

[74] Michel Devoret. Lecture at the collège de france: Circuits et signaux quantiques (i), May 2008.

[75] Yuriy Makhlin, Gerd Schön, and Alexander Shnirman. Quantum-state engineering with josephson-junction devices. *Reviews of Modern Physics*, 73:357–400, May 2001.

[76] Jens Koch, Terri M. Yu, Jay Gambetta, A. A. Houck, D. I. Schuster, J. Majer, Alexandre Blais, M. H. Devoret, S. M. Girvin, and R. J. Schoelkopf. Charge-insensitive qubit design derived from the cooper pair box. *Physical Review A*, 76:042319, Oct 2007.

[77] J. A. Schreier, A. A. Houck, Jens Koch, D. I. Schuster, B. R. Johnson, J. M. Chow, J. M. Gambetta, J. Majer, L. Frunzio, M. H. Devoret, S. M. Girvin, and R. J. Schoelkopf. Suppressing charge noise decoherence in superconducting charge qubits. *Physical Review B*, 77:180502, May 2008.

[78] Sebastian Schmidt and Jens Koch. Circuit qed lattices: Towards quantum simulation with superconducting circuits. *Annalen der Physik*, 525(6):395–412, 2013.

[79] E. T. Jaynes and F. W. Cummings. Comparison of quantum and semiclassical radiation theories with application to the beam maser. *Proceedings of the IEEE*, 51(1):89–109, January 1963.

[80] T Grujic, S R Clark, D Jaksch, and D G Angelakis. Non-equilibrium many-body effects in driven nonlinear resonator arrays. *New Journal of Physics*, 14(10):103025, 2012.

[81] Mattias Fitzpatrick, Neereja M. Sundaresan, Andy C. Y. Li, Jens Koch, and Andrew A. Houck. Observation of a Dissipative Phase Transition in a One-Dimensional Circuit QED Lattice. *Physical Review X*, 7(1):011016, February 2017.

[82] Howard J. Carmichael. *Statistical Methods in Quantum Optics 1 - Master Equations and Fokker-Planck Equations*. Springer, 2002.

[83] Stanislaw Kryszewski and Justyna Czechowska-Kryszk. Master equation - tutorial approach. *arXiv:0801.1757 [quant-ph]*, January 2008. arXiv: 0801.1757.

[84] Ángel Rivas, A Douglas K Plato, Susana F Huelga, and Martin B Plenio. Markovian master equations: a critical study. *New Journal of Physics*, 12(11):113032, 2010.

[85] Cristiano Ciuti, Gérald Bastard, and Iacopo Carusotto. Quantum vacuum properties of the intersubband cavity polariton field. *Physical Review B*, 72:115303, Sep 2005.

[86] Félix Beaudoin, Jay M. Gambetta, and A. Blais. Dissipation and ultrastrong coupling in circuit qed. *Physical Review A*, 84:043832, Oct 2011.

[87] M. B. Plenio and P. L. Knight. The quantum-jump approach to dissipative dynamics in quantum optics. *Review of Modern Physics*, 70:101–144, Jan 1998.

[88] Crispin Gardiner and Peter Zoller. *Quantum Noise - A Handbook of Markovian and Non-Markovian*. Springer-Verlag Berlin Heidelberg, 2004.

[89] Ian P McCulloch. From density-matrix renormalization group to matrix product states. *Journal of Statistical Mechanics: Theory and Experiment*, 2007(10):P10014, 2007.

[90] E. M. Kessler, G. Giedke, A. Imamoglu, S. F. Yelin, M. D. Lukin, and J. I. Cirac. Dissipative phase transition in a central spin system. *Physical Review A*, 86(1):012116, July 2012.

[91] H. M. Gibbs, S. L. McCall, and T. N. C. Venkatesan. Differential gain and bistability using a sodium-filled fabry-perot interferometer. *Physical Review Letters*, 36:1135–1138, May 1976.

[92] A. Baas, J. Ph. Karr, H. Eleuch, and E. Giacobino. Optical bistability in semiconductor microcavities. *Physical Review A*, 69(2):023809, February 2004.

[93] Daniele Bajoni, Elizaveta Semenova, Aristide Lemaître, Sophie Bouchoule, Esther Wertz, Pascale Senellart, Sylvain Barbay, Robert Kuszelewicz, and Jacqueline Bloch. Optical Bistability in a GaAs-Based Polariton Diode. *Physical Review Letters*, 101(26):266402, December 2008.

[94] T. K. Paraïso, M. Wouters, Y. Léger, F. Morier-Genoud, and B. Deveaud-Plédran. Multistability of a coherent spin ensemble in a semiconductor microcavity. *Nature Materials*, 9(8):655–660, August 2010.

[95] F. R. Ong, M. Boissonneault, F. Mallet, A. Palacios-Laloy, A. Dewes, A. C. Doherty, A. Blais, P. Bertet, D. Vion, and D. Esteve. Circuit QED with a Nonlinear Resonator: ac-Stark Shift and Dephasing. *Physical Review Letters*, 106(16):167002, April 2011.

[96] P. D. Drummond and D. F. Walls. Quantum theory of optical bistability. I. Nonlinear polarisability model. *Journal of Physics A: Mathematical and General*, 13(2):725, February 1980.

[97] H. Risken, C. Savage, F. Haake, and D. F. Walls. Quantum tunneling in dispersive optical bistability. *Physical Review A*, 35:1729–1739, Feb 1987.

[98] K. Vogel and H. Risken. Quantum-tunneling rates and stationary solutions in dispersive optical bistability. *Physical Review A*, 38(5):2409–2422, September 1988.

[99] H. Risken and K. Vogel. Quantum tunneling rates in dispersive optical bistability for low cavity damping. *Physical Review A*, 38(3):1349–1357, August 1988.

[100] Joseph Kerckhoff, Michael A. Armen, and Hideo Mabuchi. Remnants of semiclassical bistability in the few-photon regime of cavity qed. *Opt. Express*, 19(24):24468–24482, Nov 2011.

[101] Hideo Mabuchi. Coherent-feedback control strategy to suppress spontaneous switching in ultralow power optical bistability. *Applied Physics Letters*, 98(19):193109, 2011.

[102] H. Abbaspour, S. Trebaol, F. Morier-Genoud, M. T. Portella-Oberli, and B. Deveaud. Stochastic Resonance in Collective Exciton-Polariton Excitations inside a GaAs Microcavity. *Physical Review Letters*, 113(5):057401, July 2014.

[103] H. Abbaspour, G. Sallen, S. Trebaol, F. Morier-Genoud, M. T. Portella-Oberli, and B. Deveaud. Effect of a noisy driving field on a bistable polariton system. *Physical Review B*, 92:165303, Oct 2015.

[104] R. Vijay, M. H. Devoret, and I. Siddiqi. Invited review article: The josephson bifurcation amplifier. *Review of Scientific Instruments*, 80(11):111101, 2009.

[105] W. Casteels, F. Storme, A. Le Boité, and C. Ciuti. Power laws in the dynamic hysteresis of quantum nonlinear photonic resonators. *Physical Review A*, 93:033824, Mar 2016.

[106] S. R. K. Rodriguez, W. Casteels, F. Storme, N. Carlon Zambon, I. Sagnes, L. Le Gratiet, E. Galopin, A. Lemaître, A. Amo, C. Ciuti, and J. Bloch. Probing a dissipative phase transition via dynamical optical hysteresis. *Physical Review Letters*, 118:247402, Jun 2017.

[107] Ruichao Ma, Clai Owens, Andrew Houck, David I. Schuster, and Jonathan Simon. Autonomous stabilizer for incompressible photon fluids and solids. *Physical Review A*, 95(4):043811, April 2017.

[108] K. E. Cahill and R. J. Glauber. Ordered Expansions in Boson Amplitude Operators. *Physical Review*, 177(5):1857–1881, January 1969.

[109] K. E. Cahill and R. J. Glauber. Density Operators and Quasiprobability Distributions. *Physical Review*, 177(5):1882–1902, January 1969.

[110] Alexandre Le Boité, Giuliano Orso, and Cristiano Ciuti. Bose-Hubbard model: Relation between driven-dissipative steady states and equilibrium quantum phases. *Physical Review A*, 90(6):063821, December 2014.

[111] T W B Kibble. Topology of cosmic domains and strings. *Journal of Physics A: Mathematical and General*, 9(8):1387, 1976.

[112] W. H. Zurek. Cosmological experiments in superfluid helium? *Nature*, 317(6037):505–508, October 1985.

[113] Wojciech H. Zurek, Uwe Dorner, and Peter Zoller. Dynamics of a quantum phase transition. *Physical Review Letters*, 95:105701, Sep 2005.

[114] Jacek Dziarmaga. Dynamics of a quantum phase transition and relaxation to a steady state. *Advances in Physics*, 59(6):1063–1189, 2010.

[115] Bogdan Damski. The simplest quantum model supporting the kibble-zurek mechanism of topological defect production: Landau-zener transitions from a new perspective. *Physical Review Letters*, 95:035701, Jul 2005.

[116] Bogdan Damski and Wojciech H. Zurek. Adiabatic-impulse approximation for avoided level crossings: From phase-transition dynamics to landau-zener evolutions and back again. *Physical Review A*, 73:063405, Jun 2006.

[117] Clarence Zener. Non-Adiabatic Crossing of Energy Levels. *Proceedings of the Royal Society of London A: Mathematical, Physical and Engineering Sciences*, 137(833):696–702, September 1932.

[118] Lev Landau. Zur theorie der energieubertragung. ii. *Physikalische Zeitschrift der Sowjetunion*, 2:46, 1932.

[119] V. M. Akulin and W. P. Schleich. Landau-zener transition to a decaying level. *Physical Review A*, 46:4110–4113, Oct 1992.

[120] W. Casteels, R. Fazio, and C. Ciuti. Critical dynamical properties of a first-order dissipative phase transition. *Physical Rev. A*, 95:012128, Jan 2017.

[121] W. Casteels, R. Rota, F. Storme, and C. Ciuti. Probing photon correlations in the dark sites of geometrically frustrated cavity lattices. *Physical Review A*, 93(4):043833, 2016.

[122] R. Rota, F. Storme, N. Bartolo, R. Fazio, and C. Ciuti. Critical behavior of dissipative two-dimensional spin lattices. *Physical Review B*, 95(13):134431, April 2017.

[123] S. Finazzi, A. Le Boité, F. Storme, A. Baksic, and C. Ciuti. Corner-Space Renormalization Method for Driven-Dissipative Two-Dimensional Correlated Systems. *Physical Review Letters*, 115(8):080604, August 2015.

[124] W. Casteels, S. Finazzi, A. Le Boité, F. Storme, and C. Ciuti. Truncated correlation hierarchy schemes for driven-dissipative multimode quantum systems. *New Journal of Physics*, 18(9):093007, 2016.

[125] Alberto Biella, Florent Storme, José Lebreuilly, Davide Rossini, Rosario Fazio, Iacopo Carusotto, and Cristiano Ciuti. Phase diagram of incoherently-driven strongly correlated photonic lattices. *arXiv:1704.08978 [cond-mat, physics:quant-ph]*, April 2017. arXiv: 1704.08978.

[126] Vincenzo Savona. Private communication.

[127] L. M. Sieberer, S. D. Huber, E. Altman, and S. Diehl. Dynamical Critical Phenomena in Driven-Dissipative Systems. *Physical Review Letters*, 110(19):195301, May 2013.

[128] L. M. Sieberer, S. D. Huber, E. Altman, and S. Diehl. Nonequilibrium functional renormalization for driven-dissipative Bose-Einstein condensation. *Physical Review B*, 89(13):134310, April 2014.

[129] Ehud Altman, Lukas M. Sieberer, Leiming Chen, Sebastian Diehl, and John Toner. Two-Dimensional Superfluidity of Exciton Polaritons Requires Strong Anisotropy. *Physical Review X*, 5(1):011017, February 2015.

[130] G. Vidal and R. F. Werner. Computable measure of entanglement. *Physical Review A*, 65(3):032314, February 2002.

[131] Philipp Hauke, Markus Heyl, Luca Tagliacozzo, and Peter Zoller. Measuring multipartite entanglement through dynamic susceptibilities. *Nature Physics*, 12(8):778–782, August 2016.

[132] Jian Ma and Xiaoguang Wang. Fisher information and spin squeezing in the Lipkin-Meshkov-Glick model. *Physical Review A*, 80(1):012318, July 2009.

[133] Teng-Long Wang, Ling-Na Wu, Wen Yang, Guang-Ri Jin, Neill Lambert, and Franco Nori. Quantum Fisher information as a signature of the superradiant quantum phase transition. *New Journal of Physics*, 16(6):063039, 2014.

[134] Zheng Qiang, Yao Yao, and Xu Xun-Wei. Probing berezinskii–kosterlitz–thouless phase transition of spin-half xxz chain by quantum fisher information. *Communications in Theoretical Physics*, 63(3):279, 2015.

[135] Luca Pezzé and Augusto Smerzi. Entanglement, Nonlinear Dynamics, and the Heisenberg Limit. *Physical Review Letters*, 102(10):100401, March 2009.

[136] Riccardo Rota, Fabrizio Minganti, Alberto Biella, and Cristiano Ciuti. Dynamical properties of dissipative XYZ Heisenberg lattices. *arXiv:1712.02716 [cond-mat, physics:quant-ph]*, December 2017. arXiv: 1712.02716.

[137] R. Orús and G. Vidal. Infinite time-evolving block decimation algorithm beyond unitary evolution. *Physical Review B*, 78(15):155117, October 2008.

[138] Michael J. Hartmann. Quantum simulation with interacting photons. *Journal of Optics*, 18(10):104005, 2016.

[139] A. Tomadin, V. Giovannetti, R. Fazio, D. Gerace, I. Carusotto, H. E. Türeci, and A. Imamoglu. Signatures of the superfluid-insulator phase transition in laser-driven dissipative nonlinear cavity arrays. *Physical Review A*, 81(6):061801, June 2010.

[140] Alberto Biella, Leonardo Mazza, Iacopo Carusotto, Davide Rossini, and Rosario Fazio. Photon transport in a dissipative chain of nonlinear cavities. *Physical Review A*, 91:053815, May 2015.

[141] Changhyoup Lee, Changsuk Noh, Nikolaos Schetakis, and Dimitris G. Angelakis. Few-photon transport in many-body photonic systems: A scattering approach. *Physical Review A*, 92:063817, Dec 2015.

[142] Felix Nissen, Sebastian Schmidt, Matteo Biondi, Gianni Blatter, Hakan E. Türeci, and Jonathan Keeling. Nonequilibrium dynamics of coupled qubit-cavity arrays. *Physical Review Letters*, 108:233603, Jun 2012.

[143] José Lebreuilly, Michiel Wouters, and Iacopo Carusotto. Towards strongly correlated photons in arrays of dissipative nonlinear cavities under a frequency-dependent incoherent pumping. *Comptes Rendus Physique*, 17(8):836–860, October 2016.

[144] José Lebreuilly, Alberto Biella, Florent Storme, Davide Rossini, Rosario Fazio, Cristiano Ciuti, and Iacopo Carusotto. Stabilizing strongly correlated photon fluids with a non-Markovian reservoir. *arXiv:1704.01106 [cond-mat, physics:quant-ph]*, April 2017. arXiv: 1704.01106.

[145] Guido Schmid, Synge Todo, Matthias Troyer, and Ansgar Dorneich. Finite-Temperature Phase Diagram of Hard-Core Bosons in Two Dimensions. *Physical Review Letters*, 88(16):167208, April 2002.

[146] Erich J. Mueller, Tin-Lun Ho, Masahito Ueda, and Gordon Baym. Fragmentation of bose-einstein condensates. *Physical Review A*, 74:033612, Sep 2006.

[147] J. Ruiz-Rivas, E. del Valle, C. Gies, P. Gartner, and M. J. Hartmann. Spontaneous collective coherence in driven dissipative cavity arrays. *Physical Review A*, 90(3):033808, September 2014.

[148] M. Wouters and I. Carusotto. Absence of long-range coherence in the parametric emission of photonic wires. *Physical Review B*, 74(24):245316, December 2006.

[149] M. H. Szymańska, J. Keeling, and P. B. Littlewood. Nonequilibrium Quantum Condensation in an Incoherently Pumped Dissipative System. *Physical Review Letters*, 96(23):230602, June 2006.

[150] M. Girardeau. Relationship between Systems of Impenetrable Bosons and Fermions in One Dimension. *Journal of Mathematical Physics*, 1(6):516–523, November 1960.

[151] I. Carusotto, D. Gerace, H. E. Tureci, S. De Liberato, C. Ciuti, and A. Imamoğlu. Fermionized Photons in an Array of Driven Dissipative Nonlinear Cavities. *Physical Review Letters*, 103(3):033601, July 2009.